MAGYAR ÁLLAMI
EÖTVÖS LORÁND
GEOFIZIKAI INTÉZET

EÖTVÖS LORÁND
GEOPHYSICAL INSTITUTE
OF HUNGARY

GEOFIZIKAI KÖZLEMÉNYEK

GEOPHYSICAL TRANSACTIONS

ВЕНГЕРСКИЙ
ГЕОФИЗИЧЕСКИЙ
ИНСТИТУТ
ИМ Л. ЭТВЕША

ГЕОФИЗИЧЕСКИЙ
БЮЛЛЕТЕНЬ

BUDAPEST

CONTENTS

VOL. 33. NO. 3–4. MAY 1988. (ISSN 0016–7177)

TARTALOMJEGYZÉK

СОДЕРЖАНИЕ

GEOPHYSICAL TRANSACTIONS 1988
Vol. 33. No. 3–4. pp. 157–173

STUDY OF METHODS FOR DETERMINING VELOCITY AND DEPTH PARAMETERS IN LAYERED REALISTIC MEDIA

V. M. GLOGOVSKY* and G. N. GOGONENKOV*

Different methods for solving the problem on the basis of local homogeneity of the layers are compared by a special representation of the CDP traveltime curve. Error estimates for the velocity and the depth computations are given as a function of the errors of the initial data and the inhomogeneity of the medium. The problem of regarding the layers as locally homogeneous media is discussed.

Keywords: inverse problem, seismic discontinuities, traveltime curves, common-depth-point method, inhomogeneous media, seismic inversion

1. Introduction

One of the traditional problems in seismics is that of determining the spatial orientation of reflectors and the velocity of the layers bounded by them from the kinematic parameters (t_0, V_{CDP}, etc.) of the reflected waves. At one time this problem, called the inverse problem of reflection seismics, stood in the centre of data processing; subsequently, interest weakened for almost a decade and after that — through the emergence of new techniques and possibilities — it took on a new lease of life on the basis of newer ideas. Nevertheless, it never fully disappeared from the horizon of geophysicists since the resulting medium parameters are important not only for themselves (such as, for instance, the layer velocity as a substantial source of information necessary for predicting the lithological composition), but they are indispensable for proper data processing (e.g. the layer model of the medium is essential for the migration taking the refraction of rays into consideration as well).

The majority of the present-day methods used for solving the inverse kinematic problem of reflection seismics carries out the computation layer by layer, that is, going downward the velocity and the depth of each subsequent individual layer are determined successively from the kinematic parameters of certain reflecting interfaces marked out previously on the time section. Then in the course of the solution of this problem, it will be supposed for each layer, that

1. the parameters of layers in higher up positions are known and were determined properly;

* Central Geophysical Expedition of the Ministry of Oil Industry, 123298 Moscow, ul. Narodnogo Opolcheniya, d. 40, korp. 3, USSR
Manuscript received: 2 June, 1987

2. in each step of the computation the layers are locally homogeneous.

In reality, however, the requirements mentioned above are fulfilled only approximately, as a result of which the estimates for the medium parameters sought for are subject to errors. These result mainly from the supposition of the layers being locally homogeneous. Direct velocity measurements in acoustic loggings demonstrate that the layers belonging to time differences larger than 0.3–0,5 s are seldom homogeneous, although the reflections bounding the intervals selected for the layer-by-layer solution of the inverse problem border just such regions of the medium. This is confirmed indirectly by the often intensive arrivals more or less traceable for some length observable on the time section, between reflectors chosen as layer boundaries for the data processing.

In reality, errors will result from neglecting inhomogeneity when determining the parameters of such layers, and these not only distort the parameters of the layer itself, but also adversely affect the accuracy of the parameters of the subsequent layers. In fact, the initial data necessary for solving the inverse problem for the subsequent layer shift over from the surface to the upper interface of the subsequent layer, thus, these data will be erroneous as well because of the parameter errors of the previous (upper) layer.

In this paper, we study the effect of the inhomogeneity of the real medium on the quality of the solution of the inverse kinematic problem if we assume locally homogeneous layers. First, a convenient representation of the time field is developed, actually for the CDP traveltime curves (i.e. the arrival times of the reflections are given as functions of the shotpoint and the recording locations). Subsequently, those concepts are reviewed on which the solution of the inverse problem referring to a homogeneous layer are based and it is shown that the various algorithms are equivalent to each other for homogeneous media, but they behave differently to velocity inhomogeneity. This enables one to formulate the task of identifying a layer by whether it is homogeneous or not. In the following the specific aspects of the layer-by-layer computation are discussed, given that the layer is inhomogeneous and the initial data are subject to error.

Since these problems are rather complicated and multifarious, our main intention is not so much to give detailed answers to the questions raised as to develop a more general approach to them on the basis of which answers are obtained in a more coherent way.

Let us review the tools necessary for solving the problem.

2. Skeleton velocity and the CDP traveltime curve representation

One of the difficulties in solving the inverse kinematic problem for inhomogeneous media comes from the lack of an equation for the traveltime curves of reflected waves, in more or less simple form. The traveltime curve is usually described by a power series in which the coefficients of the terms are functions of the layer parameters [URUPOV and LEVIN 1985]. In the case of comparatively more complex media, these series are slowly convergent and in addition to this

the coefficients are complicated expressions, and are difficult to evaluate — especially with regard to solving the inverse kinematic problem. Thus we intend to formulate a traveltime curve representation with generalized medium characteristics which are not explicitely related to medium parameters. Nevertheless, this representation provides an opportunity to investigate several methods for determining the parameters of inhomogeneous layers and to compare them with each other.

Consider a layer with varying velocity $v(x, z)$ and a reflection of depth $h(x)$ (*Fig. 1*). Let n be the ray with normal incidence to reflector $h(x)$ starting from point Θ and reaching $(\xi,h(\xi))$. Denote by l the distance between points Θ and $(\xi,h(\xi))$, and by ω the angle between this straight line and the vertical. Then (l,ω) are the polar co-ordinates of reflection point $(\xi,h(\xi))$.

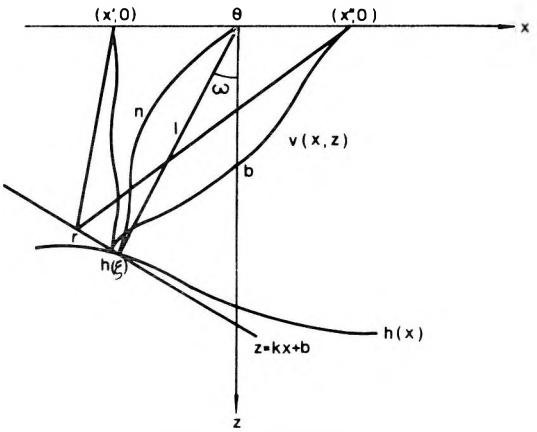

Fig. 1. Definition of notations

1. ábra. Vázlat a jelölések és közelítések szemléltetésére

Рис. 1. К определению понятия каркасной скорости.

In oder to obtain the formulae in a more simple form, the upper interface (observation line) is taken to be horizontal; however, this limitation can easily be cancelled in the following operations if necessary. Upon similar considerations (with the same remark) the planar case will now be considered instead of the three-dimensional one.

Let the straight line $z = kx + b$ passing through point $(\xi,h(\xi))$ be perpendicular to the straight line $(\Theta,\xi,h(\xi))$, thus $k = \tan\omega$. Out of the arbitrary points $(x', 0)$ and $(x'', 0)$ on the survey line let the first one be the shotpoint, the second one the recording point and consider the following zig-zag line: $(x', 0) - r - (x'', 0)$, $r \in kx + b$, which satisfies the laws of optics at point r. We call such zig-zag lines, belonging to different source and recording points, skeleton rays, in order to distinguish them from the actual raypaths corresponding to reflector $h(x)$, which are curved if $v(x, z) \neq \text{const}$. The skeleton velocity is determined for an arbitrary pair of points $(x_i', 0)$, $(x_i'', 0)$ in the form of $v_s(i) = A_i/t_i$

where t_i is the actual traveltime from the ith source point to the ith recording point, and Δ_i is the length of the ith skeleton raypath. Then, the identity $t_i = \Delta_i / v_s(i)$ will apply.

Let us denote the quantity $2l/t_0$ by $\bar{v}$ (t_0 is the actual traveltime if both the source and the recording are placed at point Θ) then $v_s(i)$ can be expressed in the form:

$$v_s(i) = \frac{\bar{v}}{\sqrt{1-f(i)}} \tag{1}$$

where $f(i)$ is a function (the negative sign under the square root has been chosen for the sake of convenience), and

$$t_i = \frac{\sqrt{1-f(i)}}{\bar{v}} \Delta i \tag{2}$$

The quantity Δ_i (the length of the zig-zag) can easily be obtained in any given case, even for arbitrarily shaped surfaces. Actually, if the survey line is horizontal and the common midpoint is at $\Theta = \{0, 0\}$, the CDP traveltime curve is given by:

$$\Delta_x = 2\sqrt{b^2 + x^2}\cos\omega$$

Consequently Eq. (2) will take the form:

$$t(x) = \frac{2\sqrt{1-f(x)}}{v_0} \sqrt{b^2 + x^2} \tag{3}$$

where $v_0 = \bar{v}/\cos\omega$, x is the half offset $x \in [0, L]$.

Referring to the CDP traveltime curve, function $f(x)$ can be characterized in the following way as well. From the definition of $\bar{v}$ it follows that $v_0 = 2b/t_0$. From this and from the identity $t(0) = t_0$ it follows that $f(0) = 0$. Finally, from the symmetry of the CDP traveltime curve it follows that function $f(x)$ is an even function. Now, if one or another form of $f(x)$ is used, different representations of the CDP traveltime curve can be obtained. If $t(x)$ is an analytic function, then $f(x)$ can be represented in the form of an expansion in powers of x^2, the coefficients of which depend on the (even) derivatives of $t(x)$ taken at $x = 0$ or on the derivatives of $t^2(x)$ in quadratic co-ordinates. For a detailed description see [Goldin and Suvorov 1977]. The advantage of the expressions given in such form lies in the fact that the derivatives of $t(x)$ can be expressed by the parameters of the medium [Goldin 1979], thus, the equation of the traveltime curve can be obtained as a function of the physical parameters of the section. There is an additional possibility that the coefficients in the expansion of $f(x)$ are determined in such a way that the expansion should be the best quadratic approximation of $f(x)$. This reduces considerably the requirement for the smooth behaviour of $f(x)$, although there is no explicit relationship between the coefficients of the series and the parameters of the medium. This relationship

is, however, not very important with regard to the investigation of the solution to the inverse problem; much rather it is essential that greater freedom in the characterization of the medium is permitted (e.g. there is no need to prescribe the differentiability, the continuity, etc. at the layer boundaries) and just upon such considerations this way of obtaining the traveltime curve has been chosen (in connection with this we refer to PUZYREV's work [1979] who treated the traveltime curve similarly).
Let

$$f(x) = \sum_{j=1}^{n} \gamma_j x^{2j} + r_n(x)$$

where $r_n(x)$ is an even function, and $r_n(0) = 0$.
Considering that from Eq. (1)

$$f(x) = 1 - \left(\frac{\bar{v}}{v_s(x)}\right)^2$$

let us determine the coefficients γ_j so that

$$\int_0^L \left[1 - \left(\frac{\bar{v}}{v_k(x)}\right)^2 - \sum_{j=1}^{n} \gamma_j x^{2j}\right]^2 \mathrm{d}x = \min_{(\gamma_j)}.$$

(it should be recalled that L is half the maximum offset). In order to compute the coefficients γ_j the time values $t(x)$ are necessary (the question in this case may be the approximation of the observed traveltime curve). We follow — however — an opposite course of treatment in studying the methods for solving the inverse kinematic problem: we assume $f(x)$ in the form $\sum_{j=1}^{n} \gamma_j x^{2j}$ i.e. the term $r_n(x)$ will be neglected. Then the traveltime curve

$$t_n(x) = 2v_0^{-1}\left[\left(1 + \sum_{j=1}^{n} \gamma_j x^{2j}\right)(b^2 + x^2)\right]^{1/2}$$

corresponds to an inhomogeneous medium; substituting $t_n(x)$ and its functionals into an explicit formula which gives the solution to the inverse problem in one or another way, it can be clarified how the solution and the coefficients γ_j are related to each other — the latter being characteristic to the extent to which the medium departs from the model of homogeneous media with plane interfaces (for which obviously each $\gamma_j = 0$). Now, there is no need to know the dependence of γ_j on the parameters of the medium: a knowledge of the domain of variation of the coefficients is sufficient. In addition, statements can be made on several opinions referring to the solution of the inverse kinematic problem by studying the most "simple" inhomogeneous medium, in which $f(x) = \gamma x^2$ and the traveltime curve

$$t(x) = \frac{2}{v_0}\sqrt{b^2 + (1 - b^2\gamma)x^2 - \gamma x^4} \tag{4}$$

needs only one additional parameter in comparison with those of the homogeneous one. Nevertheless, those models for which the traveltime curve can be approximated well by function (4) may even consist of "quite inhomogeneous" media in respect to the a priori ideas of possible velocity variations. In *Fig 2*, a two-layer model can be seen with differently dipping interfaces and with considerable velocity contrast. Even so, the traveltime curves of the lower reflector (which are influenced by the inhomogeneous layer between the lower interface and the surface) can be obtained from Eq. (4) with an error less than 0.5 ms.

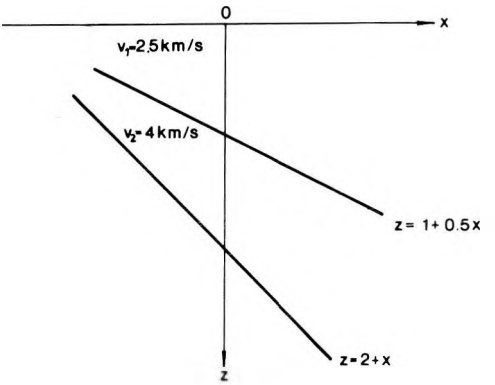

Fig. 2. Example for an inhomogeneous medium in which the CDP traveltime curve is well approximated by Expression (4)

2. ábra. Példa olyan inhomogén közegre, amelyben a CDP terjedési időgörbét jól közelíti a (4) kifejezés

Рис. 2. Пример неоднородной среды, в которой годографы ОГТ хорошо аппроксимируются выражением (4).

During seismic data processing, the kinematic parameters of the reflections are determined in the course of signal enhancement, consequently we do not deal with the traveltime curves themselves, but with their functionals, e.g. with t_0 and V_{CDP}. It is known that the values obtained in such a way are close to those obtained when the traveltime curve is approximated by the hyperbola $(\alpha + \beta x^2)^{1/2}$ with the least squares method, and it is supposed that $t_0^2 = \alpha$ and $0.25V_{CDP}^2 = \beta$. Such approximation of traveltime curve (3) (for simplicity with co-ordinates (x, t^2)) leads to the minimization of the following integral:

$$\int_0^L (t^2(x) - \alpha - \beta x^2)^2 \, dx =$$

$$= \int_0^L \left[\frac{4}{v_0^2}(b^2 - b^2 f(x) + x^2 - x^2 f(x)) - \alpha - \beta x^2\right]^2 dx = \min_{(\alpha, \beta)}$$

After differentiating it with respect to α and β, and making it equal to 0, we get the following linear equation system:

$$\alpha L+\beta\frac{L^3}{3}=\frac{4}{v_0^2}\left[b^2L-b^2\int_0^L f(x)\,dx+\frac{L^3}{3}-\int_0^L x^2f(x)\,dx\right]$$

$$\alpha L^3/3+\beta\frac{L^5}{5}=\frac{4}{v_0^2}\left[b^2L^3/3-b^2\int_0^L x^2f(x)\,dx+\frac{L^5}{5}\int_0^L x^4f(x)\,dx\right].$$

From this equation system we get:

$$\begin{aligned}\alpha&=\frac{4b^2}{v_0^2}-\frac{9b^2}{v_0^2L}\int_0^L f(x)\,dx+\frac{3}{v_0^2L}\left(\frac{5b^2}{L^2}-3\right)\int_0^L x^2f(x)\,dx+\frac{15}{v_0^2L^3}\int_0^L x^4f(x)\,dx\\ \beta&=\frac{4}{v_0^2}+\frac{15b^2}{v_0^2L^3}\int_0^L f(x)\,dx-\frac{15}{v_0^2L^3}\left(\frac{3b^2}{L^2}-1\right)\int_0^L x^2f(x)\,dx-\frac{45}{v_0^2L^5}\int_0^L x^4f(x)\,dx\end{aligned}\tag{5}$$

If $f(x)$ is of the form: $f(x)=\gamma x^2+\varphi(x)$, in which γ is determined from the condition

$$\int_0^L (f(x)-\gamma x^2)\,dx=\min_{(\gamma)}$$

that is

$$\int_0^L x^2\varphi(x)\,dx=0$$

formulae (5) will have the form:

$$\begin{aligned}\alpha&=\frac{4b^2}{v_0^2}+\frac{12}{35}\frac{L^4}{v_0^2}\gamma-\frac{3}{v_0^2L}\int_0^L\left(3b^2-\frac{5}{L^2}x^4\right)\varphi(x)\,dx\\ \beta&=\frac{4}{v_0^2}[1-(b^2+6/7L^2)\gamma]+\frac{15}{v_0^2L^3}\int_0^L\left(b^2+\frac{3}{L^2}x^4\right)\varphi(x)\,dx\end{aligned}\tag{6}$$

When the residual $\varphi(x)$ can be neglected, the CDP traveltime curve takes the form of Eq. (4), and for t_0 and V_{CDP} the following simple forms are obtained:

$$t_0=2b/v_0\tag{7}$$

$$V_{CDP}=\frac{v_0}{\sqrt{1-(b^2+6/7L^2)\gamma}}\tag{8}$$

Expressions (7) and (8) permit one to draw comparisons between the methods for solving the inverse kinematic problem in the case of such inhomogeneous media which can be described by formula (4). Already this makes it possible to clarify several features of such solutions. In the case of more complex media analogous relationships can be found if the terms of x^4, x^6, etc. are "taken out" consistently from function $\varphi(x)$, and then they are taken into consideration in formula (6). In order to be able to apply relations (7) and (8), a knowledge of the domain of the variations of the coefficient γ is necessary. For this purpose, first of all, on differentiating traveltime curve (4) we get:

$$[t''(0)]^{-1} = \frac{t_0 v_0^2}{1 - b^2\gamma}$$

As is well-known, $[t_0 t''(0)]^{-1/2}$ is the limiting value of the effective velocity v_e thus

$$v_e = \frac{V_0}{\sqrt{1 - b^2\gamma}} \tag{9}$$

The relationship between the parameters of the section and v_e are known for models of homogeneous layers with curved interfaces [GOLDIN 1979]. This allows us, in principle, to obtain similar relationships for parameter γ expressed by v_e from formula (9). Another possibility is to estimate the values of γ directly from the CDP traveltime curve. In fact, if we write down relationship (8) for two offsets L_1 and L_2, and express γ from them we get:

$$\gamma = \frac{1 - c^2}{(1 - c^2)b^2 + 6/7(L_2^2 - L_1^2)}$$

where

$$c = \frac{V_{\text{CDP}}(L_1)}{V_{\text{CDP}}(L_2)}$$

Thus γ depends on V_{CDP} which is a function of the offset. The values of b necessary for computing γ can be estimated as $0.5 t_0 V_{\text{CDP}}$ as we show in the following.

These results will be utilized, first of all, to compare the several methods used for solving the inverse kinematic problem. All of these start from the supposition of local homogeneity of the medium when initial data correspond to an inhomogeneous layer. But first, we discuss these methods in detail.

3. Two principles for solving the inverse kinematic problem in homogeneous media

The basic laws of geometrical seismics are Bendorf's* law and Snell' s law, both of them offering independently the possibility to solve the inverse problem in homogeneous media. It is true that with Bendorf's law one still needs the supposition of plane interfaces but this is not a strong constraint because geologically it is often justifiable and the form of the CDP traveltime curve does not depend strongly on the curvature of the reflector. Therefore, if the velocity is constant and the reflector is plane, then using Bendorf's law the traveltime of the wave from the source point to the registration point can be expressed as a function of their co-ordinates and of the three parameters of the medium, viz. the velocity of the layer, the depth, and the dip of the reflector. Three equations are enough to determine the unknown parameters. In the simple case of a horizontal surface these equations transform into the equation of a traveltime curve whose parameters can be converted into the parameters of the medium. The initially set-up problem, which presumes the solution of the non-linear equations based on the parameters of the medium, proves to be useful if computation is carried out according to the algorithm of layer-by-layer computation. In fact, the curvature of intermediate interfaces and the collapse of the structure of the CDP traveltime curve fail to allow the application of the explicit equation of the traveltime curve in reducing the initial data to the surface of the subsequent layer. Formula (2), in which it is assumed that $f(i) \equiv 0$ for a homogeneous layer, permits one, however, to set up a relationship between the arrival time of the wave reflected from the interface $z = kx + b$ and the parameters k, b, and the velocity $\bar{v}$ for every position of the source and the receiver. A series of such equations for various source–receiver pairs in which parameters k, b and $\bar{v}$ are a priori assumed to be the same, constitute such a system from the solution of which estimates for the required parameters can be obtained. The system of equations is usually overdetermined and its solution is achived by the least-squares method. In principle, this is equivalent with that procedure in which the parameters of the traveltime curve are converted into the parameters of the medium, smoothing beforehand the observed arrival times by the least-squares method. The solution of the inverse problem derived from Bendorf's law by the method of proceeding from layer to layer is called the R-method in the following.

Let us return to the observation carried out on the surface, since all formulae take a simpler form in this case and they are easily interpreted. Then, the solution to the inverse problem can be obtained by the following formulae: the tangent of the dip of the reflector is $k = 0.5\, t_0 V_{CDP}$, the (vertical) depth to the reflector is $H = 0.5\, t_0 V_{CDP}$. Accordingly, the (x, z) co-ordinates of the reflecting point of the normal ray are

*Bendorf's law: $dt/dl = p$, where l = offset, p = ray parameter: $\frac{V_i}{V_{i+1}}$

$$(x, z) = \left(x_0 - \frac{Hk}{1+k^2}; \frac{H}{1+k^2}\right),$$

where x_0 is the co-ordinate of the centre point of the CDP traveltime curve.

The solution of the inverse problem based on Snell's law in a homogeneous layer has its foundation in the following conception. Consider the point of the CDP traveltime curve at a distance of $2x$. Denote by $mx+n$ the tangent to the reflecting interface at the reflecting point, by α the angle of the incident ray with the surface, and by β that of the emerging ray.
The following relationships hold:

$$\sin\alpha = -\frac{1}{\sqrt{1+m^2}}\,\frac{x-mn}{\sqrt{x^2+n^2}}$$

$$\sin\beta = \frac{1}{\sqrt{1+m^2}}\,\frac{x+mn}{\sqrt{x^2+n^2}}$$

The following three equations can be set up for the unknown parameters m, n and v of the medium:

$$\begin{aligned}
\frac{\sin\beta}{v} - \frac{\sin\alpha}{v} &= \frac{2}{\sqrt{1+m^2}}\,\frac{x}{\sqrt{x^2+n^2}}\,\frac{1}{v} = A \\
\frac{\sin\beta}{v} + \frac{\sin\alpha}{v} &= \frac{2}{\sqrt{1+m^2}}\,\frac{mn}{\sqrt{x^2+n^2}}\,\frac{1}{v} = B \\
\frac{1}{v}\,\frac{2}{\sqrt{1+m^2}}\,\sqrt{x^2+n^2} &= t
\end{aligned} \tag{10}$$

The quantities $(\sin\alpha)/v$ and $(\sin\beta)/v$ are known for the layer in question since according to Snell's law they are equal to the corresponding ratios of the upper layer, the parameters of which are known similarly to the angles of emergence. On the surface, their values are equal to the derivatives of the traveltime curves taken at the reciprocal points. Therefore this method of solving the inverse problem is called the method of reciprocal points [Urupov and Levin 1985]. The quantities A, B and t (the traveltime of the wave for a given raypath) are to be measured. Let us introduce the following notation:

$$w = \frac{1}{v\sqrt{1+m^2}}$$

Then $w = V_{\mathrm{CDP}}^{-1}$. The solution to the system of equations (10) is given by the relations:

$$w = 0.5\sqrt{\frac{At}{x}},$$

$$n = \sqrt{\frac{tx}{A} - x^2}, \tag{11}$$

$$m = \frac{B\sqrt{x}}{\sqrt{A}\sqrt{t - Ax}}$$

The method of reciprocal points and the *R*-method apply Snell's and Bendorf's laws in their "pure form". In addition to these, there are other well-proven methods in practice, which take both laws into consideration at the same time, e.g. the iterative method [GOLDIN 1979]. Since each of the two laws is individually capable of solving the inverse problem, their joint use may lead to contradictions (the corresponding equations are inconsistent) if the homogeneous model is not an appropriate choice for the real medium, or the initial data are subject to errors. As usual, the elimination of this difficulty is achieved by solving the equations by the least-squares method. Thus, we possess the explicit formulae for the solution of the inverse problem by the *R*-method and by the method of reciprocal points, both of which express the required parameters of the medium by the functionals t_0, V_{CDP}, t_0' of the observed time field. Obviously the solution obtained will be suitable if the initial data correspond to that medium for which the formulae have been derived. Otherwise (i.e. if the layer is inhomogeneous), errors appear, which can be estimated by taking into account the explicit expressions derived for inhomogeneous media from the initial data. In order to avoid further technical difficulties, "the most simple" inhomogeneous model ($f(x) = \gamma x^2$) will now be considered again remembering once more the fact that those traveltime curves which are considered to be "realistic" are described in such a way in many models.

4. Comparison of the solutions obtained by the method of reciprocal points and the *R*-method for inhomogeneous layers

Assume that the primary data correspond to an inhomogeneous layer. It is clear even qualitatively, that the local solutions of the two methods (at the centre of the CDP traveltime curve) will differ from each other. In fact, in the *R*-method the solution is obtained from the values of t_0, t_0' and V_{CDP} belonging to the point studied, while the variation of V_{CDP} in the vicinity of this point is ignored by the formula. With the method of reciprocal points, however, the derivatives of the traveltime curves for common shotpoints are necessary to compute the angles of emergence of reciprocal rays, i.e. adjacent CDP traveltime curves have to be processed. This fact becomes evident especially if the derivatives are replaced by finite differences (which is practically compulsory due to

the discrete sampling in the seismic observation). Then, it is obvious that in the computation of the required derivatives so many neighbouring CDP traveltime curves are involved as many points are taken in the approximation by finite differences. Consequently, in the solution of the inverse problem by the method of reciprocal points the quantity V'_{CDP} is additionally taken into consideration as well. In other words, the two methods manipulate the same "common block" of data in a different manner.

Next, let us derive the necessary quantitative connections for that case when the CDP traveltime curve $t(x)$ is described by formula (4).
According to the well known relation

$$\frac{\sin\beta}{v} - \frac{\sin\alpha}{v} = \frac{\mathrm{d}t(x)}{\mathrm{d}x}$$

from which it is obtained that

$$A = \frac{\sin\beta}{v} - \frac{\sin\alpha}{v} = \frac{4}{v_0^2}\,\frac{x(1-b^2\gamma-2\gamma x^2)}{t}$$

Substituting the expression for A into the first formula of Eq. (11) we get:

$$V_{CDP} = \frac{v_0}{\sqrt{1-(b^2+2x^2)\gamma}} \tag{12}$$

The quantity V_{CDP} is not a final parameter in the method of reciprocal points, it is rather an intermediate computation result. Once V_{CDP} is known the ratio of the estimates of the layer velocity $\tilde{V}$ and the cosine of the dip of the layer ($\cos\tilde{\varphi}$), is known as well. First of all, it can be seen from formula (12), that this ratio is a function of the spread length x, from which the parameters of the layer can be derived. Then a comparison of (12) with (8) shows that the spread length is multiplied by 2 in the first formula and by 6/7 in the second one. For this reason the ratio $\hat{V}/\cos\hat{\varphi}$ ($\hat{V}$ and $\cos\hat{\varphi}$ are estimated by the R-method) is not equal to $\tilde{V}/\cos\tilde{\varphi}$, hence the equalities $\hat{V}=\tilde{V}$ and $\hat{\varphi}=\tilde{\varphi}$ are not valid simultaneously. Thus, if $\gamma\neq 0$, the method of reciprocal points and the R-method supply different layer parameters, which are the more different, the more inhomogeneous the medium. As mentioned already, the layers selected for solving the inverse problem are a priori to be regarded as inhomogeneous ones. Even so, not every kind of inhomogeneity necessarily leads to the erroneous determination of the layer parameters. For instance, if the first layer in Fig. 2 is regarded to be homogeneous and the inverse problem is solved under this assumption, then the dip and depth of the interface are retrieved with fairly good accuracy. In other cases, the situation may be different — much depends on the velocity gradient, on the curvature of intra-layer bedding and its conformity or unconformity, and on the combination of these and other factors. Therefore, for every solution of the inverse problem it is important to know whether or not the model may be regarded to consist of homogeneous layers. This is the task of indentifying the medium. This fact found by us implies that

one can recognize if a layer is not homogeneous merely by the initial data without using any a priori information. From formulae (8) and (12) a conclusion opposite to this can be drawn too: from the fact, namely, that in the method of reciprocal points $\tilde{V}/\cos\tilde{\varphi}$ is identical to V_{CDP} the latter being obtained directly from the CDP traveltime curve; it follows that $\gamma = 0$. The simultaneous application of different algorithms to determine the velocity and depth data characterizing the layered model of the medium enhances the confidence in the good quality of the data obtained in those cases in which the layer was considered to be locally homogeneous. If the match is not sufficient, necessity of taking steps to increase the accuracy of the solution emerges (one way to resolve the medium into more layers is to utilize a method which takes into consideration the velocity variation within the layer, etc.).

With this approach not only can the methods for solving the inverse problem in inhomogeneous media be compared with each other but a series of other questions can be answered as well—in particular, the extent of the resulting error when the layer is considered to be homogeneous, the effect of the errors in the initial data, and the extent of errors resulting from the algorithm of the layer-by-layer computation when determining the layer parameters. Without going into detail we touch upon some relevant factors which have considerable influence on the final results.

5. Accuracy in determining the layer parameters in the layer-by-layer algorithm

First we discuss how the inhomogeneity of the layer influences the determination accuracy of the parameters in the R-method, if observation is performed on the surface. As can be seen from Fig. 1, the true co-ordinates of the reflecting point $(\xi, h(\xi))$ belonging to the normal ray are to be computed as:

$$\xi = -b\cos\omega\sin\omega$$

$$h(\xi) = b\cos^2\omega$$

(remember that point θ coincides with the origin of the co-ordinate system). As a solution to the inverse problem, we get estimates for b and ω (denote these by H and φ respectively), i.e., instead of point $(\xi, h(\xi))$ we obtain the point $(\bar{\xi}, \bar{h}(\xi)) = (-H\cos\varphi\sin\varphi, H\cos^2\varphi)$. The square of the distance between them is given by:

$$\varrho^2 = b^2\cos^2\omega + H(H-2n)\cos^2\varphi - mH\sin 2\varphi,$$

where

$$m = b\sin\omega\cos\omega, \qquad n = b\cos^2\omega$$

Considering γ as a variable, we seek for a minimum of ϱ^2 according to φ. This occurs when

$$\operatorname{tg} 2\varphi = -\frac{b \sin 2\omega}{H - 2b\cos^2\omega}$$

and it equals

$$\varrho_{\min}^2 = b^2\cos^2\omega + 0.5H[H - 2b\cos^2\omega - \sqrt{(H-2b\cos^2\omega)^2 + b^2\sin^2 2\omega}]$$

It is evident that $\varrho_{\min}$ gives a lower estimate of the distance between the actual reflecting point of the normal ray and the corresponding point resulting from the solution of the inverse problem. $\varrho_{\min}^2$ is a monotonic function of $\cos\omega$ and reaches its maximum at $\omega = 0$. In this case (if $2b > H$), $\varrho_{\min} = H - b$. In the R-method the estimates for H and φ can be obtained in the form of

$$H = 0.5\, t_0 V_{CDP}, \qquad \tan\varphi = 0.5 t_0' V_{CDP}$$

Substituting the values of t_0 and V_{CDP}—formulae (7) and (8), respectively—into the expression of H we get:

$$H = \frac{b}{\sqrt{1 - (b^2 + 6/7L^2)\gamma}}$$

The values of $H - b$ as a function of γ and b (at $L = 1.2$ km) are given below:

γ \ b (km)	1	2	3	
0.01	0.011	0.054	0.317	$H-b$ (km)
0.03	0.035	0.178	0.604	

Thus, starting from possible values of γ, the determination error in the position of the reflecting point increases inadmissibly, and rapidly with the increase of the value of b.

To demonstrate how realistic the values of γ in the table above are, consider the possibility of estimating γ on the basis of the V_{CDP} values at two points of the CDP traveltime curve L_1 and L_2 far from each other. Let $L_1 = 0$ and $L_2 = 1.2$ km, and compute the ratio of v_e and V_{CDP} for the whole spread. If $v_e/V_{CDP} = 0.98$ (i.e. they differ from each other by 2%) then at $b = 1$ km: $\gamma = 0.031$, and at $b = 3$ km: $\gamma = 0.025$. A detailed study of the formulae reported in this paper (and of other similar ones) proves that with increasing inhomogeneity and thickness of the layer the determination error in the position of the reflector may exceed several hundred metres. This actually explains why depth conversions led, as a rule, to correct results down to depths of 2–2.5 km and then the errors (proportional to the square of the layer thickness as shown by the formulae) increased. It was essentially this realization that led to the method of the layer-by-layer computation, but the foregoing conclusions remain valid even there: in creating the model from the time section, one has to be careful not to let the layers be too thick. In practice, reasonable values of b are between 1 and

1.5 km (it should be noted that the thickness is measured commonly along the normal of the reflector and is estimated by $b \cos \varphi$, where φ is the dip angle of the interface).

The method of the layer-by-layer computation of the medium parameters has the useful feature that in reducing the initial data to the upper boundary of the subsequent layer, the length of the traveltime curve decreases proportionally to its thickness and depth. In addition to this, the computed time field will be erroneous due to those errors which occur when determining the kinematic parameters of the waves, and due to those inaccuracies associated with the velocity and depth values of the upper layer. These errors are mainly of systematic character since both the initial values and the intermediate data are considerably smoothed. In order to clarify the way in which all of these factors affect the solution of the inverse problem in the subsequent layer, we turn again to the technique developed in the foregoing. The time field on the upper boundary is described by Eq. (2). If the time values t_i are subject to errors ε_i, then, in order to maintain the validity of Eq. (2) the values of $\bar{v}$ and $f(i)$ have to be modified at the interface. In other words, an error in the initial data is equivalent to a modified set of "the inhomogeneity parameters" of the layer and accurate arrival times. If the values of ε_i are small (~ 2–5 ms), $\bar{v}$ remains practically unchanged. Function $f(i)$, however, is modified considerably, especially if the offset is small. If, for simplicity, one considers a traveltime curve of the form (3), in which $f(x) = \gamma x^2$, and the time values $t(x)$ are subject to the distortions $\varepsilon(x)$, then the traveltime curve $t(x) + \varepsilon(x)$ is characterized by the parameter $\gamma = \gamma - \Delta\gamma$, in which the estimate for the major term of $\Delta\gamma$ (with an accuracy of the order of $\varepsilon(x)$) is given by the inequality:

$$\frac{5}{L^5 \cos \omega} \sqrt{\frac{1-\gamma L^2}{b^2+L^2}} \int_0^L \varepsilon(x) x^2 \, dx \leqq \Delta\gamma \leqq \frac{5}{L^5 \cos \omega} \frac{1}{b} \int_0^L \varepsilon(x) x^2 \, dx$$

As an example, if $L = 0.5$ km, $\varepsilon(x) = 0.016x^2$ (an error of 4 ms in arrival times at maximum offset), then at $b = 1$ km $\gamma = 0.05$ and if $\omega = 45°$, the value of $\Delta\gamma$ is of the order of 0.01. The consequence of such a modification of the value of γ has already been discussed when dealing with the R-method. For a choice of $L = 0.4$ km $\Delta\gamma$ will be doubled—consideration for the nonlinear relationship between $\Delta\gamma$ and L is especially important in the layer-by-layer computation.

6. Conclusions

A more thorough analysis of expression (2) shows, for concrete situations, when depth transformations are not to be carried out due to accumulation of errors, and when acceptable results can be obtained. It may happen that the errors committed in the computation of the time field performed from the surface compensate for the effects of inhomogeneity of the layer and this leads

to a more accurate determination of the layer parameters—as if the same method had been applied for a homogeneous medium and proper data.

Of course, the accumulation of errors necessarily has negative consequences and one of the resulting practical conclusions is that in some cases a compromise has to be made between the method of determining each layer from the surface and the method of the layer-by-layer computation. Just in the upper part, where the section exhibits the highest variability, it is necessary to carry out finer resolution. In the lower part, where the velocities relatively stabilize, the observation base shortens substantially, and it is thus feasible to increase the layer thicknesses or to complete the solution of the inverse problem for each layer from a certain "inner" interface. Then, the increase of the parameter b acts in a less destructive manner than do the reduction errors of the time field accumulated due to the large number of steps.

The suggested analysis is helpful in choosing the strategy for solving the inverse problem in concrete cases in the possession of suitable a priori information; a posteriori it helps in comparing the results obtained by the methods of reciprocal points and the R-method. Here one has to keep in mind that the result of the solution of the identification problem in the presence of errors in each step depends on the nature of both the medium and the errors. Deviations of the layer parameters determined by both methods imply that either the model or the initial data (or both) have to be corrected for. If the results are the same, then it is only true that parameter γ, which characterizes the time field at the upper interface of the layer, is equal to zero. However, this may also be a consequence of the fact that the true time values are distorted by errors. Then, the depth transformations are incorrect and there are no "inner" data for recognition of the situation. In such cases possibly the only argument for the reliability of the solution is that the probability of occurrence of such particularly unique errors is rather low.

REFERENCES

GOLDIN S. V. 1986: Seismic traveltime inversion. SEG Tulsa 363 p.

GOLDIN S. V. 1979: Interpretation of reflection seismic data (in Russian). Nedra 343 p.

GOLDIN S. V., SUVOROV V. D. 1977: Reflected wave hodograph applied to waves in the vicinity of points (in Russian). Geologija i Geofizika, **3**, pp. 98–105

PUZYREV N. N. 1979: Time field of reflected waves and the method of effective parameters. Nauka, Novosibirsk, pp. 192–200

URUPOV A. K., LEVIN A. N. 1985: Velocity modelling and interpretation in reflection seismics (in Russian). Nedra 287 p.

SEBESSÉG- ÉS MÉLYSÉGPARAMÉTEREK MEGHATÁROZÁSA RÉTEGZETT KÖZEGBEN VALÓS FELTÉTELEK MELLETT

V M. GLOGOVSZKIJ és G. N. GOGONENKOV

A szerzők a reflexiós szeizmika inverz kinematikai feladatának megoldási problémáit vizsgálják inhomogén közegben. CDP útidő-görbe speciális előállításának segítségével összevetik a feladat megoldására alkalmazott, a rétegek lokális homogenitásán alapuló különböző eljárásokat, a sebesség- és mélységszámításokra hibabecslést adnak, a kiindulási adatok hibáinak és a közeg inhomogenitásának függvényében. Megtárgyalják a lokálisan homogén közeg felismerésének kritériumait.

ИССЛЕДОВАНИЕ СПОСОБОВ ОПРЕДЕЛЕНИЯ СКОРОСТНЫХ И ГЛУБИННЫХ ПАРАМЕТРОВ СЛОИСТОЙ СРЕДЫ В РЕАЛЬНЫХ УСЛОВИЯХ

В. М. ГЛОГОВСКИЙ и Г. Н. ГОГОНЕНКОВ

Рассматриваются проблемы, возникающие при решении обратной кинематической задачи МОВ в неоднородной среде. С помощью специального представления годографа ОГТ сопоставляются между собой различные способы, решающие задачу в предположении о локальной однородности слоя. Оцениваются погрешности определения скоростных и глубинных параметров в зависимости от ошибок в исходных данных и степени неоднородности среды. Обсуждается новая задача об идентификации слоя как локально однородного.

GEOPHYSICAL TRANSACTIONS 1988
Vol. 33. No. 3–4. pp. 175–185

LOVE WAVE SCATTERING DUE TO A SURFACE IMPEDANCE

P. S. DESHWAL*

The paper presents a theoretical formulation for studying the problem of Love wave scattering due to the presence of a surface impedance. The displacements are obtained in terms of Fourier transforms by using the Wiener–Hopf technique. Evaluation of the Fourier integrals along suitable contours in the complex plane gives the scattered Love waves appropriate to the surface impedance. The scattered waves have a logarithmic singularity at the tip of the scatterer and behave as decaying cylindrical waves at distant points. Numerical results for the scattering coefficient close to the scatterer and the amplitude of the reflected wave versus the wavenumber have been obtained.

Keywords: Love waves, Fourier analysis, scattering, amplitude, Wiener–Hopf analysis, wavenumber

1. Introduction

It is supposed that there is a discontinuity in the free surface such that there is a thin smooth uniform distribution of matter on half of the surface $x<0$, $z=-H$ and the other half of the surface $x>0$, $z=-H$ is free. The effect of distribution of matter is such that it exerts surface traction proportional to the acceleration in a direction perpendicular to the vertical plane through the direction of propagation.

The model can be idealized to scattering of seismic waves due to irregularities or discontinuities in the upper surface of the crust. For example, rigid boundaries on the surface of the earth may resist the motion of the waves and force the particles of the material beneath it to have horizontal polarization. GREGORY [1966] studied the attenuation of Rayleigh waves due to the presence of a surface impedance; DESHWAL and GOGNA [1987] have considered the problem of diffraction of compressional waves due to surface impedance; the problem of scattering of a Rayleigh wave due to the presence of the edge of a thin surface has also been considered by SIMONS [1976]. The mathematical formulation of the present paper is based on a paper by SATO [1961] who studied the problem of propagation of Love waves for a surface layer of variable thickness.

Here, we propose to discuss the problem of scattering of Love waves due to the presence of an impeding surface. The method of solution is the application of Fourier transformation and the Wiener–Hopf technique. A time-harmonic Love wave is incident on the impeding surface ($x<0$, $z=-H$) from the region $x>0$. The discontinuity at the surface gives rise to the Love waves appropriate to the surface impedance and the waves scattered due to the impedance.

* Department of Mathematics, Maharshi Dayanand University, Rohtak—124001, India
Manuscript received: 15 August, 1987

Let us consider a layered structure with a surface layer of thickness H with its co-ordinate system at a point in the interface between the layer and a solid halfspace *(Fig. 1)*. The velocities of shear waves and rigidities are taken to be v_1, μ_1 in the solid halfspace and v_2, μ_2 in the surface layer. Let the incident wave be [SATO 1961]

$$\begin{aligned} v_{0,1} &= A\cos(\beta_{2,N} H)\exp(-\beta_{1,N} z - \mathrm{i}k_{1,N} x), \quad z \geqq 0 \\ v_{0,2} &= A\cos(\beta_{2,N}(z+H))\exp(-\mathrm{i}k_{1,N} x), \quad -H \leqq z \leqq 0 \end{aligned} \tag{1}$$

where

$$\beta_{1,N} = \sqrt{(k_{1,N}^2 - k_1^2)}, \quad \beta_{2,N} = \sqrt{(k_2^2 - k_{1,N}^2)}, \tag{2}$$

and $k_{1,N}$ is a root of the equation

$$\tan \beta_{2,N} H = \gamma \frac{\beta_{1,N}}{\beta_{2,N}}, \quad \gamma = \frac{\mu_1}{\mu_2} \tag{3}$$

The wave equation in two dimensions is

$$(\nabla^2 + k_j^2) v_j = 0, \quad j = 1, 2, \quad |k_1| < |k_2| \tag{4}$$

and

$$k_j = \sqrt{\left(\frac{\omega^2 + \mathrm{i}\varepsilon\omega}{v_j^2}\right)} = k_j' + \mathrm{i}k_j'' \tag{5}$$

$\varepsilon > 0$ is a damping constant and the displacement has a time factor $\exp(-\mathrm{i}\omega t)$. k_j is complex whose imaginary part is positive and small. We define the Fourier transforms

$$\begin{aligned} \bar{v}_j &= \int_{-\infty}^{\infty} v_j e^{\mathrm{i}px}\,\mathrm{d}x, \qquad p = \xi + \mathrm{i}\eta \\ &= \int_{-\infty}^{0} v_j \mathrm{e}^{\mathrm{i}px}\,\mathrm{d}x + \int_{0}^{\infty} v_j \mathrm{e}^{\mathrm{i}px}\,\mathrm{d}x \\ &= \bar{v}_{j-} + \bar{v}_{j+} \end{aligned} \tag{6}$$

If for given z,

$$|v_j| \sim \exp(-\mathrm{k}_1''|x|) \quad \text{as} \quad |x| \to \infty \tag{7}$$

then $\bar{v}_{j+}$ is analytic for $\eta > -k_1''$ and $\bar{v}_{j-}$ for $\eta < +k_1''$.

$\bar{v}_j$ is therefore analytic in the strip $-k_1'' < \eta < k_1''$ of the complex p plane.

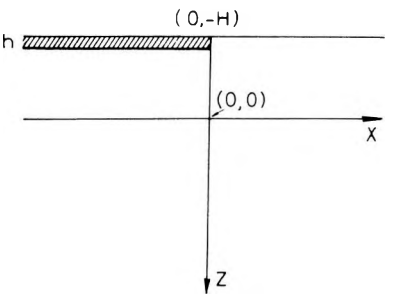

Fig. 1. The geometry of the model

1. ábra. A felvett modell

Рис. 1. Геометрия модели

2. Boundary Conditions

If the total displacements are denoted by

$$\begin{aligned} v &= v_{0,1} + v_1, \qquad z \geqq 0 \\ v &= v_{0,2} + v_2, \qquad -H \leqq z \leqq 0 \qquad -\infty < x < \infty \end{aligned} \tag{8}$$

then the conditions on the boundaries are

(i) $$v_1 = v_2 \qquad z = 0 \tag{9}$$

(ii) $$\mu_1 \frac{\partial v}{\partial z} = \mu_2 \frac{\partial v}{\partial z} \quad \text{or} \quad \gamma \frac{\partial v_1}{\partial z} = \frac{\partial v_2}{\partial z}, \qquad z = 0 \tag{10}$$

(iii) $$\mu_2 \frac{\partial v}{\partial z} = 0 \quad \text{or} \quad \frac{\partial v_2}{\partial z} = 0, \qquad z = -H, \qquad x \geqq 0 \tag{11}$$

(iv) $$\mu_2 \frac{\partial v}{\partial z} = av, \qquad \text{on} \qquad z = -H, \qquad x \leqq 0, \qquad \text{ie.,}$$

$$\mu_2 \frac{\partial v_2}{\partial z} - a[v_2 + A \exp(-ik_{1,N} x)], \qquad z = -H, \qquad x \leqq 0 \tag{12}$$

where a is a constant depending upon the nature of the material of the impeding surface. The boundary condition (12) may be interpreted as representing the physical situations that (i) there is a thin smooth uniform surface distribution of matter exerting surface traction proportional to the acceleration along a direction in the horizontal plane perpendicular to the vertical plane through the direction of propagation or (ii) at each point of the surface, there is a resisting or a restoring force proportional to the velocity along the normal to the vertical plane through the direction of propagation. GREGORY [1966] has given various explanations for this condition in the case of Rayleigh waves.

3. Solution of the problem

We begin by taking a Fourier transform of (4) to find

$$\frac{d^2 \bar{v}_j}{dz^2} - \beta_j^2 \bar{v}_j = 0, \qquad \beta_j = \pm \sqrt{(p^2 - k_j^2)} \tag{13}$$

The sign before the radical in (13) is such that the real part of $\beta_j \geqq 0$ for all p. The solution to (13) is

$$\bar{v}_1(p, z) = B(p) \exp(-\beta_1 z), \qquad z \geqq 0 \tag{14}$$

$$\bar{v}_2(p, z) = C(p) \exp(-\beta_2 z) + D(p) \exp(\beta_2 z), \qquad -H \leqq z \leqq 0. \tag{15}$$

Using the boundary conditions (9) and (10), we find

$$\bar{v}_2(p, z) = \frac{B}{\beta_2}(\beta_2 \cosh \beta_2 z - \gamma\beta_1 \sinh \beta_2 z) \tag{16}$$

$$\bar{v}_1(p, z) = \bar{v}_1(p, 0) \exp(-\beta_1 z) \tag{17}$$

$$\bar{v}_1(p, 0) = B \tag{18}$$

We use the notation $\bar{v}_1(p)$ for $\bar{v}_1(p, -H)$, etc. thus the conditions (11) and (12) result in

$$\overline{v_{2+}^r}(p) = 0 \tag{19}$$

$$\mu_2 \overline{v_{2-}^r}(p) = a\bar{v}_{2-} + \frac{aA}{\mathrm{i}(p - k_{1,N})}, \qquad \eta < \mathrm{Im}(k_{1,N}). \tag{20}$$

Adding (19) and (20), we find

$$\overline{v_2^r}(p) = \frac{a\bar{v}_{2-}}{\mu_2} + \frac{aA}{\mathrm{i}\mu_2(p - k_{1,N})} \tag{21}$$

From (16), it is obtained that

$$\bar{v}_2(p, z) = \frac{\beta_2 \cosh \beta_2 z - \gamma\beta_1 \sinh \beta_2 z}{\beta_2 \cosh \beta_2 H + \gamma\beta_1 \sinh \beta_2 H} \bar{v}_2(p) \tag{22}$$

and from here, we get

$$\overline{v_2^r}(p) = -\beta_2 \frac{\beta_2 \sinh \beta_2 H + \gamma\beta_1 \cosh \beta_2 H}{\beta_2 \cosh \beta_2 H + \gamma\beta_1 \sinh \beta_2 H} \bar{v}_2(p) \tag{23}$$

From (21) and (23), we obtain

$$\frac{a\bar{v}_{2-}}{\mu_2} + \frac{aA}{\mathrm{i}\mu_2(p - k_{1,N})} = -\beta_2 \frac{[\beta_2 \sinh \beta_2 H + \gamma\beta_1 \cosh \beta_2 H]\bar{v}_2(p)}{\beta_2 \cosh \beta_2 H + \gamma\beta_1 \sinh \beta_2 H} \tag{24}$$

We can solve the functional equation (24) for $\bar{v}_{2+}$ and $\bar{v}_{2-}$ by invoking the Wiener–Hopf technique.

Let us write

$$L(p) = \frac{F_1(p)}{F_2(p)} = \frac{\beta_2 \cosh \beta_2 H + \gamma\beta_1 \sinh \beta_2 H}{\beta_2 \sinh \beta_2 H + \gamma\beta_1 \cosh \beta_2 H} \tag{25}$$

$L(p)$ tends to 1 as $|\xi|$ tends to infinity. By an infinite product theorem [Noble 1958], $L(p)$ can be factorized. Let $\pm p_{1n}$ and $\pm p_{2n}$ $(n = 1, 2, \ldots)$ be the zeros of $F_1(p)$ and $F_2(p)$ respectively. Then

$$L(p) = \left[\prod_{n=1}^{\infty} \frac{(p^2 - p_{1n}^2)}{(p^2 - p_{2n}^2)}\right] \frac{P_1(p)}{P_2(p)} \tag{26}$$

where

$$P_1(p) = F_1(p)/\prod_{n=1}^{\infty}(p^2-p_{1n}^2)$$
$$P_2(p) = F_2(p)/\prod_{n=1}^{\infty}(p^2-p_{2n}^2) \tag{27}$$

are non-zero functions of p. Further if

$$P(p) = P_1(p)/P_2(p) = P_+(p)P_-(p) \tag{28}$$

then

$$\log P_+(p) = \frac{1}{2\pi i}\int_T \frac{\log P(\zeta)}{\zeta-p}\,d\zeta$$
$$= \frac{1}{2\pi i}\int_T \frac{\log F_1(\zeta)}{\zeta-p}\,d\zeta - \frac{1}{2\pi i}\int_T \frac{\log F_2(\zeta)}{\zeta-p}\,d\zeta \tag{29}$$
$$= \frac{1}{\pi}\int_0^{\infty}\frac{\Phi_1-\Phi_2}{u-ip}\,du - \frac{1}{\pi}\int_0^{k_1}\frac{V_1-V_2}{u+p}\,du - \frac{1}{\pi}\int_{k_1}^{k_2}\frac{du}{u+p}$$

and $P_-(p)=P_+(-p)$
where

$$\begin{aligned}
\tan\Phi_1 &= \beta\cos\beta H/\gamma\sqrt{(u^2+k_1^2)}\sin\beta H\\
\tan\Phi_2 &= \gamma\sqrt{(u^2+k_1^2)}\cos\beta H/\beta\sin\beta H\\
\tan V_1 &= \beta'\cos\beta' H/\gamma\sqrt{(k_1^2-u^2)}\sin\beta' H\\
\tan V_2 &= \gamma\sqrt{(k_1^2-u^2)}\cos\beta' H/\beta'\sin\beta' H\\
\beta &= (u^2+k_2^2)^{1/2}, \qquad \beta' = (k_2^2-u^2)^{1/2}
\end{aligned} \tag{30}$$

T is the contour shown in *Fig. 2*. Thus

$$L(p) = \prod_{n=1}^{\infty}\frac{(p^2-p_{1n}^2)}{(p^2-p_{2n}^2)}P_+(p)P_-(p) = L_+(p)L_-(p) \tag{31}$$

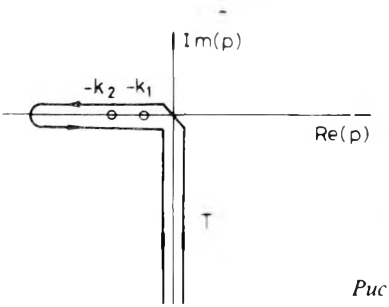

Fig. 2. Contour of integration in the complex plane

2. ábra. Az integrálási kontúr a komplex síkban

Рис. 2. Контур интегрирования в комплексной плоскости

where

$$L_{\pm}(p) = \prod_{n=1}^{\infty} \frac{(p \pm p_{1n})}{(p \pm p_{2n})} P_{\pm}(p)$$

We decompose (24) as

$$\frac{1}{L_+(p)} \left[\sqrt{(p+k_2)}\bar{v}_{2-} - \bar{v}_{2-}(-p_{1n})\sqrt{(k_2-p_{1n})}\right] + \\ + \frac{L_-(p)}{\sqrt{(p-k_2)}} \left[\bar{v}_{2-} + \frac{A}{i(p-k_{1,N})}\right] \frac{a}{\mu_2} = \\ = -\frac{\sqrt{p+k_2}\bar{v}_{2+}}{L_+(p)} - \frac{\sqrt{k_2-p_{1n}}\bar{v}_{2-}(-p_{1n})}{L_+(p)} \tag{32}$$

$\beta_2 = 0$ is not a singularity in the decomposition. The left hand member of (32) has no singularity at the zeros $p = -p_{1n}$ of $L_+(p)$ as it reduces to $\frac{0}{0}$ form. There is a pole at $p = k_{1,N}$ and branch points at $p = \pm k_2$. Therefore the member is analytic in the region $\eta \cdot \mathrm{Im}(k_1) = k_1''$, where $k_1 < k_{1,N} < k_2$. Similarly the right hand member is analytic in the region $\eta > -k_1''$. By analytic continuation, they represent an entire function analytic in the strip $-k_1'' < \eta < k_1''$ and having the value $-\sqrt{k_2-p_{1n}}\bar{v}_{2-}(-p_{1n}) = -\lambda$ as $|p| \to \infty$. By Liouville's theorem, each member in (32) has the constant value $-\lambda$.
Hence

$$\bar{v}_2(p) = -\frac{a}{\mu_2\beta_2}\left[\bar{v}_{2-} + \frac{A}{i(p-k_{1N})}\right] L(p) \tag{33}$$

where

$$\bar{v}_{2-} = \frac{\mu_2\sqrt{p-k_2}}{\mu_2\beta_2 + aL(p)}\left[\lambda - \lambda L_+(p) - \frac{aAL(p)}{i\mu_2\sqrt{p-k_2}(p-k_{1,N})}\right] \tag{34}$$

The displacement inside the layer is given by

$$v_2(x,z) = \frac{1}{2\pi}\int_{-\infty+i\eta}^{\infty+i\eta} \bar{v}_2(p,z)e^{-ipx}\,dp \\ = \frac{1}{2\pi}\int_{-\infty+i\eta}^{\infty+i\eta} \frac{\beta_2\cosh\beta_2 z - \gamma\beta_1\sinh\beta_2 z}{\beta_2\cosh\beta_2 H + \gamma\beta_1\sinh\beta_2 H}\bar{v}_2(p)e^{-ipx}\,dp \tag{35}$$

where $-k_1'' < \eta < k_1''$ and $\bar{v}_2(p)$ is given by (33).

4. Evaluation of the integral

If $a=0$ then $v_2(x, z) = 0$, i.e. if there is no impedance on the surface, there is no wave other than the incident wave. Let us evaluate the integral (35) along a closed contour in the upper part $\eta > -k_1''$ of the complex plane. In order that the integral along the contour at infinity vanishes $x<0$. There is a contribution due to the pole at $p=k_{1,N}$

$$v_{2,1} = -A\cos\beta_{2,N}(z+H)\exp(-ik_{1,N}x) \tag{36}$$

which cancels the incident wave. We have the poles of the equation $a\,L(p)+ +\mu_2\beta_2 = 0$

i.e.
$$\frac{\beta_2\cosh\beta_2 H+\gamma\beta_1\sinh\beta_2 H}{\beta_2\sinh\beta_2 H+\gamma\beta_1\cosh\beta_2 H} = -\frac{\mu_2\beta_2}{a} \tag{37}$$

Let $k_{2,N}$ ($N = 1, 2, 3, \ldots$) be a root of this equation. $k_{2,N}$ represents the Nth-mode of Love waves due to the impeding surface. If we take

$$\beta'_{2,N} = \sqrt{(k_2^2-k_{2,N}^2)}, \qquad \beta''_{1,N} = \sqrt{(k_{2,N}^2-k_1^2)} \tag{38}$$

then (37) has the form

$$\tan\beta'_{2,N}(H-h) = \gamma\beta''_{1,N}/\beta'_{2,N} \tag{39}$$

where

$$\tan\beta'_{2,N}h = a/\mu_2\beta'_{2,N} \tag{40}$$

The impeding surface behaves as a surface layer. The pole at $p=k_{2,N}$ contributes

$$v_{2,2} = -\frac{a\beta'_{2,N}}{\cos\beta'_{2,N}(H-h)}\left[\frac{\lambda(L_+(k_{2,N})-1)}{\sqrt{(k_2+k_{2,N})}}-\frac{A}{i(k_{2,N}-k_{1,N})}\right]\cdot \frac{\cos\beta'_{2,N}(z+H-h)\exp(-ik_{2,N}x)}{G(k_{2,N})} \tag{41}$$

where

$$G(p) = \frac{d}{dp}[a(\beta_2\cosh\beta_2 H+\gamma\beta_1\sinh\beta_2 H)+ +\mu_2\beta_2(\beta_2\sinh\beta_2 H+\gamma\beta_1\cosh\beta_2 H)] \tag{42}$$

These are damped Love waves appropriate to the impeding surface.

Let us now take the contour in the lower part $\eta<k_1''$ of the complex plane. It has a branch point at $p=-k_2$ and the contour includes a branch cut as shown in *Fig. 3*. The integral along the infinite circular arc vanishes if $x>0$. The branch cut is obtained by taking Real $(\beta_2)=0$ [EWING et al. 1957], and Im(β_2) changes sign along the branch cut. The contribution at the branch point $p=-k_2$ comes from its neighbourhood and we put $p=-k_2-iu$ in (35), where u is small. Since β_2 is imaginary along the branch cut, β_2^2 is negative. Therefore

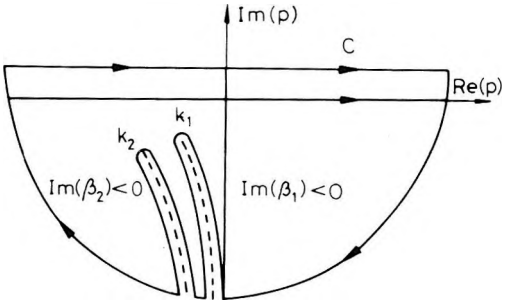

Fig. 3. The contour of integration in the complex plane with branch cuts

3. ábra. Az integrálási kontúr a komplex síkban, kettős bevágással

Рис. 3. Контур интегрирования в комплексной плоскости с двойным врезом

$$\beta_2^2 = (-k_2 - \mathrm{i}u)^2 - k_2^2 = 2\mathrm{i}u(k_2' + \mathrm{i}k_2'') - u^2 = -(2k_2''u + u^2), \qquad k_2' = 0$$

or

$$\beta_2 = \pm \mathrm{i}\beta_2', \qquad \beta_2' = \sqrt{(2k_2''u + u^2)}$$

Integrating (35) along the two sides of the branch cut, we have

$$v_{2,3} = \frac{1}{2\pi} \int_0^\infty [[\bar{v}_2(p, z)]_{\beta_2 = \mathrm{i}\beta_2'} - [\bar{v}_2(p, z)]_{\beta_2 = -\mathrm{i}\beta_2'}] e^{-k_2'' x} e^{-ux} \, \mathrm{d}u =$$

$$= -\frac{a\lambda}{\pi} e^{-k_2'' x} \int_0^\infty \left[\frac{G_1(u) \cos \sqrt{(2k_2''u + u^2)}\,(z + H)}{\sqrt{(2k_2'' + u^2)}} + \right.$$

$$\left. + \frac{G_2(u) \sin \sqrt{2k_2''u + u^2}(z + H)}{2k_2''u + u^2} \right] e^{-ux} \, \mathrm{d}u \tag{43}$$

where

$$G_1(u) = \frac{(\beta_2' \cos \beta_2' H + \gamma\beta_1' \sin \beta_2' H)\bar{\beta}_2}{\mu_2\beta_2' + aL'(u)}$$

$$G_2(u) = \frac{\beta_2'(\beta_2' \sin \beta_2' H - \gamma\beta_1' \cos \beta_2' H)\bar{\beta}_2}{\mu_2\beta_2' + aL'(u)}$$

$$L'(u) = \frac{\beta_2' \cos \beta_2' H + \gamma\beta_1' \sin \beta_2' H}{-\beta_2' \sin \beta_2' H + \gamma\beta_1' \cos \beta_2' H},$$

and

$$\bar{\beta}_2 = \sqrt{-\mathrm{i}(2k_2'' + u)}, \qquad \beta_1' = \sqrt{(k_2 + \mathrm{i}u)^2 - k_1^2}$$

Since u is small, we shall retain only $G_1(0)$ and $G_2(0)$. The integrals in (43) are Laplace integrals. We use a result obtained by OBERHETTINGER and BADII [1973], viz.

$$K_0(k_2'' r) = e^{-k_2'' x} \int_0^\infty \frac{\cos \sqrt{2k_2'' u + u^2}\,(z+H)}{\sqrt{2k_2'' u + u^2}} e^{-ux}\, du \tag{44}$$

where K_0 is the modified Hankel function of zero order and $r = \sqrt{x^2 + (z+H)^2}$. Thus

$$v_{2,3} = -\frac{a\lambda}{\pi}\left[G_1(0)\, K_0(k_2'' r) + G_2(0) \int_{-H}^{z} K_0(k_2'' s)\, dt \right] \tag{45}$$

where

$$\begin{aligned} G_1(0) &= \frac{\sqrt{2k_2''}\,(1+\gamma\bar{\beta}_1 H)\gamma\bar{\beta}_1 \exp(-i\pi/4)}{a(1+\gamma\bar{\beta}_1 H) + \mu_2\gamma\bar{\beta}_1}, \\ G_2(0) &= -\frac{\sqrt{2k_2''}\,(\gamma^2\bar{\beta}_1^2) \exp(-i\pi/4)}{a(1+\gamma\bar{\beta}_1 H) + \mu_2\gamma\bar{\beta}_1} \end{aligned} \tag{46}$$

and

$$\bar{\beta}_1 = \sqrt{(k_2^2 - k_1^2)}, \qquad s = \sqrt{(x^2 + (t+H)^2)} \tag{47}$$

Conclusions

The scattered wave in (45) and the reflected wave in (41) corresponding to the impedance surface are absent if $a = 0$, that is, if there is no impedance condition. For small values of r, $K_0(k_2'' r) \sim (\log z - \log r - c)$ and for large r, $K_0(k_2'' r) \sim \exp(-k_2'' r)/\sqrt{r}$. The scattered wave has a logarithmic singularity at the tip of the scatterer and behaves as a decaying cylindrical wave at distant points. Numerical computations are made by taking $r = 0.1$ km, $z = -H$, $h = 0.01$ km, $\gamma = \mu_1/\mu_2 = 2$, $H = 6$ km, $v_2/v_1 = 3/4$, $v_2/v = 6/7$ and $k_{1N} = k_2$. The amplitude of the reflected wave *(Fig. 4.)* has been plotted versus the wavenumber k for the case $\lambda = 0$. It reaches the greatest value around $k = 32.5$ and then falls to attain a minimum value around $k = 60$. The scattering coefficient *(Fig. 5.)* grows gradually as k increases slowly. It can be seen in (40) that it depends upon both the material and thickness of the impeding surface.

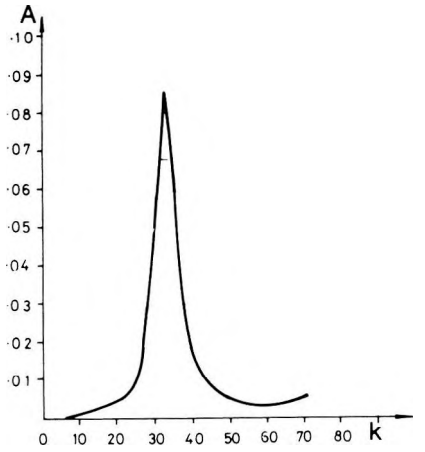

Fig. 4. Amplitude of reflected wave versus wavenumber

4. ábra. A reflektált hullámok amplitúdója a hullámszám függvényében

Рис. 4. Амплитуды отраженных волн как функция волновых чисел

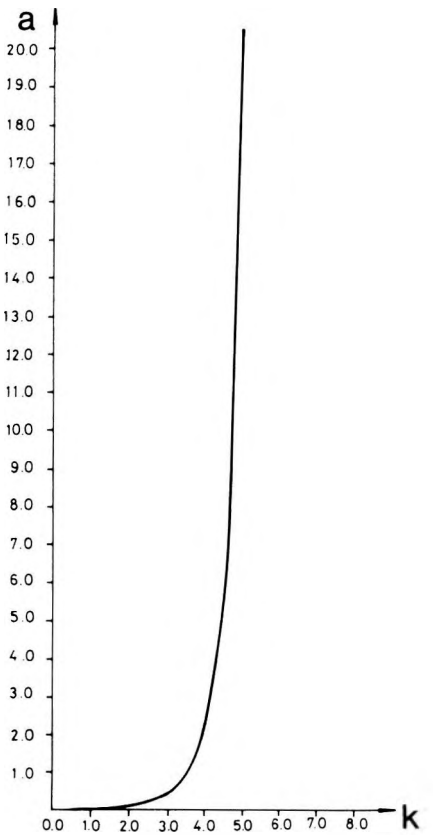

Fig. 5. Scattering coefficient versus wavenumber

5. ábra. Szórási együttható a hullámszám függvényében

Рис. 5. Коэффициенты дисперсии как функция волновых чисел

REFERENCES

DESHWAL, P. S. and GOGNA M. L. 1987: Diffraction of a compressional wave in a solid halfspace by a surface impedance. Acta Geophysica Polonica, **15**, 2. pp. 167–182

EWING W. M., JARDETZKY W. S. and PRESS F. 1957: Elastic waves in layered media. McGraw-Hill, New York, 380 p.

GREGORY R. D. 1966: The attenuation of a Rayleigh wave in a halfspace by a surface impedance, Proc. Camb. Phil. Soc., **62**, pp. 811–827

NOBLE B. 1958: Methods based on the Wiener–Hopf technique. Pergamon Press, Oxford

OBERHETTINGER F. and BADII L. 1973: Tables of Laplace Transforms. Springer Verlag, New York

SATO R. 1961: Love waves in case the surface layer is variable in thickness. J. of Physics of the Earth, **9**, 2, pp. 19–36

SIMONS D. A. 1976: Scattering of a Rayleigh wave by the edge of a thin surface layer with negligible inertia. J. Acoustic. Soc. Am., **59**, pp. 12–18

LOVE-HULLÁM SZÓRÓDÁS KIÉKELŐDŐ, NAGY AKUSZTIKUS IMPEDANCIÁJÚ VÉKONY FELSZÍNI RÉTEGEN

P. S. DESHWAL

A felszíni impedancián keletkező Love-hullám szóródás problémájának tanulmányozására elméleti megoldást javasol. Az elmozdulásokat Fourier-transzformáltakkal fejezi ki a Wiener–Hopf technika alkalmazásával. A Fourier-integráloknak a komplex síkban alkalmas vonalak mentén történő kiszámításával megadja a felszíni impedanciának megfelelő szórt Love-hullámokat. A szórt hullámoknak a szórási felület csúcsán logaritmikus szingularitásuk van és úgy viselkednek, mint csillapodó hengeres hullámok távoli pontokban. A szórási felület közelében a szórási együtthatóra és a reflektált hullám amplitúdójára numerikus eredményeket ad a hullámszám függvényében.

ДИСПЕРСИЯ ВОЛН ЛАВА ОТ ВЫКЛИНИВАЮЩЕГОСЯ ПРИПОВЕРХНОСТНОГО СЛОЯ С ВЫСОКИМ АКУСТИЧЕСКИМ ИМПЕДАНСОМ

П. С. ДЕШУОЛ

Предлагается теоретическое решение проблемы дисперсии волн Лава, возникающих на приповерхностном импедансе. Смещения выражаются грансформантами Фурье с использованием техники Винера–Гопфа. Путем вычисления интегралов Фурье вдоль подходящих линий в комплексной плоскости определяются рассеянные волны Лава, соответствующие импедансу на поверхности. На вершине поверхности дисперсии рассеянные волны обладают логарифмической сингулярностью и ведут себы так, как затухающие цилиндрические волны в удаленных точках. Даются цифровые результаты как функция волновых чисел для коэффициента дисперсии и амплитуды отраженных волн вблизи от поверхности дисперсии.

GEOPHYSICAL TRANSACTIONS 1988
Vol. 33. No. 3–4 pp. 187–210

SEISMIC MIGRATION WITH ELIMINATION OF SPHERICAL DIVERGENCE

Andrzej KOSTECKI*

The present paper verifies the relations between conventional migration and Born's inversion represented by the derivative of the function describing velocity changes in the direction normal to the boundary separating media of different velocities. A new migration algorithm for zero offset seismic sections is proposed in order to eliminate the spherical divergence from the whole frequency band. The high frequency approximation of the proposed algorithm converges to the Cohen–Bleistein algorithm except for a constant irrespective of the latter being used for Kirchhoff's or f–k migration. Properties of high frequency approximations are visualized by performing the computations for 2-D and 3-D models of synthetic wave fields.

Keywords: seismic methods, migration, two-dimensional models, three-dimensional models, spherical divergence, seismic inversion

1. Introduction

During the last few years one can observe the intense development of seismic migration methods. The fundamental principle of seismic migration formulated by CLAERBOUT and DOHERTY [1972] has become an inspiration for novel ways of extrapolating the wave field measured on the surface below the earth's surface. In 1976 LOEWENTHAL et al. proposed the idea of exploding reflectors. This idea assumed that wave sources are located along reflection boundaries and that they became actuated at the same moment $t=0$. For such a case it was also assumed that the zero offset time section corresponds to the propagation of waves whose velocity is equal to half the genuine velocity. This principle significantly contributed to the development of numerous novel methods of two- and three-dimensional migration [SCHNEIDER 1978, STOLT 1978, GAZDAG 1980].

Starting with a wave equation with the velocity being a function of the spatial coordinates, COHEN and BLEISTEIN [1979] proposed the new method of mapping the subsurface. Their method consisted in defining velocity changes with respect to a constant reference velocity. These velocity changes are blamed for creating a secondary seismic field. The solution obtained is valid only for proportionately small velocity variation and when the Born approximation has been applied, i.e. when the total wave field has been substituted by the one with constant wave velocity and homogeneous medium. The result is a solution of

* Oil and Gas Institute, 31–503 Cracow, Lubicz 25a, Poland
Manuscript received (revised version): 2 November, 1987

Fredholm's integral equation of the first kind and it defines velocity changes based on seismic data recorded by means of the CMP method. In 1982 BLEISTEIN and COHEN reduced the problem of velocity changes to one that defines the source density in a wave equation where the source or initial value has been modelled by geometrical reflection coefficients multiplied by the Dirac function indicating the reflection boundary. Similar considerations are also quoted in [BLEISTEIN et al. 1985] where several details on how to compute the integral relations in asymptotic expressions are discussed. This paper also demonstrated that the high frequency approximation provides information both on structure and on reflecting properties.

A generalized solution of COHEN and BLEISTEIN [1979] for unstacked data has been obtained by RAZ [1981] who succeeded in mapping both velocity and density. In his later paper RAZ [1982] applied the Bremmer-like inversion procedure for a three-dimensional stacked CMP section. The physical assumptions behind the inverse solutions (with respect to reference velocity) are thoroughly discussed in the literature. CLAYTON and STOLT [1981] generalized the Raz procedure making it applicable to a slowly changing layered medium with plane interfaces instead of a homogeneous halfspace. In his detailed work BERKHOUT [1984] thoroughly discussed the relation between seismic migration and multidimensional linearized inversion and provided a condition for the identity of these processes. COHEN and HAGIN [1985] presented the velocity inversion algorithms which take into account results obtained when the depth-dependent velocity function was assumed to be the reference velocity. The mutual relation between Born inversion and migration for CMP time sections has been thoroughly considered by CHENG and COEN [1984] who proved that the Cohen–Bleistein inverse problem may be regarded as migration for modified surface data. The problem of how to define the small velocity variations based upon the non-homogeneous wave equation has also been solved by ALEKSEEV et al. [1981] and TSIBUL'CHIK [1981].

The author of the present paper presenting the procedure for defining velocity changes, has compared the computational data for f–k migration and source density function [KOSTECKI 1983]. Further a comparison has been made for an inclined boundary, and the sources are modelled by Dirac function [KOSTECKI 1986]. Here, I provide an analysis of the relationship between Born velocity inversion and migration as well as proposing a modified migration algorithm which eliminates the spherical divergence. The high frequency approximation of the proposed algorithm converges to the Cohen–Bleistein solution (except for a constant). Some results of investigations are presented using two- and three-dimensional models of wave fields.

2. Theoretical considerations

Considering the scalar seismic wave field being recorded for coincident source-receiver point (zero offset data) within heterogeneous halfspace $z>0$

(Fig. 1.) we can get the following relation between backscattered signal $F(x, y, 0, \omega)$ at the surface ($z=0$) and the change of velocity defined by the function $\alpha(x_0, y_0, z_0)$:

$$\frac{\partial}{\partial\omega}\left\{\frac{F(x, y, 0, \omega)}{\omega^2}\right\} = \frac{-\mathrm{i}}{8\pi^2 V^3}\iint_U \int_{z_0>0} \alpha(x_0, y_0, z_0)\,\frac{\mathrm{e}^{-\mathrm{i}\frac{2\omega R_s}{v}}}{R_s}\,\mathrm{d}x_0\,\mathrm{d}y_0\,\mathrm{d}z_0 \qquad (1)$$

where:

x, y, z = Cartesian coordinates; f = frequency; $\mathrm{i} = \sqrt{-1}$; $\omega = 2\pi f$; $R_s = [(x-x_0)^2 + (y-y_0)^2 + z_0^2]^{1/2}$

$$\alpha(x_0, y_0, z_0) = \frac{V^2}{V^2(x_0, y_0, z_0)} - 1 \qquad (2)$$

where:

$V(x_0, y_0, z_0)$ = velocity of P-waves within region U expressed as a function of coordinates x_0, y_0, z_0;

V = constant reference velocity.

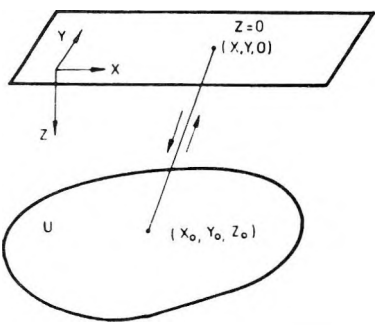

Fig. 1. Sketch showing the seismic field measurement at point (x, y, z) with zero offset from a three-dimensional point source. U denotes the heterogeneous medium with velocity being the function of position $V(x_0, y_0, z_0)$

1. ábra. Vázlat a szeizmikus mérés geometriai elrendezésére. Mérés a 3-dimenziós pontforráshoz képest 0 eltolással, az (x, y, z) pontban. U jelöli a helytől függő, $V(x_0, y_0, z_0)$ sebességű heterogén közeget

Рис. 1. Схема геометрии сейсмических измерений. Измерения с нулевым сдвигом по отношению к трехразмерному источнику, в точке (x, y, z). U — неоднородная среда со скоростями $V(x_0, y_0, z_0)$, зависящими от положения в пространстве.

Relation (1) is obtained from the original formulae of BLEISTEIN et al. [1985, p. 1255] by changing the sign of the exponent of Green's function. The solution of the first order Fredholm integral equation (1) with respect to the unknown $\alpha(x_0, y_0, z_0)$ function has been obtained within the domain of wavenumber and frequency provided that wave field $F(x, y, 0, \omega)$ is defined within $-\infty < x, y, \omega < +\omega$ (see Appendix A). This solution has the form:

$$\alpha(x_0, y_0, z_0) = -\frac{2V}{\pi^2}\int_{-\infty}^{+\infty}\int\int\int \omega \frac{\partial}{\partial\omega}\left\{\frac{F(k_x, k_y, 0, \omega)}{\omega^2}\right\} e^{ik_z z_0} e^{i(k_x x_0 + k_y y_0)}\, dk_x\, dk_y\, d\omega \quad (3)$$

where:

k_x, k_y, k_z = components of wave vector $|\vec{k}| = (k_x^2 + k_y^2 + k_z^2)^{1/2} = \frac{2\omega}{V}$ and $F(k_x, k_y, 0, \omega)$ is the Fourier transform of function $F(x, y, 0, t)$ i.e.

$$F(k_x, k_y, 0, \omega) = \int_{-\infty}^{\infty}\int\int\int F(x, y, 0, t)\, e^{-i(k_x x + k_y y + \omega t)}\, dx\, dy\, dt \quad (4)$$

In the space–time domain the Fourier transform has the form of the Kirchhoff integral

$$\alpha(x_0, y_0, z_0) = 8V\frac{\partial}{\partial z_0}\int_{-\infty}^{+\infty}\int \left.\frac{2t\int_0^t F(x, y, 0, \tau)\, d\tau - \int_0^t \tau F(x, y, 0, \tau)\, d\tau}{R_s}\right|_{t=\frac{2R_s}{V}} dx\, dy \quad (5)$$

where: τ is an integration variable.

The direct relations between Born's inversion represented by function $\alpha(x_0, y_0, z_0)$ and the migrated wave field $F(x_0, y_0, z_0, t = 0) = F(x_0, y_0, z_0)$ can be obtained from Eqs. (3) and (4). Appropriate calculations are given in detail by CHENG and COEN [1984] who also provided the test data from wave field models. However, no $\alpha(x_0, y_0, z_0)$ function was calculated but its derivative with respect to the z_0 and x_0 coordinates for a two dimensional model.

As suggested by BLEISTEIN et al. [1985] it is more advisable to use the derivative normal to the reflection boundary $\frac{\partial\alpha}{\partial\vec{n}}$ which can be done by multiplying the integral function by wave vector k ($\vec{n}$ — vector normal to the reflector). Based upon Eq. (3) we can create the $\beta(x_0, y_0, z_0)$ function by multiplying the integral function by the factor $i\frac{2\omega}{V}$ [BLEISTEIN et al. 1985]:

$$\beta(x_0, y_0, z_0) = -\frac{i4}{\pi^2}\int_{-\infty}^{+\infty}\int\int\int \omega^2 \frac{\partial}{\partial\omega}\left\{\frac{F(k_x, k_y, 0, \omega)}{\omega^2}\right\} e^{ik_z z_0} e^{i(k_x x_0 + k_y y_0)}\, dk_x\, dk_y\, d\omega \quad (6)$$

After some rearrangement of terms (see Appendix A) the function can be expressed in the form of Kirchhoff's integral:

$$\beta(x_0, y_0, z_0) = 16 \frac{\partial}{\partial z_0} \int_{-\infty}^{+\infty} \int \frac{\left[2 \int_0^t F(x, y, 0, \tau)\, d\tau + tF(x, y, 0, t) \right]}{R_s} \Bigg|_{t = \frac{2R_s}{V}} dx\, dy \qquad (7)$$

The $\beta(x_0, y_0, z_0)$ function (Eq. 7) has two components. The first component containing $\int_0^t F(x, y, 0, \tau)\, d\tau$ denotes the integration of the wave field of each seismic trace (zero offset data) within the time interval $\left[0, t = \frac{2R_s}{V}\right]$ and, afterwards, summing up the results over the hyperbolic surface defined by the length of radius R_s. The first component corresponds to the low frequency filter (see Appendix A, relation A 16) applied to the $F(x, y, 0, \omega)$ Fourier transform of the wave field recorded over the surface ($z = 0$).

The second component in Eq. (7), when compared with the standard Kirchhoff migration [SCHNEIDER 1978]:

$$F(x_0, y_0, z_0, t = 0) = -\frac{1}{2\pi} \frac{\partial}{\partial z_0} \int_{-\infty}^{+\infty} \int \frac{F\left(x, y, 0, t = \frac{2R_s}{V}\right)}{R_s} dx\, dy \qquad (8)$$

represents a migration carried out over a seismic field modified by multiplying the observed field by double the time of wave propagation $t = \frac{2R_s}{V}$. Because R_s is the radius of curvature of a spherical wavefront in a homogeneous medium and double its value is the geometrical spreading factor, the operation of multiplying the wave field by double the arrival time of reflections means that the influence of that factor has been compensated. When comparing the second component with the first one, the latter may be regarded as the high frequency response (see Appendix A, relation A 9) and in the wavenumber frequency domain the corresponding relation has the form:

$$\beta_h(x_0, y_0, z_0) = -\frac{i4}{\pi^2} \int_{-\infty}^{+\infty} \int \int \frac{\partial}{\partial \omega} \{F(k_x, k_y, 0, \omega)\}\, e^{ik_z z_0}\, e^{i(k_x x_0 + k_y y_0)}\, dk_x\, dk_y\, d\omega \qquad (9)$$

Eq. (9) is a high frequency approximation of function $\beta(x_0, y_0, z_0)$ (relation 6).

As can easily be observed, relation (9) is analogous to conventional f–k migration — the only difference being that the Fourier transform of the seismic field recorded on the surface ($z = 0$) $F(k_x, k_y, 0, \omega)$ has been substituted by its derivative with respect to ω. In an attempt to find a relation between the velocity

inversion [COHEN and BLEISTEIN 1979] described by Eq. (6) [BLEISTEIN et al. 1985] and conventional f–k migration let us notice that the migrated seismic field $F(x, y, z, t = 0) = F(x, y, z)$ may be regarded to be the effective source distribution either in a non-homogeneous scalar wave equation [see for instance CHENG and COEN 1984]

$$\left(\nabla^2 - \frac{4}{V^2}\frac{\partial}{\partial t^2}\right) F(x, y, z, t) = -\frac{8}{V^2} F(x, y, z)\delta'(t) \tag{10}$$

where

∇^2 = Laplacian operator, $\delta'(t) = \dfrac{\mathrm{d}}{\mathrm{d}t}\delta(t)$;

$\delta(t)$ = Dirac function

or in the non-homogeneous Helmholtz equation obtained from (10) by Fourier transformation

$$(\nabla^2 + k^2) F(x, y, z, \omega) = -\frac{\mathrm{i}8\omega}{V^2} F(x, y, z) \tag{11}$$

where $k = \dfrac{2\omega}{V}$.

Equations (10–11) describe the propagation of waves emitted by secondary sources of $F(x, y, z)$ density, for $t = 0$. The propagation velocity is $V/2$.
In this case the $F(x, y, 0, \omega)$ solution at the surface ($z = 0$) is as follows [see MORSE and FESHBACH 1953]:

$$F(x, y, 0, \omega) = \frac{\mathrm{i}2\omega}{\pi V^2} \iiint_U F(x_0, y_0, z_0) \frac{\mathrm{e}^{-\mathrm{i}\frac{2\omega R_s}{V}}}{R_s} \mathrm{d}x_0\, \mathrm{d}y_0\, \mathrm{d}z_0 \tag{12}$$

where U, as previously, denotes the region of integration.

Assuming the integral function in (6) to be unknown and applying the reverse sequence of transformations in the same way as when solving Eq. (1) (see Appendix A, relations A1–A5) we obtain

$$\begin{aligned} &-\frac{2}{\omega} F(x, y, 0, \omega) + \frac{\partial}{\partial\omega} F(x, y, 0, \omega) = \\ &= \frac{-\omega}{16\pi^2 V^2} \iiint_U \beta(x_0, y_0, z_0) \frac{\mathrm{e}^{-\mathrm{i}\frac{2\omega R_s}{V}}}{R_s} \mathrm{d}x_0\, \mathrm{d}y_0\, \mathrm{d}z_0 \end{aligned} \tag{13}$$

Equation (13) relates the wave field recorded on the surface (left Hand side of equation 13) to the change in velocity described by function $\beta(x_0, y_0, z_0)$ which also simulates the effective source distribution. Because the wave field recorded over the surface ($z = 0$) is a result of the same operation, for high frequencies we can equate relations (12) and (13) to get the following approximate relation:

$$aF(x_0, y_0, z_0) \cong -\beta(x_0, y_0, z_0)\left(\frac{1}{R_s} + \frac{1}{\mathrm{i}kR_s^2}\right) \tag{14}$$

where $a = \dfrac{64\pi}{V}$ and $R_s = R_n$ i.e. the radius normal to the reflector for zero offset seismic sections.

Formula (14) says that the contribution of the second component within brackets, on the right-hand-side of Eq. (14), decreases when the kR_s product increases. If we take, for instance, $f = 10$ Hz and $V = 2000$ m/s for $R_s = 2000$ m then the following formula yields an error of less than 1 per cent:

$$\beta(x_0, y_0, z_0) \cong -aR_sF(x_0, y_0, z_0) \tag{15}$$

Because function $\beta(x_0, y_0, z_0)$ is a directional derivative of relative velocity changes (or more precisely — velocity raised to the second power) it does not depend on the distance between the arbitrary subsurface points where the sources are located and the surface point $z = 0$. This means that function $\beta(x_0, y_0, z_0)$ does not depend on the distance R_s. Considering relation (15), we can easily observe that the right-hand-side of Eq. (15), i.e. the product $R_sF(x_0, y_0, z_0)$, is also independent of R_s and so we can conclude that the migrated value of $F(x_0, y_0, z_0)$ is inversely proportional to R_s. The approximative formula (15) says that in the case of a single seismic reflector the high-frequency version of the Born inversion, as defined by Cohen and Bleistein, is a seismic migration in which spherical divergence has been eliminated. We now propose a new algorithm for extrapolating the surface ($z = 0$) recorded wave field downwards below the earth's surface, in the wavenumber–frequency domain:

$$P(x_0, y_0, z_0, t = 0) =$$

$$= \frac{\mathrm{i}V}{16\pi^3}\int_{-\infty}^{+\infty}\int\int\int \omega \frac{\partial}{\partial\omega}\left\{\frac{F(k_x, k_y, 0, \omega)}{\omega}\right\} \mathrm{e}^{\mathrm{i}k_z z_0}\,\mathrm{e}^{\mathrm{i}(k_x x_0 + k_y y_0)}\,\mathrm{d}k_x\,\mathrm{d}k_y\,\mathrm{d}\omega \tag{16}$$

The proposed algorithm is believed to replace the Cohen–Bleistein inversion defined by Eqs. (6) and (7).

If we express relation (16) in the form of Kirchhoff's integral (in the same way as in Eq. A 7) then, taking into account equations (A 8—A 9) and (A 16), we shall get the relation:

$$P(x_0, y_0, z_0, t = 0) = \frac{-V}{4\pi}\frac{\partial}{\partial z_0}\int_{-\infty}^{+\infty}\iint \frac{\int_0^t F(x, y, 0, \tau)\,\mathrm{d}\tau + tF(x, y, 0, t)}{R_s}\Bigg|_{t=\frac{2R_s}{V}} \mathrm{d}x\,\mathrm{d}y \tag{17}$$

It is easy to note that relation (17) contains the same components as Eq. (7), the only difference being that the function under the integral has no multiplying factor of 2 before low frequency component $\int_0^t F(x, y, 0, \tau)\,d\tau$. When analysing equation (16), which describes the proposed migration algorithm, we can derive (see Appendix B) the following formula which relates conventional migration with the proposed one:

$$P(x_0, y_0, z_0, t = 0) = P(x_0, y_0, z_0) = R_s F(x_0, y_0, z_0) \tag{18}$$

Formula (18) bears evidence that the spherical divergence has effectively been eliminated. That is why the seismic field extrapolation method described by Eqs. (16) and (17) is named "migration with elimination of spherical divergence".

High frequency approximation of "migration with spherical divergence elimination" can be expressed as follows:

$$P_h(x_0, y_0, z_0) \cong \frac{iV}{16\pi^3} \int_{-\infty}^{+\infty}\int\int \frac{\partial}{\partial\omega}\{F(k_x, k_y, 0, \omega)\}e^{ik_z z_0}e^{i(k_x x_0 + k_y y_0)}\,dk_x\,dk_y\,d\omega \tag{19}$$

It can be seen that relation (19) is equivalent, to the velocity inversion as defined by COHEN and BLEISTEIN [1979] and BLEISTEIN et al. [1985], except for a constant. This conclusion results directly from comparing formulae (9) and (19).

3. Testing models

In order to verify the operational applicability of approximations (9) and (19), the relations between the low- and high-frequency components in Eq. (7) have been tested for function $\beta(x_0, y_0, z_0)$ expressed in the form of Kirchhoff's integral. Experiments have been performed with zero-offset sections generated for a longitudinal syncline. A model section of three-dimensional wave field along a profile with three hodographs is shown in *Fig. 2*. Modelling was performed by the ray tracing method; the discrete space steps used were: $\Delta x = \Delta y = 40$ m, $\Delta z = 0.008$ s*; the time step was: $\Delta t = 0.004$ s; the velocity in the first layer was $V_1 = 2000$ m/s, the velocity in the second layer $V_2 = 2500$ m/s. A symmetrical impulse in frequency band of 1–83 Hz was used to generate the wave field. *Fig. 3* shows the result computed according to Eq. (7) whereas *Fig. 4* presents the migrated three dimensional seismic section computed by neglecting the $\int_0^t F(x, y, 0, \tau)\,d\tau$ term. Comparison of images for both versions of migration proves that the shape of the lower part of the syncline was mapped correctly in both cases and that amplitude differences were negligible (amounts

* The depth scale is given in time

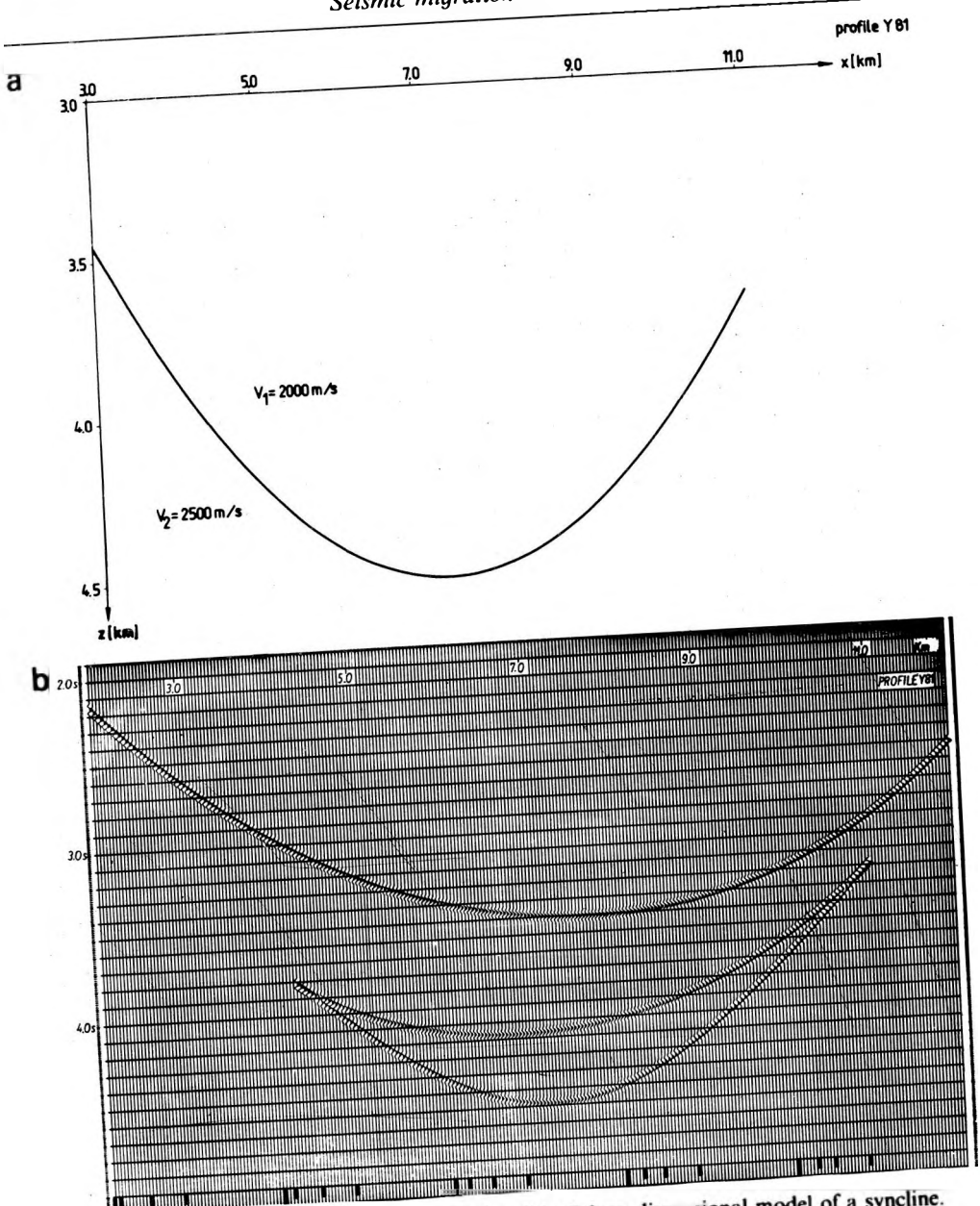

Fig. 2. Model (a) and zero-offset time section (b) of three-dimensional model of a syncline. Space and time steps: $\Delta x = \Delta y = 40$ m, $\Delta t = 0.004$ s; velocities: $V_1 = 2000$ m/s, $V_2 = 2500$ m/s

2. ábra. Egy szinklinális 3-dimenziós modelljének (a) 0-eltolású időszelvénye (b). Tér- és idő mintavétel: $\Delta x = \Delta y = 40$ m; $\Delta t = 0{,}004$ s; sebességek: $V_1 = 2000$ m/s, $V_2 = 2500$ m/s

Рис. 2. Временной профиль трехразмерной модели (а) синклинали с нулевым смещением (b) Отсчеты пространства и времени: $\Delta x = \Delta y = 40$ м; $\Delta t = 0{,}004$ с, скорости $V_1 = 2000$ м/с и $V_2 = 2500$ м/с.

to 0.2% of maximum amplitude). Amplitude fluctuations are of the same order as noises created by the application of Kirchhoff's integral. Because the spectrum of the pulse used for modelling contains the low frequency band (the zero component of a spectrum is anyway equal to zero) no great error will be made by neglecting the $\int_0^t F(x, y, 0, \tau)\,d\tau$ component. Such an approach is equivalent to the situation described by relations (9) or (19) in the wavenumber–frequency domain.

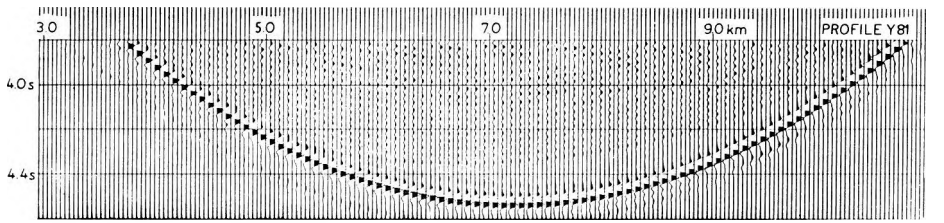

Fig. 3. Time section after migration computed according to Eq. (7). Space and time steps: $\Delta x = \Delta y = 40$ m, $\Delta z = 0.008$ s, $\Delta t = 0.004$ s

3. ábra. A (7) összefüggéssel számított migrált időszelvény. Tér és idő mintavétel: $\Delta x = \Delta y = 40$ m, $\Delta z = 0{,}008$ s, $\Delta t = 0{,}004$ s

Рис. 3. Миграционный временной профиль, рассчитанный по выражению (7). Отсчеты пространства и времени: $\Delta x = \Delta y = 40$ м, $\Delta z = 0{,}008$ с и $\Delta t = 0{,}004$ с.

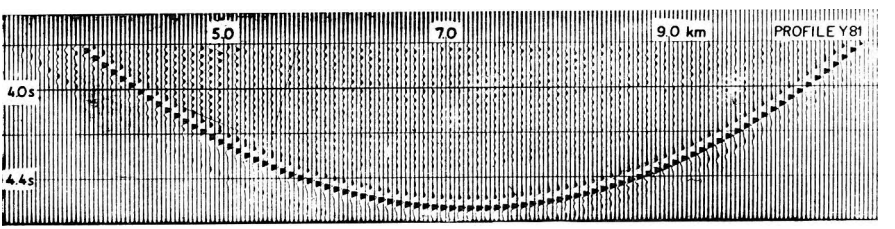

Fig. 4. Time section after migration computed according to Eq. (7) neglecting the $\int_0^t F(x, y, 0, \tau)\,d\tau$ term. Time and space steps as in Fig. 3

4. ábra. A (7) összefüggéssel számított migrált időszelvény, az $\int_0^t F(x, y, 0, \tau)\,d\tau$ tényező elhanyagolásával. Idő- és tér mintavétel a 3. ábra szerint

Рис. 4. Миграционный временной профиль, рассчитанный по выражению (7), при пренебрежении фактором $\int_0^t F(x, y, 0, \tau)\,d\tau$. Отсчеты пространства и времени — в соответствии с рис. 3.

For testing the high-frequency approximation (19) a zero offset time section was created by the ray tracing method for a 2-D reflector of 45° dip *(Fig. 5)*. The spectrum of the applied pulse was in the 1–80 Hz frequency band. The amplitude of the wave field on the surface decreases as R_n^{-1} when moving along the x axis, where R_n is the distance between the reflector and the surface measured along the normal to the reflector. We migrate this section using the conventional $f-k$ method *(Fig. 6)* and with migration described by formula (19) *(Fig. 7)*. Comparison of the two types of migration says that the amplitudes of the conventional $f-k$ migration field quickly decrease with depth whereas for migration described by Eq. (19) the amplitudes maintain a constant value over a large portion of the reflector. The solid line in *Fig. 8* presents the distribution of relative amplitudes $A(x)/A_c$ (where A_c denotes the amplitude in the centre of the reflector) as a function of horizontal coordinate x. One can observe from Fig. 8 that for 2.2–2.9 km the relative amplitudes oscillate around 1 and the maximum amplitude change does not exceed 4%. Inaccuracy in locating the amplitudes along dipping reflector $z=z(x)$ for discrete values of $\Delta z=0.004$ s leads to the oscillating character of the relative amplitude curve.

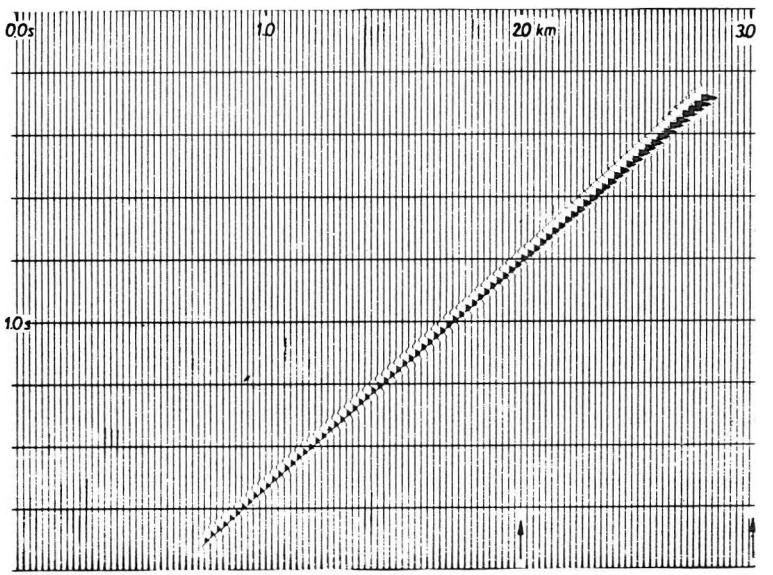

Fig. 5. Zero-offset time section of a two-dimensional reflector with 45° dip. Space and time steps: $\Delta x=25$ m, $\Delta t=0.002$ s; velocities: $V_1=2000$ m/s, $V_2=2500$ m/s

5. ábra. 45°-os dőlésű szeizmikus határfelület 0-eltolású időszelvénye. Tér- és idő mintavétel: $\Delta x=25$ m, $\Delta t=0{,}002$ s; sebességek: $V_1=2000$ m/s, $V_2=2500$ m/s

Рис. 5. Временной профиль с нулевым сдвигом сейсмической поверхности раздела, наклоненный под 45°. Отсчеты пространства и времени: $\Delta x=25$ м, $\Delta t=0{,}002$ с скорости $V_1=2000$ м/с и $V_2=2500$ м/с.

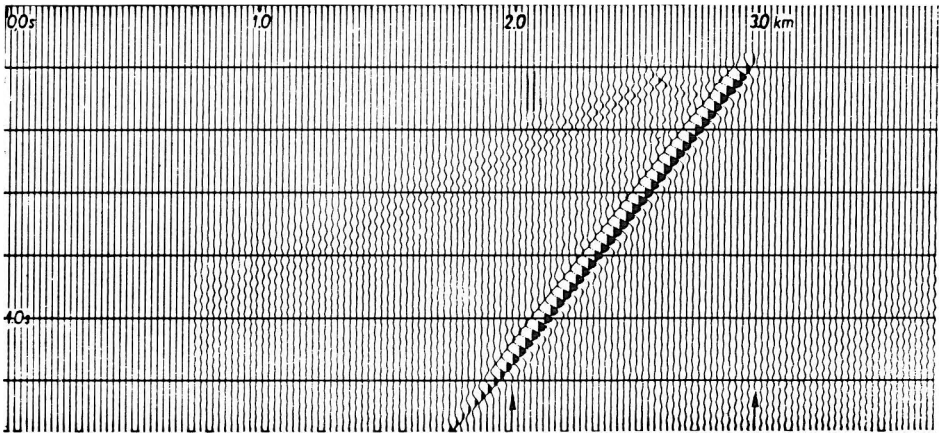

Fig. 6. Time section after conventional *f–k* migration for the wavefield of Fig.5. Time and space steps: $\Delta t = 0.002$ s, $\Delta x = 25$ m, $\Delta z = 0.004$ s. Arrows indicate end points of dipping horizon

6. ábra. f–k migráció utáni időszelvény az 5. ábrával azonos hullám térre. Idő- és tér mintavétel: $\Delta t = 0{,}002$ s, $\Delta x = 25$ m, $\Delta z = 0{,}004$ s. A nyilak a dőlt határfelület végpontjait jelölik

Рис. 6. Временной профиль волнового поля рис. 5 после *f–k* миграции. Отсчеты пространства и времени: $\Delta x = 25$ м, $\Delta z = 0{,}004$ с, $\Delta t = 0{,}002$ с. Стрелками обозначены конечные пункты наклонной поверхности раздела.

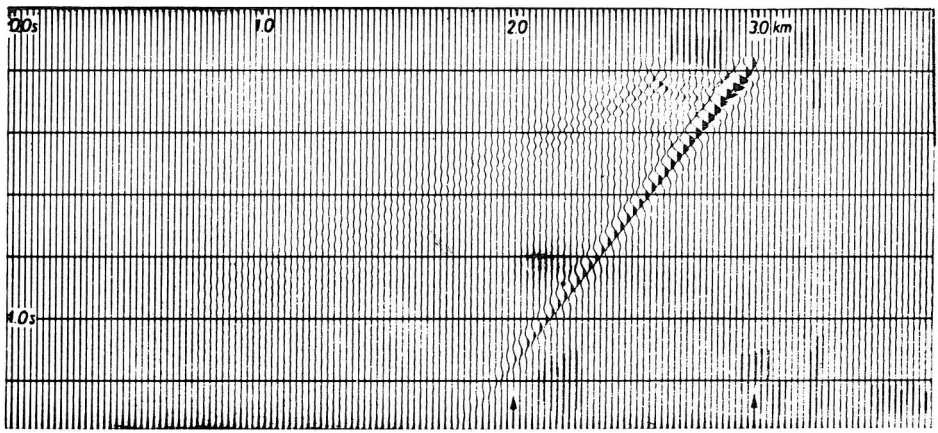

Fig. 7. Time section after *f–k* migration according to Eq. (19) for the wavefield of Fig.5. Time and space steps applied as in Fig.6. Arrows indicate end points of dipping horizon

7. ábra. A (19) egyenlettel számított *f–k* migráció utáni időszelvény az 5. ábrával azonos hullámtérre. Idő- és tér mintavétel azonos a 6. ábráéval. A nyilak a dőlt határfelület végpontjait jelölik

Рис. 7. Временной профиль волнового поля рис. 5 после *f–k* миграции по уравнению (19). Отсчеты пространства и времени — как на рис. 6. Стрелками обозначены конечные пункты наклонной поверхности раздела.

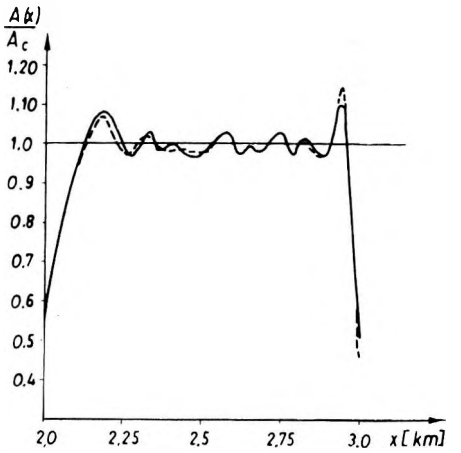

Fig. 8. Comparison of distributions of relative amplitudes $A(x)/A_c$ for both realizations of f–k migration as a function of horizontal distance x. Solid line denotes the amplitudes normed by the amplitude in the centre of the dipping horizon migrated by Eq (19); dotted line denotes relative amplitudes of conventional f–k migration multiplied by the distance (R_n) between the surface ($z=0$) and the dipping horizon measured along its normal

8. ábra. Az $A(x)/A_c$ relatív amplitúdók eloszlásának összehasonlítása az f–k migráció két változatára a vízszintes x távolság függvényében. Folytonos vonal jelöli a (19) képlettel számított migrációval nyert hullámtér amplitúdóit a dőlő határfelület középponti amplitúdójára normálva, míg a szaggatott vonal a hagyományos f–k migráció relatív amplitúdóit szemlélteti, megszorozva a felszín ($z=0$) és a dőlő határfelület közötti R_n távolsággal, amelyet ez utóbbi normálisa mentén mérünk

Рис. 8. Сопоставление распределения относительных амплитуд $A(x)/A_c$ для варианта с f–k миграцией в зависимости от горизонтальных расстояний x. Сплошной линией обозначены амплитуды волнового поля, полученного миграцией по уравнению (19), отнесенные к центральной амплитуде наклонной поверхности раздела, в то время как прерывистой — относительные амплитуды традиционной f–k миграции, умноженные на расстояние R_n между дневной поверхностью ($z=0$) и наклонной поверхностью раздела, измеренное вдоль нормали к последней

Outside the discussed interval of x one can observe two local maxima whose locations are just before the limits of the reflector. Amplitude changes in the regions mentioned are about 10 per cent higher than over the central portion of the reflector and the maxima are accompanied by distinct drops of field intensity there. These anomalies are believed to be created by boundary effects. The dotted line in Fig. 8 represents analogous distribution of migrated relative field amplitudes (conventional $f-k$ migration) where the amplitudes had been corrected in advance by multiplying them by R_n (R_n is the distance between the reflector and the observation surface measured along the normal to the reflector). As is evident from Fig. 8, the central portions of both curves are nearly coincident which proves that the spherical divergence has been effectively compensated. As far as the physics of both experiments is concerned it is easy to note that differentiating the recorded field over the surface with respect to

frequency ω is equivalent to multiplying the amplitudes by the wave propagation time $2\,R_n/V$ which makes the amplitudes equal everywhere.

Migration of the wave field with all amplitudes being equal denotes, in a given case, that the plane wave (or more precisely its segment) continues downward to the dipping reflector, i.e. to the initial position which the plane wave has at moment $t=0$. Because, in the case of plane wave propagation, there are no energy losses due to spherical divergence the equal amplitude field should be recorded over the dipping reflector at $t=0$ provided that the boundary effects associated with limited dimensions of the reflector and sampling rate were neglected.

With conventional $f-k$ migration the reflection wave field $F(x, 0, \omega)$ which decreases along the x axis as R_n^{-1}, is downward extrapolated as a flat front to the dipping reflector, all over which the migrated values of $F(x, z, t=0)$ decrease also as R_n^{-1}. The aim of the following experiment was to check the performance of the migration algorithm with eliminated spherical divergence when used for extrapolating the wave field generated for a curved seismic horizon. The experiment was carried out with zero offset wave field data for a two dimensional syncline *(Fig. 9)*. The wave field within a two layered medium characterized by velocities $V_1=2000$ m/s and $V_2=3000$ m/s was computed with the aid of the ray tracing method taking into account the geometric spreading factor. The algorithm (19) expressed in the wavenumber–frequency domain was used for downward extrapolation. *Fig. 10* presents the migrated time section. The presented image suggests that the maximum amplitude of the wave field has been equalized. This is confirmed by a relative amplitude vs. x coordinate plot *(Fig. 11)*. As in the previous experiment with a dipping reflector, the amplitude distribution has an oscillating character around 1 and maximum amplitude variations do not exceed 8 per cent over the 2.5–7.0 km interval. As previously, the variations of maximum amplitudes are caused by inaccurate location of the seismic boundary when extrapolating the wave field with steps of $\Delta z=0.004$ s. The experiment with conventional $f-k$ migration *(Fig. 12)* of the same time section has also been performed for comparison. As expected, conventional $f-k$ migration yields the correct shape of the two-dimensional syncline whereas the amplitudes of the migrated field exhibit considerable changes (about 80%) when compared to the hodograph amplitude changes (Fig. 9).

4. Discussion and conclusions

Interpretation of migrated data with eliminated spherical divergence should not create problems with a syncline-like boundary. Suffice to note that migration is considered as the process of moving the waves back (from the recording surface $z=0$ to the reflector for $t=0$) along the same path which the wave travelled from the source to the surface. The process of backward movement of waves is equivalent to compensation of wave front curvature changes shaped by a curved boundary and thus the process of conventional migration

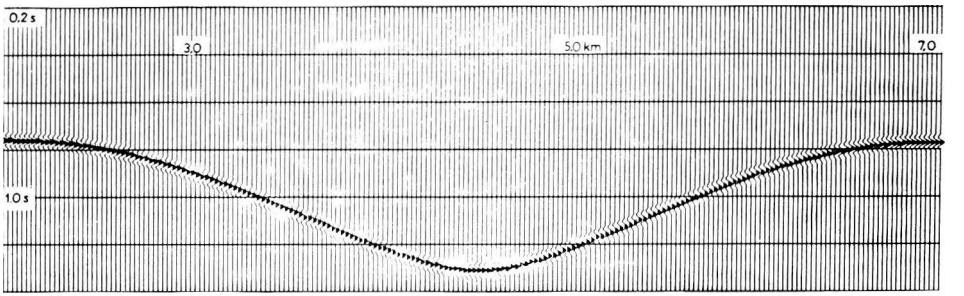

Fig. 9. Zero-offset time section for syncline-like boundary. Velocities: $V_1 = 2000$ m/s, $V_2 = 3000$ m/s; space and time steps: $\Delta x = 25$ m, $\Delta t = 0.004$ s

9. ábra. Szinklinális-szerű határfelület 0-eltolású időszelvénye. Tér- és idő mintavétel: $\Delta x = 25$ m, $\Delta t = 0.004$ s; sebességek: $V_1 = 2000$ m/s, $V_2 = 3000$ m/s

Рис. 9. Временной профиль синклиналеобразной поверхности раздела с нулевым смещением. Отсчеты пространства и времени: $\Delta x = 25$ м, $\Delta t = 0{,}004$ с, скорости $V_1 = 2000$ м/с и $V_2 = 3000$ м/с.

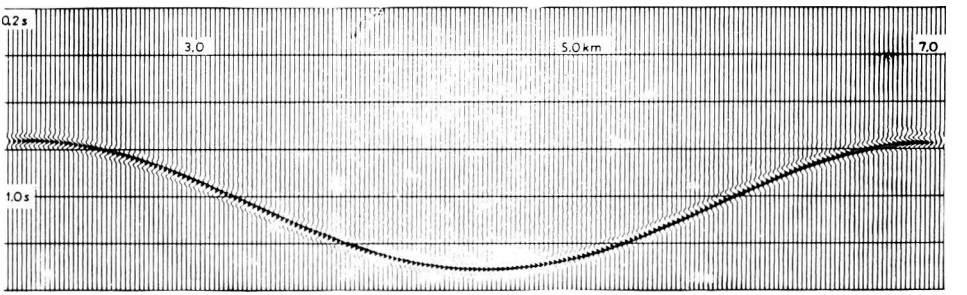

Fig. 10. Time section after migration with relation (19) for wavefield of Fig. 9. Time and space steps: $\Delta t = 0.004$ s, $\Delta z = 0.004$ s

10. ábra. A (19) egyenlettel számított migráció utáni időszelvény a 9. ábra hullámterére. Idő- és tér mintavétel: $\Delta t = 0{,}004$ s, $\Delta z = 0{,}004$ s

Рис. 10. Временной профиль волнового поля рис. 9 после миграции по уравнению (19). Отсчеты пространства и времени: $\Delta z = 0{,}004$ с, $\Delta t = 0{,}004$ с.

itself partially compensates that portion of the geometric spreading factor which accompanies wave propagation upward from the reflector in a direction normal to it. The differentiation of the wave field with respect to frequency compensates the remaining portion of the geometric spreading factor which accompanies the wave propagation from source to reflector along the line normal to it. This means the elimination of spherical divergence. Experiments carried out in media containing a single seismic horizon separating layers of different but constant velocity, proved that migration computed with the aid of Eq. (19) eliminates spherical divergence and provides information about the properties of the medium. If algorithm (19) is utilized for migration it enables one to trace the velocity changes in the underlying layer.

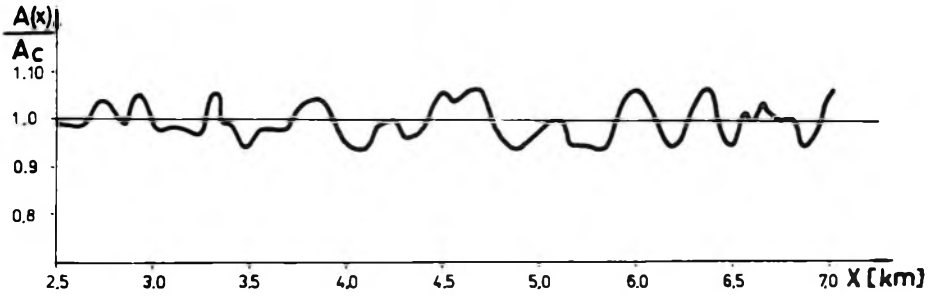

Fig. 11. Distribution of relative amplitudes $A(x)/A_c$ along the syncline-like boundary after migration with relation (19). A_c — denotes the amplitude in the centre of the syncline

11. ábra. Az $A(x)/A_c$ relatív amplitúdók eloszlása szinklinális-szerű határfelület mentén, a (19) egyenlettel számított migráció esetén. A_c — a szinklinális közepén mért amplitúdó

Рис. 11. Распределение относительных амплитуд $A(x)/A_c$ вдоль синклиналеобразной поверхности раздела при миграции по уравнению (19): A_c — амплитуда, измеренная в центре синклинали.

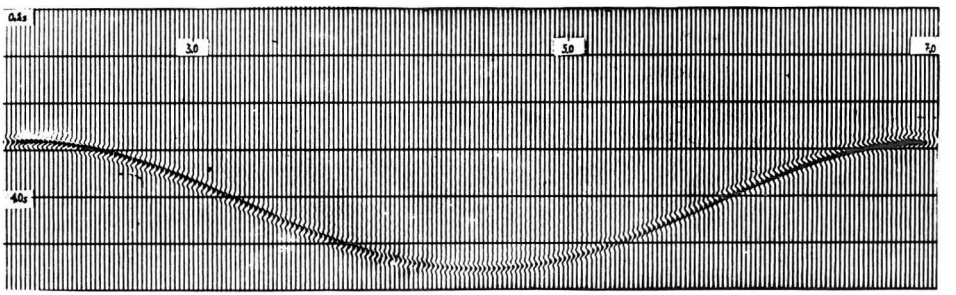

Fig. 12. Time section after conventional f–k migration for wavefield of Fig.9. Time and space steps: $\Delta t = 0.004$ s, $\Delta z = 0.004$ s

12. ábra. Hagyományos f–k migráció utáni időszelvény a 9. ábra hullámterére. Idő- és tér mintavétel: $\Delta t = 0{,}004$ s, $\Delta z = 0{,}004$ s

Рис. 12. Временной профиль волнового поля рис. 9 после традиционной f–k миграции. Отсчеты пространства и времени: $\Delta z = 0{,}004$ с, $\Delta t = 0{,}004$ с.

For the general case of heterogeneous media, approximations of the field extrapolation operator by means of the ray theory seem to be the most promising way for finding solutions to the problem [GOLDIN 1985], as well as being the most suitable tool for high frequency approximation of the seismic field. Such an approach has been also proposed by COHEN and HAGIN [1985] who tried to approximate Green's function in a heterogeneous medium. In the case of a two-dimensional medium with depth-dependent velocity the WKBJ solution can effectively be applied [CLAYTON and STOLT 1981, KOSTECKI 1984], that is done by modifying the integrand of $f-k$ migration algorithm and reducing it to a form which happens to be the analogue of the approximation of Green's function used in the ray tracing method.

Recently, STOLT and WEGLEIN [1985] undertook to estimate the possibility of accounting for density changes in a layered medium. All the mentioned ways of seismic field downward extrapolation attempt to compensate for the geometric spreading factor and thus gain information about the reflection coefficient or values proportional to the reflection coefficient along the reflector. In the case of a heterogeneous layered medium with flat reflectors the V_{rms} velocity and CMP travel time can be accepted as the first approximation—in other words, it is equivalent to applying the divergence proposed by NEWMAN [1973]. When presenting the so called "tuned reflector model" which accounts only for waves normal to the reflector, HUBRAL [1983] proposed a means of computing the geometric spreading factor for a heterogeneous medium based only on CMP traveltime. Because the geometric spreading factor does not change for waves normal to the reflector the practical application of that method (tuning the wave front to reflector morphology) seems to be a promising way to get information about the reflection coefficient in heterogeneous media.

Nonetheless the main purpose to be achieved (i.e. the invention of a reliable method for estimating the reflection coefficients) requires much more to be done. Concluding our considerations, we state the following:

1. The migration procedure (algorithm 16) in the wavenumber–frequency domain or migration expressed by Kirchhoff's integral (Eq. 17) (for homogeneous media only, i.e. for a single seismic boundary) enables one to trace the values proportional to the reflection coefficient because the spherical divergence has been eliminated from the whole bandwith (relation 18) except for zero frequency.
2. The application of high-frequency approximation (algorithm (19) or (17)) with no $\int_0^t F(x, y, 0, \tau)\, d\tau$ term is justified due to the negligible influence of the low frequency component.
3. The high-frequency approximation of migration which eliminates spherical divergence (relation 19) is equivalent to the high-frequency approximation of velocity inversion (relation 9), given by COHEN and BLEISTEIN [1979].
4. High-frequency approximation can be computed with the aid of conventional $f-k$ migration substituting the observed seismic field $F(x, y, 0, t)$ by product $tF(x, y, 0, t)$ or by applying Kirchhoff's integral neglecting the $\int_0^t F(x, y, 0, \tau)\, d\tau$ term (relation 17). By comparison with conventional migration the computational procedure is equally time consuming.

APPENDIX A

In order to find function $\alpha(x_0, y_0, z_0)$ we shall apply the Fourier transformation assuming that the wave field over the surface of recording is characterized by the full bandwidth. This approach has been accepted by several authors [COHEN, BLEISTEIN 1979, ALEKSEEV et al. 1981, KOSTECKI 1983, CHENG

and COEN 1984]. Taking it into account that the integrand in Eq. (1) is a two-dimensional convolution (with respect to x and y) i.e.

$$\alpha(x, y, z) * e^{-i2\omega R_0/V}/R_0$$

where

$$R_0 = (x^2 + y^2 + z_0^2)^{1/2}$$

we shall get the following:

$$\frac{\partial}{\partial\omega}\left\{\frac{F(x, y, 0, \omega)}{\omega^2}\right\} = \frac{-i}{8\pi^2 V^3}\int_{z_0}[\alpha(x, y, z_0) * e^{-i2\omega R_0/V}/R_0]\,dz_0 \qquad (A\ 1)$$

assuming the U region to be infinite in the x and y directions. Applying the two-dimensional Fourier transformation ($x \to k_x$, $y \to k_y$) to both sides of equation (A 1) and taking advantage of Weyl's distribution [BREKHOVSKICH 1957].

$$\int_{-\infty}^{+\infty}\int \frac{e^{\mp ikR_0}}{R_0} e^{-i(k_x x + k_y y)}\,dx\,dy = \mp 2\pi i \frac{e^{\mp ik_z z_0}}{k_z} \quad \text{for} \quad z_0 > 0 \qquad (A\ 2)$$

where

$$k_z = (k^2 - k_x^2 - k_y^2)^{1/2}$$

we shall get the equation:

$$\frac{\partial}{\partial\omega}\left\{\frac{F(k_x, k_y, 0, \omega)}{\omega^2}\right\} = -\frac{1}{4\pi V^3}\int_{z_0}\alpha(k_x, k_y, z_0)\frac{e^{-ik_z z_0}}{k_z}\,dz_0 \qquad (A\ 3)$$

where

$$\alpha(k_x, k_y, z_0) = \int_{-\infty}^{+\infty}\int \alpha(x, y, z_0) e^{-i(k_x x + k_y y)}\,dx\,dy$$

Applying the inverse Fourier transformation ($k_z \to z_0$) we shall get from (A 3)

$$\alpha(k_x, k_y, z_0) = -2V^3\int_{k_z} k_z \frac{\partial}{\partial\omega}\left\{\frac{F(k_x, k_y, 0, \omega)}{\omega^2}\right\} e^{ik_z z_0}\,dk_z \qquad (A\ 4)$$

Taking it into consideration that $k_z\,dk_z = k\,dk = \frac{4\omega}{V^2}\,d\omega$ the integration with respect to k_z can be replaced by integration with respect to ω. The application of two-dimensional Fourier transformation to Eq. (A 4) ($k_x \to x_0$, $k_y \to y_0$) yields:

$$\alpha(x_0, y_0, z_0) =$$

$$= -\frac{2V}{\pi^2} \int_{-\infty}^{+\infty}\int\int\int \omega \frac{\partial}{\partial\omega}\left\{\frac{F(k_x, k_y, 0, \omega)}{\omega^2}\right\} e^{ik_z z_0} e^{i(k_x x_0 + k_y y_0)}\, dk_x\, dk_y\, d\omega \tag{A 5}$$

where

$$k_z = \begin{cases} \operatorname{sgn}\omega\left(\dfrac{4\omega^2}{V^2} - k_x^2 - k_y^2\right)^{1/2} & \text{if} \quad \dfrac{4\omega^2}{V^2} > k_x^2 + k_y^2 \\ +i\left(k_x^2 + k_y^2 - \dfrac{4\omega^2}{V^2}\right)^{1/2} & \text{if} \quad k_x^2 + k_y^2 > \dfrac{4\omega^2}{V^2} \end{cases} \tag{A 6}$$

In practice we can limit our considerations to real values of k_z due to the rapid decrease of the evanescent field when depth z_0 increases [STOLT 1978, BERKHOUT 1980]. Let us express relation (A 5) in the form of Kirchhoff's integral. It is easy to note that the expression under the integral in (A 5) is a product of two-dimensional transforms and thus we can take advantage of Weyl's integral (A 2) and write:

$$\alpha(x_0, y_0, z_0) =$$

$$= \frac{i2V}{\pi^2} \frac{\partial}{\partial z_0} \int_{-\infty}^{+\infty}\int\int\int \omega \frac{\partial}{\partial\omega}\left\{\frac{F(k_x, k_y, 0, \omega)}{\omega^2}\right\} \frac{e^{ik_z z_0}}{k_z} e^{i(k_x x_0 + k_y y_0)}\, dk_x\, dk_y\, d\omega =$$

$$= \frac{4V}{\pi} \frac{\partial}{\partial z_0} \int_{-\infty}^{+\infty} \left(\omega \frac{\partial}{\partial\omega}\left\{\frac{F(x_0, y_0, 0, \omega)}{\omega^2}\right\} * \frac{e^{ikR_0}}{R_0}\right) d\omega = \tag{A 7}$$

$$= \frac{4V}{\pi} \frac{\partial}{\partial z_0} \int_{-\infty}^{+\infty}\int\int\int \omega \frac{\partial}{\partial\omega}\left\{\frac{F(x, y, 0, \omega)}{\omega^2}\right\} \frac{e^{ikR_s}}{R_s}\, dx\, dy\, d\omega$$

where

$$R_0 = (x_0^2 + y_0^2 + z_0^2)^{1/2}$$
$$R_s = [(x - x_0)^2 + (y - y_0)^2 + z_0^2]^{1/2}$$

Computation of Fourier transforms ($\omega \to t$) with respect to time t for both components of the integrand yields:

$$\frac{1}{2\pi} \int_{-\infty}^{+\infty} \frac{1}{\omega} \frac{\partial}{\partial\omega}\{F(x, y, 0, \omega)\} e^{i\omega t}\, d\omega = N(x, y, 0, t) \tag{A 8}$$

$$\frac{\partial}{\partial t} N(x, y, 0, t) = \frac{i}{2\pi} \int_{-\infty}^{+\infty} \frac{\partial}{\partial\omega}\{F(x, y, 0, \omega)\} e^{i\omega t}\, d\omega = tF(x, y, 0, t) \tag{A 9}$$

and, based upon (A 8) and (A 9), we have:

$$N(x, y, 0, t) = \int_0^t \tau F(x, y, 0, \tau)\, d\tau \tag{A 10}$$

where: τ = variable of integration.

Let the second component of the integrand be $S(x, y, 0, t)$ i.e.

$$-\frac{1}{2\pi} \int_{-\infty}^{+\infty} \frac{F(x, y, 0, \omega)}{\omega^2} e^{i\omega t}\, d\omega = S(x, y, 0, t) \tag{A 11}$$

and thus we have

$$\frac{\partial^2}{\partial t^2} S(x, y, 0, t) = F(x, y, 0, t) \tag{A 12}$$

When we express function $S(x, y, 0, t)$ as a double convolution with the Heaviside function involved, then we have:

$$\begin{aligned} S(x, y, 0, t) &= \int_0^t d\tau_1 \int_0^{\tau_1} F(x, y, 0, \tau_2)\, d\tau_2 = \\ &= \int_0^\infty H(t-\tau_1)\left[\int_0^\infty H(\tau_1-\tau_2) F(x, y, 0, \tau_2)\, d\tau_2\right] d\tau_1 = \\ &= F(x, y, 0, t) * H(t) * H(t) = F(x, y, 0, t) * tH(t) = \\ &= \int_0^\infty (t-\tau) H(t-\tau) F(x, y, 0, \tau)\, d\tau = \\ &= \int_0^t (t-\tau) F(x, y, 0, \tau)\, d\tau \end{aligned} \tag{A 13}$$

where τ, τ_1, τ_2 are the variables of integration. Relations (A 10) and (A 13) when inserted into Eq. (A 7) yield the expression for $\alpha(x_0, y_0, z_0)$ in the form of Kirchhoff's integral:

$$\alpha(x_0, y_0, z_0) = 8V \frac{\partial}{\partial z_0} \iint_{-\infty}^{+\infty} \left. \frac{2t \int_0^t F(x, y, 0, \tau)\, d\tau - \int_0^t \tau F(x, y, 0, \tau)\, d\tau}{R_s} \right|_{t=\frac{2R_s}{V}} dx\, dy \tag{A 14}$$

Following the procedure similar to that applied for function $\alpha(x_0, y_0, z_0)$ one can obtain the following expression for the $\beta(x_0, y_0, z_0)$ function

$$\beta(x_0, y_0, z_0) = \frac{i8}{\pi} \frac{\partial}{\partial z_0} \iiint_{-\infty}^{+\infty} \omega^2 \frac{\partial}{\partial \omega} \left\{ \frac{F(x, y, 0, \omega)}{\omega^2} \right\} \frac{e^{ikR_s}}{R_s}\, dx\, dy\, d\omega \tag{A 15}$$

Applying the Fourier transformation ($\omega \to t$)

$$\frac{1}{2\pi}\int_{-\infty}^{+\infty}\frac{1}{\omega}F(x, y, 0, \omega)e^{i\omega t}\,d\omega = i\int_{0}^{t}F(x, y, 0, \tau)\,d\tau \qquad \text{(A 16)}$$

and taking advantage of Eqs. (A 8) and (A 10) we obtain the desired relation for the $\beta(x_0, y_0, z_0)$ function:

$$\beta(x_0, y_0, z_0) = 16\frac{\partial}{\partial z_0}\iint_{-\infty}^{+\infty}\frac{2\int_0^t F(x, y, 0, \tau)\,d\tau + tF(x, y, 0, t)}{R_s}\Bigg|_{t=\frac{2R_s}{V}}dx\,dy \qquad \text{(A 17)}$$

APPENDIX B

In order to express the Fourier transform ($k_x \to x$, $k_y \to y$) of the integrand function $\omega^2\frac{\partial}{\partial\omega}\left\{\frac{F(k_x, k_y, 0, \omega)}{\omega^2}\right\}$ by function $\beta(x_0, y_0, z_0)$ we perform the mathematical operations in reverse order to the sequence of operations followed during the derivation of function $\alpha(x_0, y_0, z_0)$ i.e. from Eq. (A 5) to Eq. (A 1) operation. Eq. (6) is a starting point for this procedure.

Those operations done, we have:

$$\omega^2\frac{\partial}{\partial\omega}\left\{\frac{F(x, y, 0, \omega)}{\omega^2}\right\} = -\frac{2}{\omega}F(x, y, 0, \omega) + \frac{\partial}{\partial\omega}F(x, y, 0, \omega) = \qquad \text{(B 1)}$$

$$= \frac{-\omega}{16\pi^2V^2}\iiint_U \beta(x_0, y_0, z_0)\frac{e^{-i\frac{2\omega R_s}{V}}}{R_s}\,dx_0\,dy_0\,dz_0$$

and thus for high frequency the following holds true:

$$\frac{\partial}{\partial\omega}F(x, y, 0, \omega) \cong \frac{-\omega}{16\pi^2V^2}\iiint_U \beta(x_0, y_0, z_0)\frac{e^{-i\frac{2\omega R_s}{V}}}{R_s}\,dx_0\,dy_0\,dz_0 = \qquad \text{(B 2)}$$

$$= \frac{-i}{32\pi^2V}\iiint_U \beta(x_0, y_0, z_0)\frac{1}{R_s}\frac{\partial}{\partial R_s}\left(e^{-i\frac{2\omega R_s}{V}}\right)dx_0\,dy_0\,dz_0$$

The relation between the $F(x, y, 0, \omega)$ field recorded over the $z=0$ surface and function $\beta(x_0, y_0, z_0)$ which simulates the effective source distribution can be obtained directly from (B 2).

$$F(x, y, 0, \omega) \cong \frac{1}{64\pi^2} \iiint_U \beta(x_0, y_0, z_0) \frac{1}{R_s} \frac{\partial}{\partial R_s} \left(\frac{e^{-i\frac{2\omega R_s}{V}}}{R_s} \right) dx_0\, dy_0\, dz_0 =$$

$$= -\frac{1}{64\pi^2} \iiint_U \beta(x_0, y_0, z_0) \left(\frac{1}{R_s^2} + \frac{ik}{R_s} \right) \frac{e^{-ikR_s}}{R_s} dx_0\, dy_0\, dz_0 \tag{B 3}$$

Comparing relation (B 3) and Eq. (12) we can provide the approximative relation between the migrated values of field $F(x_0, y_0, z_0)$ and source distribution $\beta(x_0, y_0, z_0)$:

$$aF(x_0, y_0, z_0) \cong -(\beta(x_0, y_0, z_0) \left(\frac{1}{R_s} + \frac{1}{ikR_s^2} \right) \tag{B 4}$$

where

$$a = \frac{64\pi}{V}.$$

Following the procedure similar to that used for the derivation of (B 1) we can obtain the following relation between Fourier transform ($k_x \to x$, $k_y \to y$) of integrand $\omega \frac{\partial}{\partial \omega} \left\{ F(k_x, k_y, 0, \omega) \right\}$ (Eq. 16) and migrated field $P(x_0, y_0, z_0)$:

$$\omega \frac{\partial}{\partial \omega} \left\{ \frac{F(x, y, 0, \omega)}{\omega} \right\} = \frac{4\omega}{\pi V^3} \iiint_U P(x_0, y_0, z_0) \frac{e^{-i\frac{2\omega R_s}{V}}}{R_s} dx_0\, dy_0\, dz_0 \tag{B 5}$$

and thus the recorded field $F(x, y, 0, \omega)$ can be expressed by

$$F(x, y, 0, \omega) = \frac{i2\omega}{\pi V^2} \iiint_U P(x_0, y_0, z_0) \frac{e^{-i\frac{2\omega R_s}{V}}}{R_s^2} dx_0\, dy_0\, dz_0 \tag{B 6}$$

By comparing relation (B 6) with the expression for the conventionally migrated field (i.e. relation 12) we can obtain the formulae relating the migrations $P(x_0, y_0, z_0)$ and $F(x_0, y_0, z_0)$:

$$P(x_0, y_0, z_0) = R_s F(x_0, y_0, z_0) \tag{B 7}$$

Relation (B 7) bears evidence of the complete elimination of spherical divergence.

REFERENCES

ALEKSEEV A. S., KREMLEV A. N., ZHERNJAK G. F. 1981: On the inverse problem of acoustic wave diffraction and visualization method and wave migration (in Russian). Geologiya i Geofizika 1, pp. 111–118

BERKHOUT A. J. 1980: Seismic Migration, Elsevier (Scientific Publishing Company)
BERKHOUT A. J. 1984: Multidimensional linearized inversion and seismic migration. Geophysics **49**, 11, pp. 1881–1895
BLEISTEIN N. and COHEN J. K. 1982: Velocity inversion — Present status, new directions. Geophysics **47**, 11, pp. 1497–1511
BLEISTEIN N., COHEN J. K., HAGIN F. G. 1985: Computational and asymptotic aspects of velocity inversion. Geophysics **50**,8, pp. 1253–1265
BREKHOVSKICH L. M. 1957: Waves in layered media (in Russian). Academy of Sciences of the USSR, pp. 214–217
CHENG G. and COEN S. 1984: The relationship between Born inversion and migration for common-midpoint stacked data. Geophysics **49**,12, pp. 2117–2131
CLAERBOUT J. F. 1970: Coarse grid calculations of waves in inhomogeneous media with application to delineation of complicated seismic structure. Geophysics **35**,3, pp. 407–418
CLAERBOUT J. F., DOHERTY S. M. 1972: Downward continuation of moveout corrected seismograms. Geophysics **37**,5, pp. 741–768
CLAYTON R. W., STOLT R. H. 1981: A Born–WKBJ inversion method for acoustic reflection data. Geophysics **46**,11, pp. 1559–1567
COHEN J. K., BLEISTEIN N. 1979: Velocity inversion procedure for acoustic waves. Geophysics **44**,6, pp. 1077–1087
COHEN J. K., HAGIN F. G. 1985: Velocity inversion using a stratified reference. Geophysics **50**,11, pp. 1689–1700
GAZDAG J. 1980: Wave equation migration with the accurate space derivative method. Geophysical Prospecting **28**,1, pp. 60–70
GOLDIN S. W. 1985: Integral continuation of wave fields (in Russian). Geologiya i Geofizika **4**, pp. 103–112, Publishing House Nauka
HUBRAL P. 1983: Computing true amplitude reflections in a laterally inhomogeneous earth. Geophysics **48**,8, pp. 1051–1062
KOSTECKI A. 1983: Solution of the inverse problem in a wave equation. Determination of source density functions in two- and three-dimensional cases. Acta Geophysica Polonica **31**,2, pp. 161–168
KOSTECKI A. 1984: Seismic field extension into a medium with vertical velocity gradient. Acta Geophysica Polonica **32**,1, pp. 43–49
KOSTECKI A. 1986: Defining velocity changes as a solution of the inverse problem in wave equation. Acta Geophysica Polonica **34**,1, pp. 41–48
LOEWENTHAL D., LU L., ROBERTSON R., SHERWOOD J. 1976: The wave equation applied to migration. Geophysical Prospecting **24**,2, pp. 380–399
MORSE P. M., FESHBACH H. 1953: Methods of Theoretical Physics, Part 1, 747. p., Mc Graw Hill Book Company
NEWMAN P. 1973: Divergence effects in a layered earth. Geophysics **38**,3, pp. 481–488
RAZ S. 1981: Three-dimensional velocity profile inversion from finite-offset scattering data. Geophysics **46**,6, pp. 837–842
RAZ S. 1982: A procedure for multidimensional inversion of seismic data. Geophysics **47**,10, pp. 1422–1430
SCHNEIDER W. A. 1978: Integral formulation for migration in two and three dimensions. Geophysics **43**,1, pp. 49–76
STOLT R. H. 1978: Migration by Fourier transform. Geophysics **43**,1, pp. 23–48
STOLT R. H., WEGLEIN A. B. 1985: Migration and inversion of seismic data. Geophysics **50**,12, pp. 2458–2472
TARANTOLA A. 1984: Linearized inversion of seismic reflection data. Geophysical Prospecting **32**,6, pp. 998–1015
TSIBUL'CHIK G. M. 1981: About the solution of some inverse problems for wave equation by the visualizing of sources method (in Russian). Geologiya i Geofizika 2, pp. 109–119

SZEIZMIKUS MIGRÁCIÓ A SZFÉRIKUS DIVERGENCIA KIKÜSZÖBÖLÉSÉVEL

Andrzej KOSTECKI

A tanulmány bemutatja a hagyományos migráció és a Born inverzió kapcsolatát. Ez utóbbi a különböző sebességű közegeket elválasztó határfelületre merőleges irányú sebességinverzió. Új migrációs algoritmust javasol nulla eltolású szeizmikus szelvényekre, a szférikus divergencia kiküszöbölésével a teljes frekvenciasávon. A javasolt algoritmus nagyfrekvenciás közelítése egy konstanstól eltekintve a Cohen–Bleistein algoritmushoz konvergál, függetlenül attól, hogy ez utóbbit Kirchhoff migrációhoz vagy *f–k* migrációhoz alkalmazzuk. A nagyfrekvenciás közelítések tulajdonságait a szintetikus hullámtér 2D és 3D modelljeire végzett számításokkal mutatja be.

СЕЙСМИЧЕСКАЯ МИГРАЦИЯ С УСТРАНЕНИЕМ СФЕРИЧЕСКОЙ ДИВЕРГЕНЦИИ

Анджей КОСТЕЦКИ

Демонстрируется связь традиционной миграции с инверсией Борна, представляюшей собой инверсию скоростей перпендикулярно к поверхности раздела между средами с различными скоростями. Предлагается новый алгоритм миграции для сейсмических профилей с нулевым сдвигом, с устранением сферической дивергенции в полном диапазоне частот. Высокочастотное приближение предлагаемого алгоритма сходится с алгоритмом Когена–Блейштейна за исключением одной из констант, независимо от того, применяется ли он к кирхгофовской миграции или же к *f–k* миграции. Свойства высокочастотных приближений демонстрируются расчетами, выполненными для моделей 2D и 3D синтетического волнового поля.

GEOPHYSICAL TRANSACTIONS 1988
Vol. 33. No. 3–4. pp. 211–220

NEW VARIANT OF INTERVAL VELOCITY ESTIMATION FROM REFLECTION AMPLITUDES

Volker KRUG*

Instead of using single traces as is done with the common pseudo-acoustic log, amplitude variations across adjoining traces along reflective horizons are used in the presented method. Proceeding from a reference trace, the reflectivity-dependent relative velocity changes, which are proportional to the amplitude variations, are determined. Since all amplitude values of a signal are suitable for calculation, signal compression (spike deconvolution) is not necessary. The examples of two profiles demonstrate the achievable results when using the horizontal changes of layer velocities.

Keywords: reflection methods, velocity, amplitude, seislog, signal-to-noise ratio, pseudo-acoustic log

1. Introduction

In recent years, the pseudo-acoustic velocity log has become important for the interpretation of local velocity variations. In particular, it has been utilized for detecting lithological changes within the limits of oil or gas deposits. The pseudo-velocity log in the classical meaning implements the velocity determination sample-wise along the time axis for one trace [LINDSETH 1979, GOGONENKOV et al. 1980]. By that procedure the value of the true amplitude is assigned to the seismic impedance at the respective location thus enabling us to determine the velocity distribution along the seismic trace. Strictly speaking, such a treatment assumes a pulse trace (not to speak about other problems; see below). Similar to a procedure used by BOISSE [1978], an alternative program has been developed which does not consider the amplitude variation along a single trace but across adjoining traces along the direction of correlation of horizons. In contrast to Boisse's procedure not only the main phase (or amplitudes) of the signals of selected horizons is processed for calculation of underlying interval velocities but all samples (sample-wise) between two consecutive horizons. Such an approach provides a more favourable statistical interpretation, especially of horizontal velocity variations.

* VEB Kombinat Geophysik Leipzig, Bautzner Strasse 67, GDR–7024
Paper presented at the 31st International Geophysical Symposium, Gdansk, 30 September–3 October, 1986

2. Principle of procedure

Fig. 1 shows the principle of the algorithm which is used in this paper. A presupposition of the treatment is a reference trace (a) recorded near the well. This trace can be obtained by the averaging of several adjoining traces. To this reference trace belongs a corresponding velocity model (V_{a1}, V_{a2}) or reflectivity sequence which is derived from sonic logs of nearby boreholes. The reflection coefficient is

$$R_a = kA_a \approx \frac{V_{a1} - V_{a2}}{V_{a1} + V_{a2}} \tag{1}$$

if the density contrast is neglected ($\varrho_1 \approx \varrho_2$). k is a scale factor, A_a the sample amplitude at time T for the reference trace. For a neighbour trace (b) the correspondig reflectivity at the same time (better: at the same horizon or phase position) may be expressed by the velocities V_{b1} and V_{b2}. The corresponding reflection coefficient on trace b is

$$R_b = kA_b \approx \frac{V_{b1} - V_{b2}}{V_{b1} + V_{b2}} \tag{2}$$

From the amplitude ratio between reference trace and adjoining trace

$$\frac{R_a}{R_b} = \frac{A_a}{A_b} \approx \frac{(V_{a1} - V_{a2})(V_{b1} + V_{b2})}{(V_{a1} + V_{a2})(V_{b1} - V_{b2})} \tag{3}$$

the velocity V_{b2}, etc. may be determined, provided the velocity V_{b1} is known:

$$V_{b2} \approx \frac{A_a V_{b1}(V_{a1} + V_{a2}) - A_b V_{b1}(V_{a1} - V_{a2})}{A_a(V_{a1} + V_{a2}) + A_b(V_{a1} - V_{a2})} \tag{4}$$

For V_{b1} one can use either the mean velocity derived from the aforetreated layer or from the given velocity model. This will be done for all traces of a stacked time section with true amplitudes.

The position of the reflecting horizons along the x-axis (T_1 in Fig. 1, and see correlation in Figs. 3 and 5) in the time section is visually picked and the intermediate layer velocities are linearly interpolated.

The trace processing sample by sample between two consecutive horizons is done parallel to the upper horizon. Since some problems may arise with thickness variations, the selection of the reference trace is of particular importance. It should preferably be taken from that point where the thickness is greatest.

For calculation, such amplitude values are abandoned which are less than a preselected percentage of the mean value of the trace. Obtained velocity values which surpass or underflow a given level are not further used for treatment. The frequently very scattered individual values on the traces are subjected to a selectable (in x and t), two-dimensional and position-weighted smoothing. As

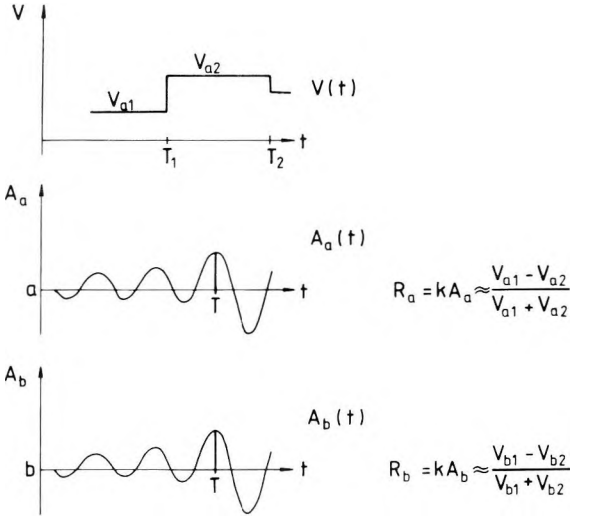

$$\frac{R_a}{R_b} = \frac{A_a}{A_b} \approx \frac{(V_{a1} - V_{a2})(V_{b1} + V_{b2})}{(V_{a1} + V_{a2})(V_{b1} - V_{b2})} \qquad V_{b2} \approx \frac{A_a V_{b1}(V_{a1} + V_{a2}) - A_b V_{b1}(V_{a1} - V_{a2})}{A_a(V_{a1} + V_{a2}) + A_b(V_{a1} - V_{a2})}$$

Fig. 1. Scheme of velocity estimation

1. ábra. A sebességbecslés vázlata

Рис. 1. Схема определения скоростей.

result we obtain interval contour plots which represent either the interval velocities or the deviation of the interval velocity from the reference trace (ΔV) or its percentual variation. This approach has some advantages over the commonly used pseudo-velocity log:

Advantages

- no spike deconvolution necessary (input is not considered as pulse seismogram but as wavelet)
- no complete frequency band required
- better use of a priori knowledge
- variable smoothing of data
- statistical procedure, robust calculation regime
- no accumulation of errors with time
- better elimination of interference
- application possible also at worse S/N-ratio

Disadvantages

- assumption of horizons with accurate correlation
- problems arising with the sampling if layer thickness changes
- no elimination of distortion (e.g. dispersion)

3. Examples

The next figures demonstrate the calculation results from two profiles *A* and *B* extending parallelly to a distance of 400 m. *Fig. 2* shows for profile *A* the normal stack, the stack with true amplitudes and the isoarea section of ΔV-results (related to reference trace at coordinate 3712 m) for the time interval essential for oil prospecting. The lowest (negative) ΔV values are white, the highest values are black. In *Fig. 3* the time scale was a little extended, the stacked traces (true amplitudes) are shown as wiggle traces and the velocity changes are plotted as ΔV contour lines. In *Fig. 4* an enlarged section is represented where stacked traces in wiggle trace form have been superimposed on the ΔV contour line section and an isoarea section is also presented. Similar plots for section *B* are presented in *Figs. 5* and *6*.

Both seismic profiles cross a carbonate sand barrier of the Zechstein (approximately between the coordinates 3000 m and 5500 m). The velocity estimation has been accomplished within the total Zechstein sequence. The main horizons are correlated in Fig. 3 and Fig. 5. The quality of the time section is poor but, nevertheless, usable results have been obtained. It is obvious that the velocity variations along the reflectors behave like the intensity of the true amplitudes, as expected. The differentiation is clearly greater for profile *B*, especially in the interesting x-interval (4000 m–5000 m). This indicates that the velocity contrasts at profile *A* are presumably lower than at profile *B*. On profile *A* it can be seen that the zone of reduced velocity around coordinate 5400 m extends with a decreasing trend to about 3100 m.

From $x = 5400$ m to higher x values one can see growing variations of the layer velocities which are connected with the steeper descent towards the trough caused by the barrier.

4. Conclusions

The quality or reliability of velocity estimations depends strongly on the quality of field data (i.e. on the signal-to-noise ratio). The statistical treatment of numerous velocity data permits a good estimation of relative velocity changes even for poor quality seismic sections. An accuracy of ± 100 m/s to ± 500 m/s should be expected for distances of about 1000 m from the borehole.

The procedure described here has the advantage of being able to use all amplitude values and spike deconvolution is not needed; on the other hand the exact correlation of horizons is something of a disadvantage.

If we are concerned with reliability, comprehensive model knowledge, and precise treatment of the original data, then this technique seems to be suitable for the exploration of large structures as well as for detailed investigations.

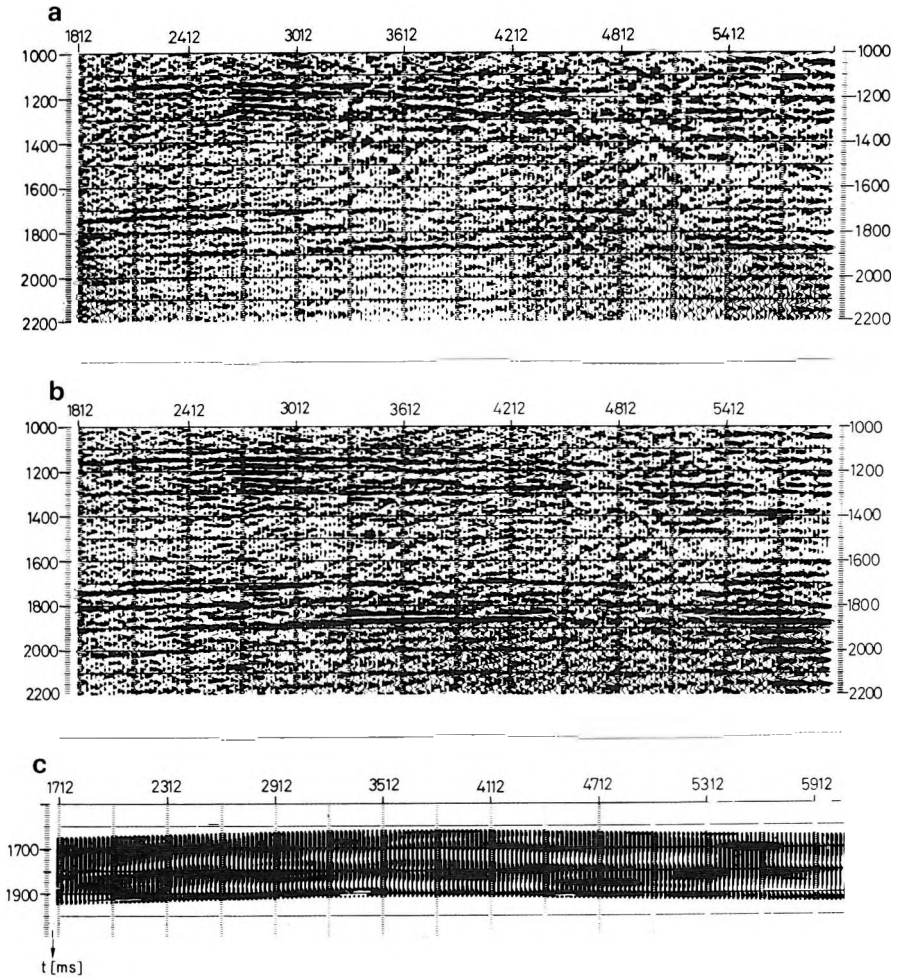

Fig. 2. Time section *A* for velocity estimation. a) Stacking; b) Stacking with true amplitudes; c) Calculated ΔV iso-area section. Velocity range: +400 m/s — −400 m/s in 200 m/s steps from dark to light

2. ábra. A sebességbecslésre felhasznált *A* időszelvény. a) Összegszelvény; b) Összegszelvény valódi amplitúdókkal; c) Számított ΔV szelvény. Sebességtartomány: +400 m/s — −400 m/s, 200 m/s lépésekkel, a sötéttől a világos árnyalatok felé haladva

Рис. 2. Временной разрез *A* для определения скоростей. a) Стекинг. b) Стекинг с истинными амплитудам. c) Рассчитанный профиль изоареалов ΔV. Диапазон скоростей от +400 м/с до −400 м/с через 200 м/с, от темных оттенков к светлым.

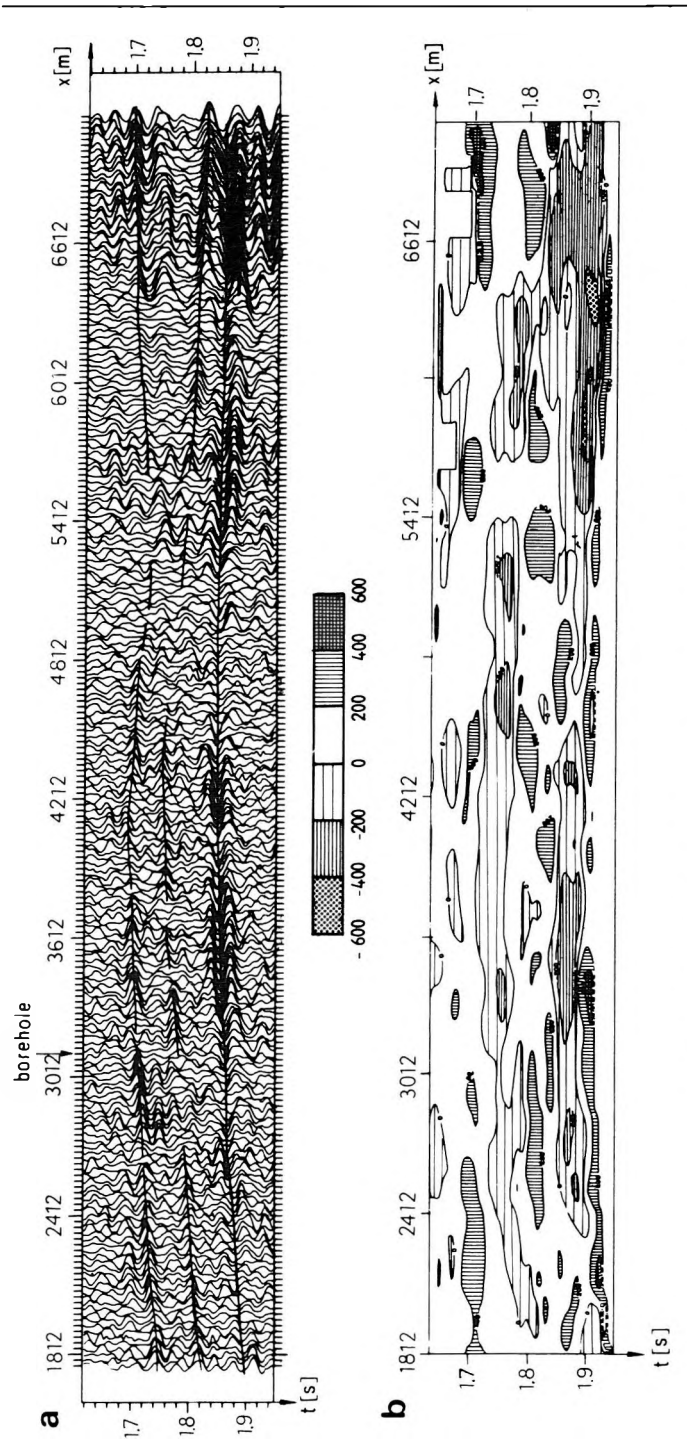

Fig. 3. Time section and estimated relative velocity changes (section *A*). a) True amplitudes (with correlation); b) ΔV isolines in m/s

3. ábra. Időszelvény és becsült relatív sebességváltozások (*A* szelvény) a) Valódi amplitúdók (korrelációval); b) ΔV izovonalak

Рис. 3. Временной разрез и определяемые относительные изменения скоростей (разрез *A*). а) Истинные амплитуды (скоррелированные). b) Изолинии ΔV в м/с.

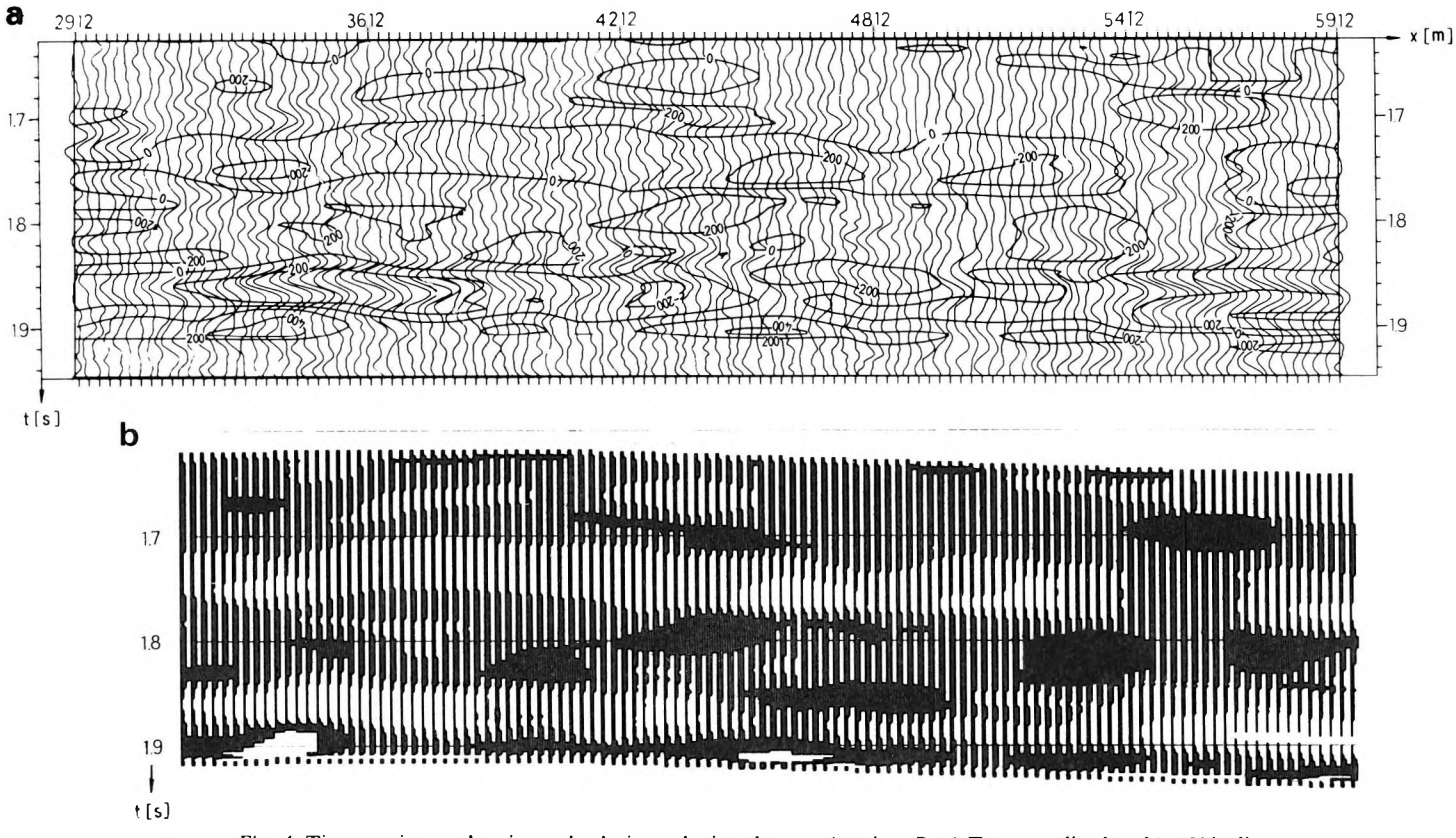

Fig. 4. Time section and estimated relative velocity changes (section *B*) a) True amplitudes: b) ΔV isolines

4. ábra. Időszelvény és becsült relatív sebességváltozások (*B* szelvény) a) Valódi amplitúdók; b) ΔV izovonalak

Рис. 4. Временной разрез и определяемые относительные изменения скоростей (разрез *B*). а) Истинные амплитуды. b) изолинии ΔV.

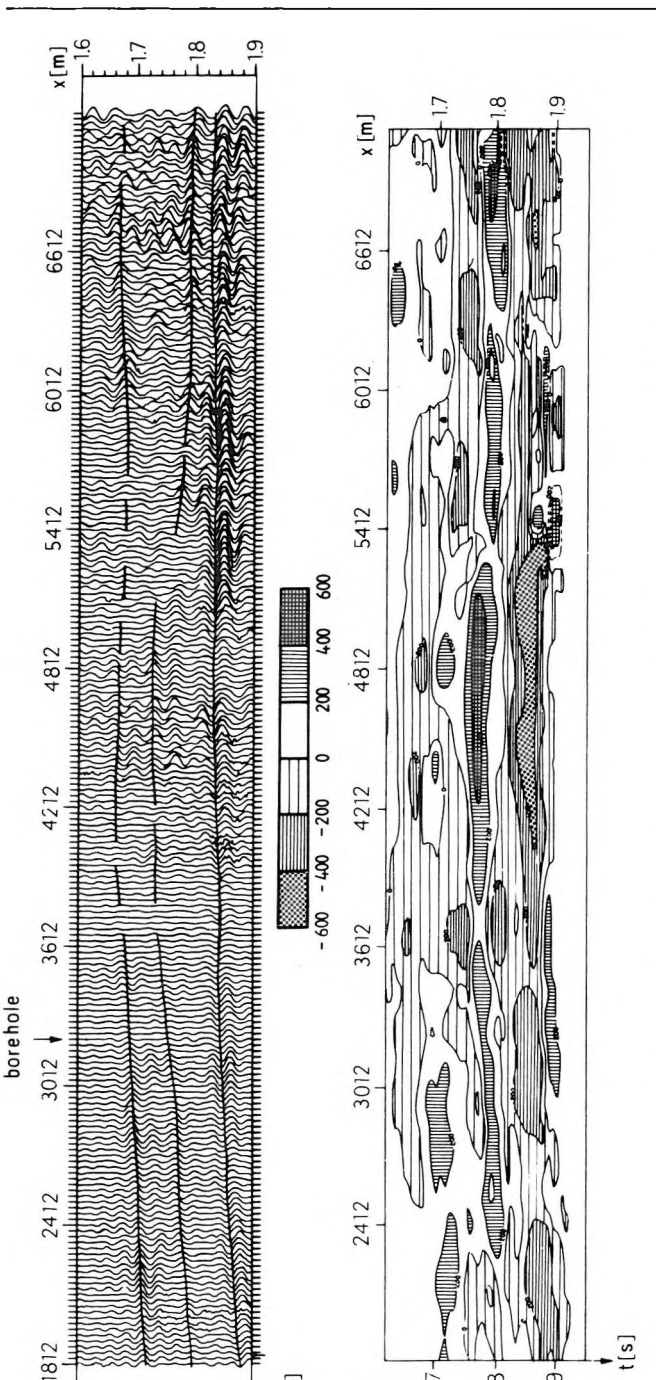

Fig. 5. Time section and estimated relative velocity changes (segment of section *A* a) ΔV-isolines and true amplitude traces; b) ΔV isoarea section. For scale see Fig.2.

5. ábra. Időszelvény és becsült relatív sebességváltozások (az *A* szelvény részlete) a) ΔV izovonalak és valódi amplitúdó csatornák; b) ΔV szelvény. A sebességskálát lásd az 1. ábrán

Рис. 5. Временной разрез и определяемые относительные изменения скоростей (фрагмент разреза *A*). а) Изолинии ΔV и каналы истинных амплитуд. b) Профиль ΔV. Шкалу скоростей см. на рис. 1.

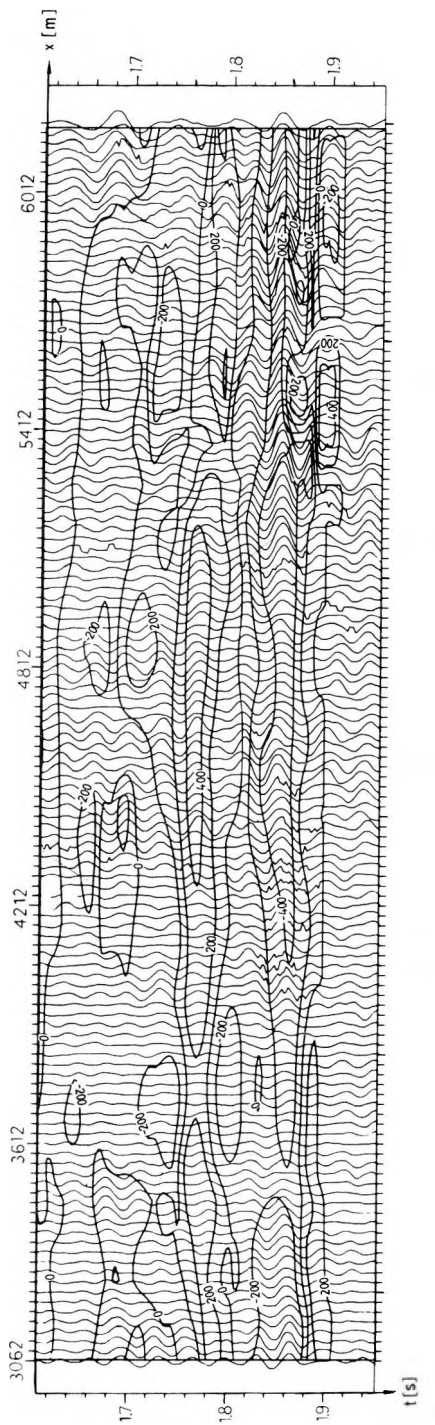

Fig. 6. Relative velocity changes along section *B* (enlarged segment)

6. ábra. Relatív sebességeloszlások a *B* szelvény mentén (részlet)

Рис. 6. Распределения относительных скоростей вдоль профиля *B* (фрагмент).

REFERENCES

Boisse S. 1978: Calculation of velocity from seismic reflection amplitude. Geophysical Prospecting **26**, 1, pp. 163–174

Gogonenkov G. N., Zacharov E. T., Elmanovich S. S. 1980: Determination of detailed velocity structure from seismic data (in Russian). Prikl. Geofiz. **97**, pp. 58–72

Lindseth R. O. 1979: Synthetic sonic logs — a process for stratigraphic interpretation. Geophysics **44**, 1, pp. 3–26

A REFLEXIÓS AMPLITÚDÓK ALAPJÁN VÉGZETT INTERVALLUMSEBESSÉG-BECSLÉS ÚJ MÓDSZERE

Volker KRUG

A tanulmány bemutat egy módszert, amelyben nem egyedi csatornákat dolgoz fel, mint ahogy a pszeudo-akusztikus karotázs szelvénynél szokásos, hanem reflektáló határfelületek mentén vizsgálja a szomszédos csatornák amplitúdó változásait. Egy referencia csatornából kiindulva a reflektivitástól függő, amplitúdó változásokkal arányos, relatív sebesség változásokat határoz meg. Mivel a jel bármely amplitúdó értéke alkalmas a számításokra, nincs szükség spike dekonvolúcióra. A bemutatott két szelvény vízszintes rétegsebesség-változások esetén mutatja az elérhető eredményeket.

НОВЫЙ МЕТОД ОЦЕНКИ ПОИНТЕРВАЛЬНЫХ СКОРОСТЕЙ НА ОСНОВАНИИ АМПЛИТУД ОТРАЖЕНИЙ

Фолькер КРУГ

Охарактеризован новый метод, в котором обрабатываются не одиночные каналы, как это принято в случае кривых псевдоакустического каротажа, а изучаются изменения амплитуд по соседним каналам вдоль отражающих поверхностей. Определяются относительные изменения скоростей, пропорциональные изменениям амплитуд и зависящие от отражательной способности, отнесенные к одному из каналов, выбранного в качестве опорного. Поскольку в расчетах могут быть использованы любые значения амплитуд сигналов, отпадает необходимость в спайк-деконволюции. Представляются два разреза в качестве иллюстрации результатов, полученных при горизонтальных изменениях погоризонтных скоростей.

GEOPHYSICAL TRANSACTIONS 1988
Vol. 33. No. 3–4. pp. 221–236

POSSIBILITIES AND LIMITATIONS OF RECOMPRESSIVE FILTERING IN THE PROCESSING OF SEAM-WAVE SEISMIC SURVEYS

György BAKI*, Tamás BODOKY*, Eszter CZILLER*, Péter SCHOLTZ*

The method for contracting dispersive signals, i.e. eliminating dispersion, is studied. Consideration is also given to the sensitivity of the method to the errors of input parameters, to noise, and to the distortions of the spectrum caused by absorption; further to what extent it is able to resolve the superposed dispersive signals. The processing of an in-seam seismic survey is presented to illustrate a practical application.

Keywords: reflection methods, mines, coal seams, dispersive filters, channel waves, in-mine seismics, recompressive filtering

1. Introduction

The in-seam seismic reflection technique — similarly to any other geophysical exploration technique — may be divided into three phases: data acquisition (i.e. the field measurement itself), data processing, and interpretation. A special step of the processing of in-seam seismic data, viz. recompressive filtering — which eliminates the dispersive character of the seam-waves — is treated here.

In order to understand the significance of this operation it must be known that there is a very important difference between seam waves and seismic waves employed in normal seismic surveys: this difference being the dispersive character of seam waves. Thus, data processing systems designed to treat impulse-like seismic signals are not able to process directly the data of in-mine seismic surveys before applying some operation to eliminate the dispersive character of seam waves. Two possible solutions of the problem are known [BODOKY et al. 1986]. The first one is the "German" way which uses a narrow band-pass filter to enhance the high frequencies of the Airy-phase and then applies enveloping [KLINGE et al. 1979]. The second one, the "English" way, employs recompressive filtering [BUCHANAN 1979].

* Eötvös Loránd Geophysical Institute of Hungary, POB 35, Budapest, H–1440
Manuscript received: 17 November, 1987

2. Recompressive filtering

The principle of recompressive filtering was published by BOOER et al. in 1977. Their method may be summarized as follows:

— the image of an impulse-like signal in the frequency–wavenumber domain is a straight line crossing the origin, that is

$$f(k) = ck$$

where f denotes frequency, k the wavenumber, and c — which is the slope of the line — the phase velocity. Here c has a constant value, which expresses that all frequency components propagate with the same phase velocity,

— the image of dispersive signals in the same domain is a curve — not a straight line — crossing the origin and increasing monotonously. Its equation is

$$f(k) = c(k)k$$

In this case the phase velocity is not a constant, it is a known function of wavenumber,

— the wavenumber spectrum of a seismic signal can be derived from its frequency spectrum with the help of the previous formulae. If the complex Fourier transform of an $s(t)$ seismic signal is $F\{s(t)\} = S(f)$ then this can be transformed by substituting the above functions:

$$S(f) = S\{f(k)\} = S(ck) = S'(k)$$

or

$$S(f) = S\{f(k)\} = S\{c(k)k\} = S'(k).$$

In the first case the shapes of the two spectra are the same only the scaling of the abscissa axes differs by a constant c factor. In the second case the shape of the spectrum also changes during transformation from $S(f)$ to $S'(k)$.

Thus, knowing the $c(k)$ dispersion curve of a seismic signal it is possible to change over from its frequency spectrum to its wavenumber one. Applying the above transform in the reverse way it is possible to return to the frequency spectrum by any arbitrary constant c (let us call it return velocity) and this spectrum will be the one of an impulse-like seismic signal propagating by return velocity c. (This signal will obviously arrive at the time corresponding to propagation velocity c.)

Of course, when applying this operation in practice one starts with a signal in the time domain and one wants to have the same form at the end. Thus, the operation begins with a direct Fourier transform and ends with an inverse one. A practical difficulty is that after transformation the sampling of the wavenumber spectrum is not equidistant, therefore a resampling is needed at that stage. The method should be applied after the separation of the modes because it is able to contract only one mode at a time.

A solution in the time domain is also known [see MARSCHALL and SCHOTT 1981]. The solution for the frequency domain was considered by GRUSZCZYK and SZABELSKI [1981].

3. Efficiency of recompressive filtering

In order to demonstrate and study the method a synthetic seismogram was computed for a symmetrical three-layer model where the density of rock enclosing the coal seam (ϱ_r) was 2500 kg/m^3, the velocity of shear waves in the rock (β_r) was 2000 m/s; while the same parameters of a 2 m thick coal seam were ϱ_c = 1500 kg/m^3 and β_c = 1000 m/s. Geophone spacing was 5 m in the direction of wave propagation *(Fig. 1)*.

In order to eliminate the dispersion of the seismogram it was filtered by the above-described recompressive filter at two different return velocities. *Figure 2* presents the result of filtering performed at a return velocity corresponding to the velocity of coal. The filter worked perfectly in the case of the synthetic seismogram, as can be seen in the figure. The long dispersed signals have been contracted into spike-like impulses in every case. However, it must not be forgotten that this form of recompressive filtering is based on deterministic principles since the dispersion curve of the waveguide, i.e. the coal seam, is previously given as a parameter of the filter. The dispersion curve depends on the following five parameters even in the most simple, symmetrical, three-layer case:

— propagation velocities of shear waves in the surrounding rocks and in the coal seam
— density of rocks and of coal
— thickness of the seam.

Therefore, it seemed necessary to examine the sensitivity of recompressive filtering to the errors of the input parameters.

A signal corresponding to 125 m source–receiver distance was computed with the parameters of Fig. 1 for the purpose of the examination. This signal was filtered, or in other words it was recompressed by erroneous parameters. *Fig. 3* presents the results of repeated filtering in which the shear-wave velocity for rock had a relative error that was changed between −25% and +25% in twenty steps. Similar results can be seen in *Fig. 4*, but in this case the shear-wave velocity for coal had the same error. It appears that the error of the velocity of rock (which determines the low-frequency end of the dispersion curve) — adversely influences the low-frequency part of the signal, whereas the error of the velocity of coal (which determines the high-frequency end of the dispersion curve) — adversely influences the high-frequency part of the signal. It was found in both cases that recompression was very sensitive to the accuracy of the examined parameters and even when they showed an error of only a few per cent the resulting length of signal could be several times longer than that of a signal obtained by exact parameters. The increased length of a signal leads to a blurring of its energy and a proportional reduction of its amplitude.

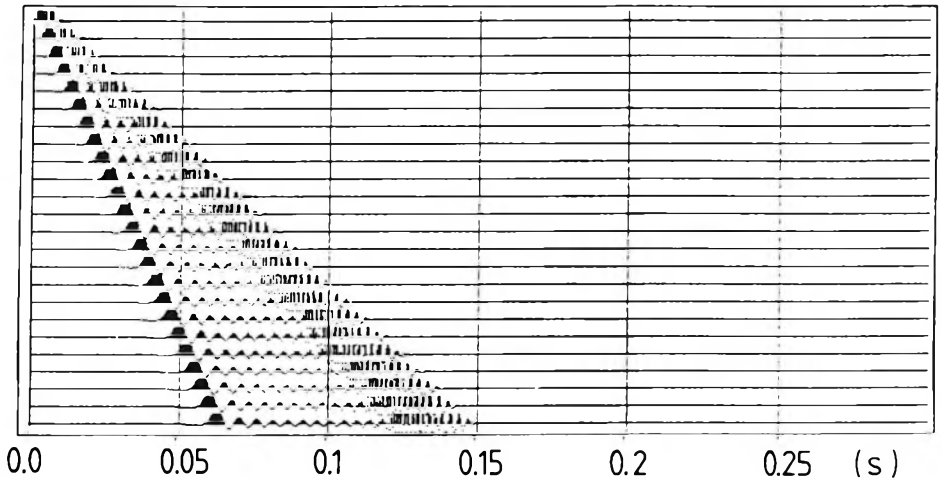

Fig. 1. Synthetic seismogram computed for a symmetrical three-layer model of a coal seam. Parameters: shear wave velocities for rock (β_r) and coal (β_c) 2000 and 1000 m/s, densities 2500 and 1500 kg/m^3, respectively; thickness of seam 2 m; geophone separation 5 m

1. ábra. Szimmetrikus telep modellre számított szintetikus szeizmogram. Paraméterek: az *S*-hullám sebessége a kőzetben (β_r) illetve a szénben (β_c) 2000, illetve 1000 m/s, a megfelelő sűrűség értékek 2500, illetve 1500 kg/m^3, a telep vastagsága 2 m; geofonköz 5 m

Рис. 1. Синтетическая сейсмограмма, рассчитанная для симметричной залежи со следующими параметрами: скорости во вмещающих породах (β_r) и углях (β_c) составляют 2000 и 1000 м/с, их плотности — 2500 и 1500 кг/см^3 соответственно, мощность залежи — 2 м, расстояние между каналами — 5 м.

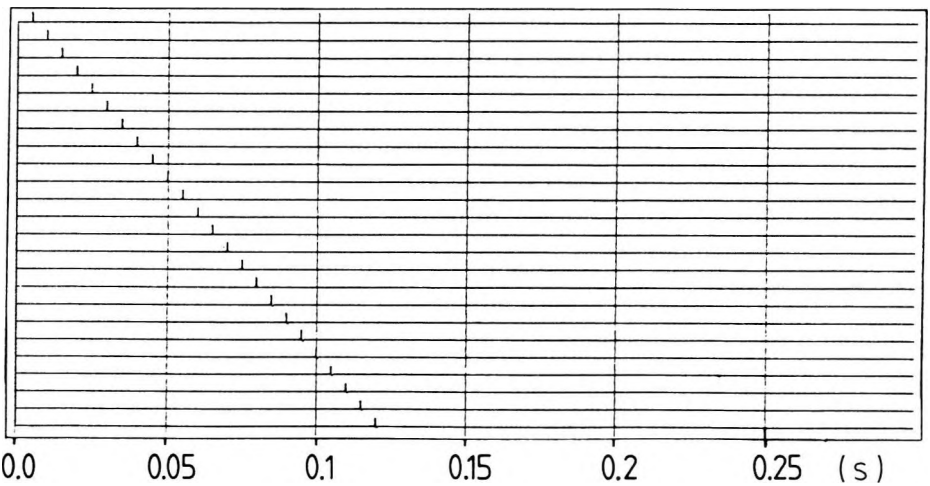

Fig. 2. Synthetic seismogram of Fig. 1 after recompressive filtering

2. ábra. Az 1. ábrán bemutatott szeizmogram a rekompressziós szűrés végrehajtása után

Рис. 2. Сейсмограмма рис. 1 после «рекомпрессивной» фильтрации.

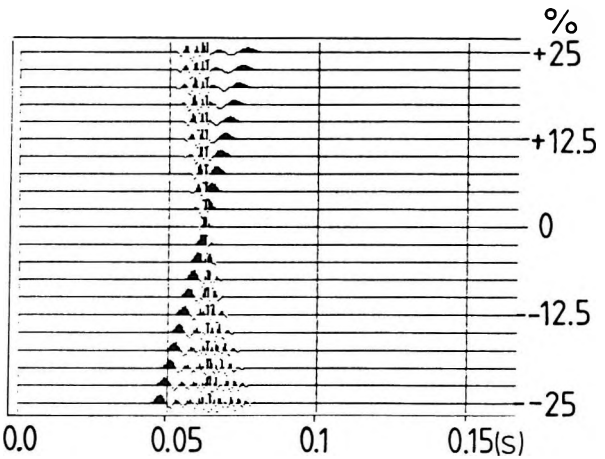

Fig. 3. Effect of erroneous β_r on the result of filtering performed on a signal computed with 125 m offset (model parameters as in Fig. 1)

3. ábra. β_r hibájának hatása a szűrés eredményére egy 125 m forráspont-érzékelő távolsággal számított csatornán (a modell paramétereket lásd az 1. ábrán)

Рис. 3. Влияние ошибок в скоростных параметрах пород на результаты фильтрации по каналу, рассчитанному для расстояния 125 м и от источника; параметры см. на рис. 1.

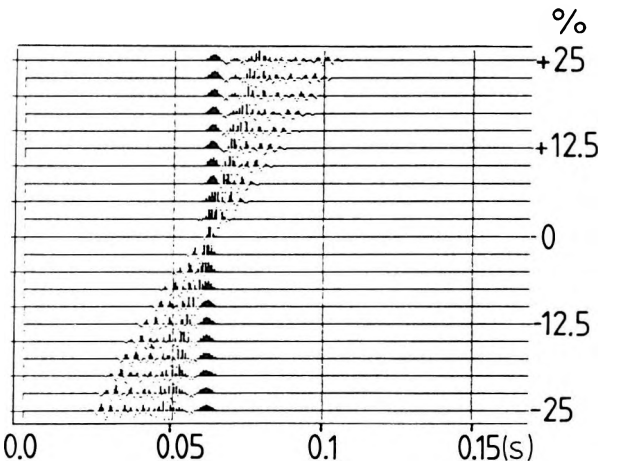

Fig. 4. Effect of erroneous β_c on the result of filtering performed on a signal computed with 125 m offset distance (model parameters as in Fig. 1)

4. ábra. β_c hibájának hatása a szűrés eredményére egy 125 m forráspont-érzékelő távolsággal számított csatornán (a modell paramétereket lásd az 1. ábrán)

Рис. 4. Влияние ошибок в скоростных параметрах углей на результаты фильтрации по каналу, рассчитанному для расстояния 125 м от источника; параметры см. на рис. 1.

The method is similarly sensitive to the other parameters, i.e. to the errors in seam thickness and densities. The diagram of *Fig. 5* summarizes the results which demonstrate the relative lengthening of the signal — compared with the length of the accurately filtered signal — as a function of the error of the parameters. It is clear that recompressive filtering is sensitive primarily to velocities, especially to that of coal and to the thickness of the seam, though the lengthening of the signal was measured somewhat arbitrarily.

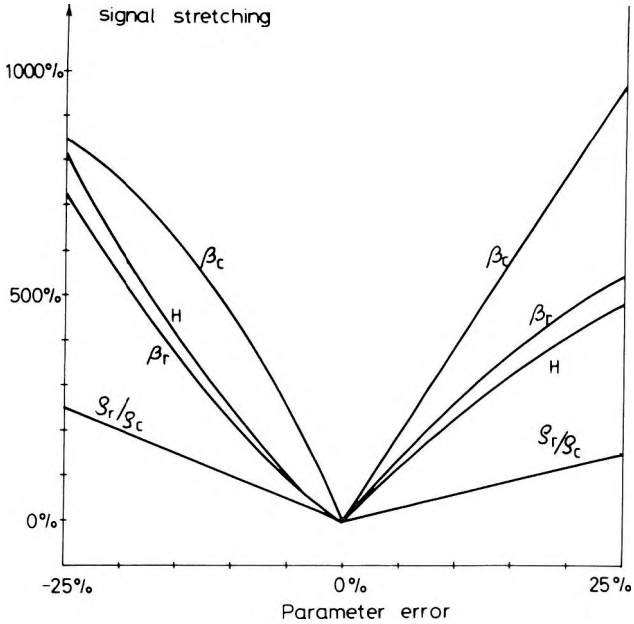

Fig. 5. Relative stretching of signal as a function of parameter errors
H — thickness of coal seam; β_r and β_c shear wave velocity in rock and coal, respectively; ϱ_r and ϱ_c — density of rock and coal, respectively

5. ábra. A jel relatív megnyúlása paraméter hibák függvényében
H — a széntelep vastagsága; β_r és β_c — a nyíróhullám sebessége a kőzetben illetve a szénben; ϱ_r és ϱ_c — a kőzet ill. a szén sűrűsége

Рис. 5. Относительное растяжение сигнала в связи с ошибками параметров:
H — мощность залежи; β_r и β_c — скорости во вмещающих породах и углях; ϱ_r и ϱ_c — их плотности соответственно.

The efficiency of filtering was also studied in the case of the superposition of several signals and in the presence of random noise, too. Furthermore, the effect of the distortions of the amplitude spectrum — caused by frequency dependent attenuation — on the filtering was tested. The seismogram of *Fig. 6.* shows the superposition of three dispersed wavelets with strong random noise added to it, while *Fig. 7* presents the filtered version of this seismogram. The figures and studies suggest that recompressive filtering is able to resolve the overlapping dispersed wavelets very well and it is not sensitive to random noise or to frequency dependent attenuation.

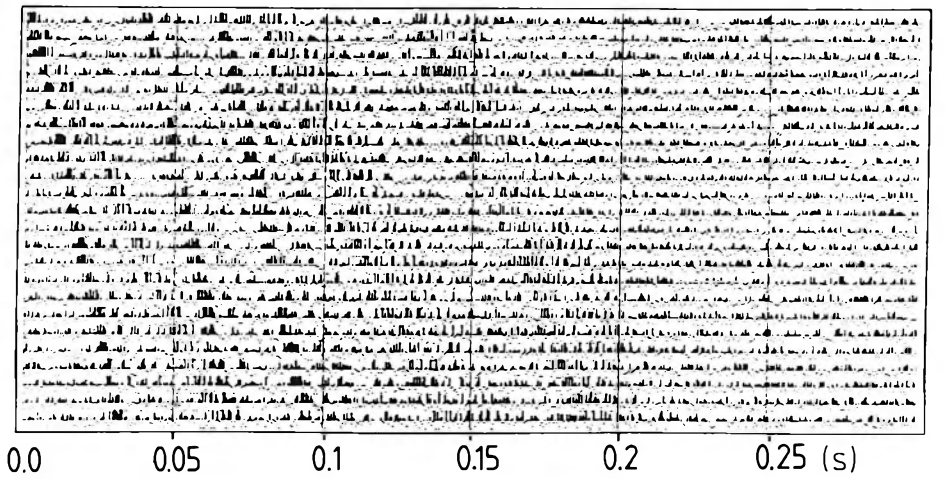

Fig. 6. Synthetic seismogram of three superposed dispersive signals, random noise added (model parameters as in Fig. 1)

6. ábra. Szintetikus szeizmogram három szuperponált diszperz beérkezéssel és rendezetlen zajjal (modell paramétereket lásd az 1. ábrán)

Рис. 6. Синтетическая сейсмограмма с тремя рассеянными вступлениями, наложенными друг на друга, и с беспорядочным шумом; параметры см. на рис. 1.

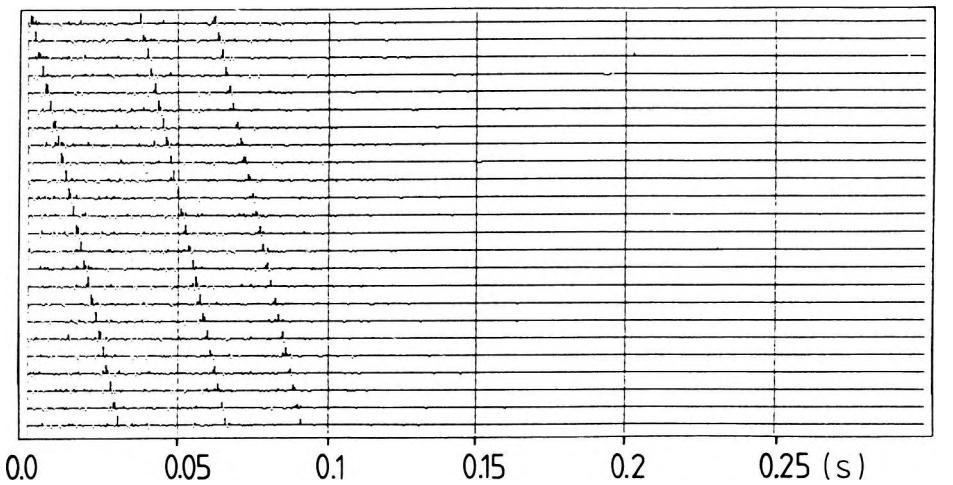

Fig. 7. Seismogram of Fig. 6 after recompressive filtering

7. ábra. A 6. ábra szeizmogramja a rekompressziós szűrés után

Рис. 7. Сейсмограмма рис. 6 после «рекомпрессивной» фильтрации.

4. Practical application of recompressive filtering

After the synthetic examples let us examine a few practical applications. *Fig. 8* presents the location map of an in-mine survey. A long panel was prepared for longwall mining in the area. The planned haulage road (*B*) whose driving was about 180 m ahead of the parallel airway (*A*) ran into an andesite dyke a few metres in thickness. The dyke was cut through but the roadway soon hit another one. Then the mining company requested a geophysical survey to determine the positions of the andesite dykes.

Taking into account the direction of the dykes the in-seam seismic reflection technique was chosen and the seismic line was placed into roadway *B* (Fig. 8). The line was shot in a one-directional six-fold offset CRP spread arrangement with 5 m spacing of two-component geophone sondes and 15 m offset. The reflection survey was completed by several transmission shots from roadway *A* for the sake of a more accurate velocity estimation.

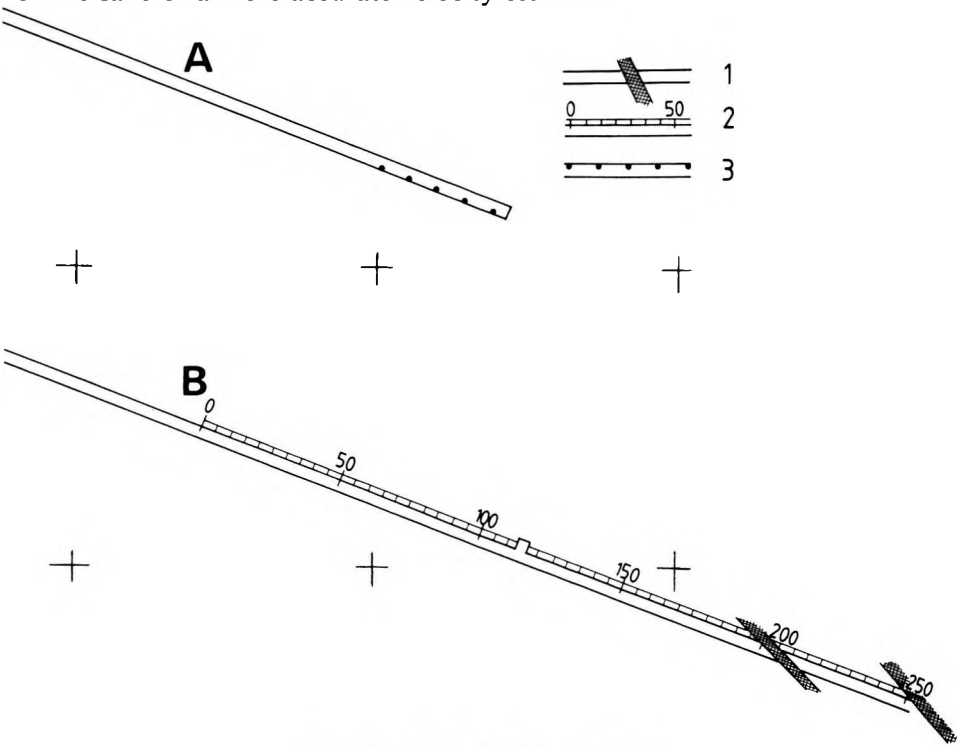

Fig. 8. Location of an in-mine survey
1 — andesite dyke; 2 — seismic reflection line; 3 — location of shots for transmission records

8. ábra. Egy bányabeli telephullám mérés helyszínrajza
1 — andezit áttörés; 2 — reflexiós mérővonal; 3 — robbantópontok átvilágító méréshez

Рис. 8. План ситуации при подземнойм измерении пластовых волн:
1 — интрузия андезитов; 2 — профиль сейсморазведки МОВ; 3 — взрывпункты для просвечивания.

Fig. 9 shows a typical seismogram of the same survey after so-called normalization, i.e. time-dependent amplification was performed. It can be seen that after the first arrivals — dying out entirely at 100–120 ms — a reflection-like arrival appears between 150 and 220 ms, though it is rather uncertain and is blurred by dispersion. *Fig. 10* presents the same seismogram after recompressive filtering which made the reflection arrival more definite and suitable for interpretation. The signal-to-noise ratio of the filtered record can be further im-

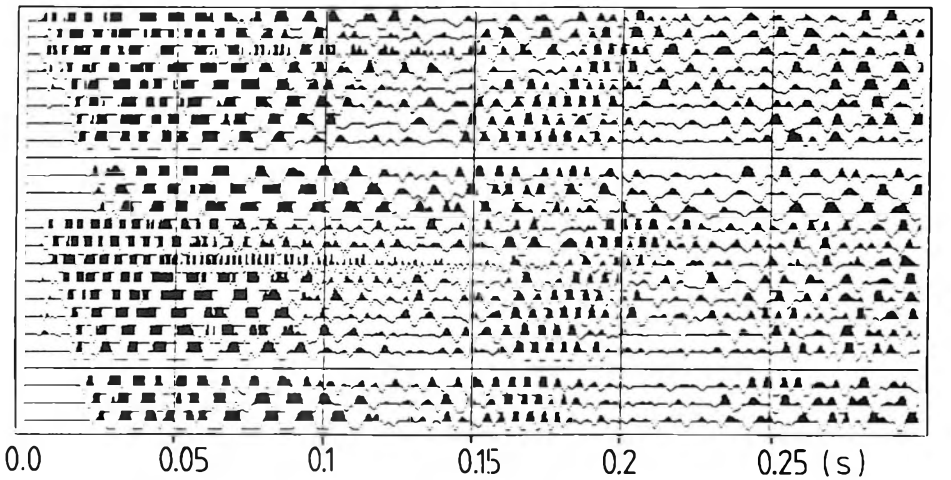

Fig. 9. Typical in-mine seismic reflection record

9. ábra. Tipikus telephullám reflexiós szeizmogram

Рис. 9. Типичная сейсмограмма отражений пластовых волн.

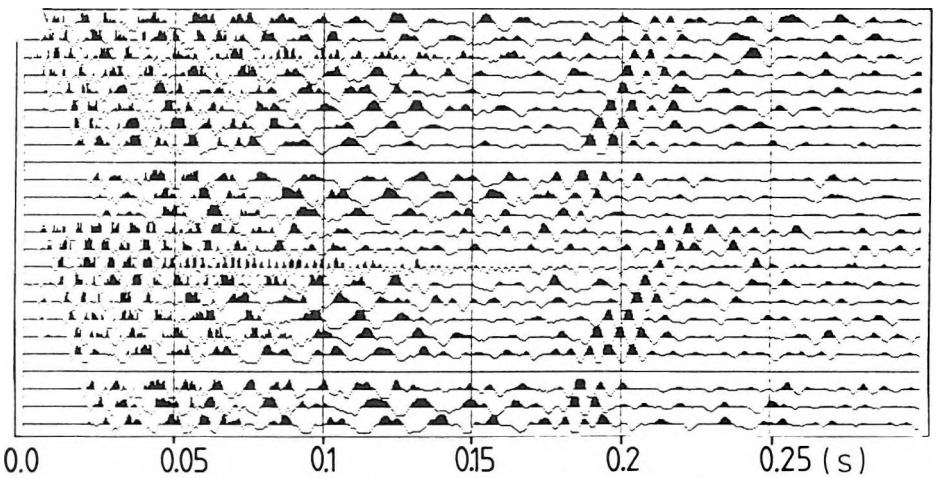

Fig. 10. Record of Fig. 9 after recompressive filtering

10. ábra. A 9. ábrán bemutatott szeizmogram recompressziós szűrés után

Рис. 10. Сейсмограмма рис. 9 после «рекомпрессивной» фильтрации.

proved by substituting the traces by their envelopes (*Fig. 11*). *Fig. 12* shows the processed time section. Though a reflected wave train can be observed in it, it is not suitable for interpretation in this form. If stacking is performed after the recompressive filtering then the reflection of Fig. 12 becomes much clearer and another one of very high frequency appears in the first half of the section (*Fig. 13*). Finally, on changing over to the envelopes by a Hilbert transform the unambiguous time-section of *Fig. 14* is obtained with a fair signal-to-noise ratio. *Fig. 15* illustrates the interpreted migrated x–y section. So far as migration is concerned, it must also be mentioned that the constant seismic velocity, chosen by us, is known due to recompressive filtering and so migration — presently a simple Kirchhoff migration — is expected to be very accurate. Fig. 15 shows that the first of the two andesite dykes hit by roadway *B* can clearly be traced and its limits accurately outlined. The second dyke hardly appears in the sections, the only exception is perhaps that of Fig. 13. This was probably caused by the fact that just over the roadway the dyke ends and so its reflection is masked by the strong first arrivals. The most important result of the survey is the third reflector — a previously unknown fault or dyke, stretching across the whole panel.

Fig. 16 shows the checking of the seismic results by roadway driving. In the case of the first dyke the real and predicted situations agreed very well. Unfortunately, the other dykes — or faults — had not been prospected by roadway driving because the mine closed the panel at the first dyke in consequence of the disturbed geology of the seam.

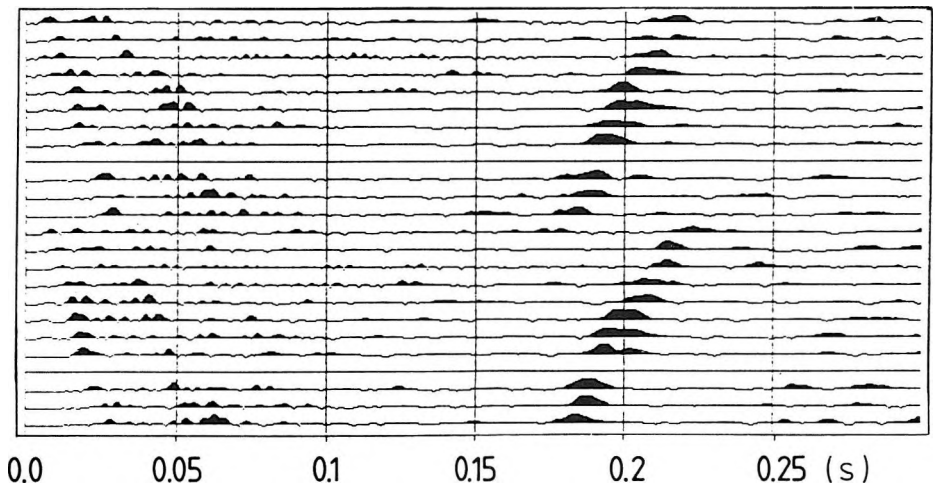

Fig. 11. Enveloped version of the record of Fig. 10

11. ábra. A 10. ábra szeizmogramja burkoló képzés után

Рис. 11. Сейсмограмма рис. 10 после создания объемлющей.

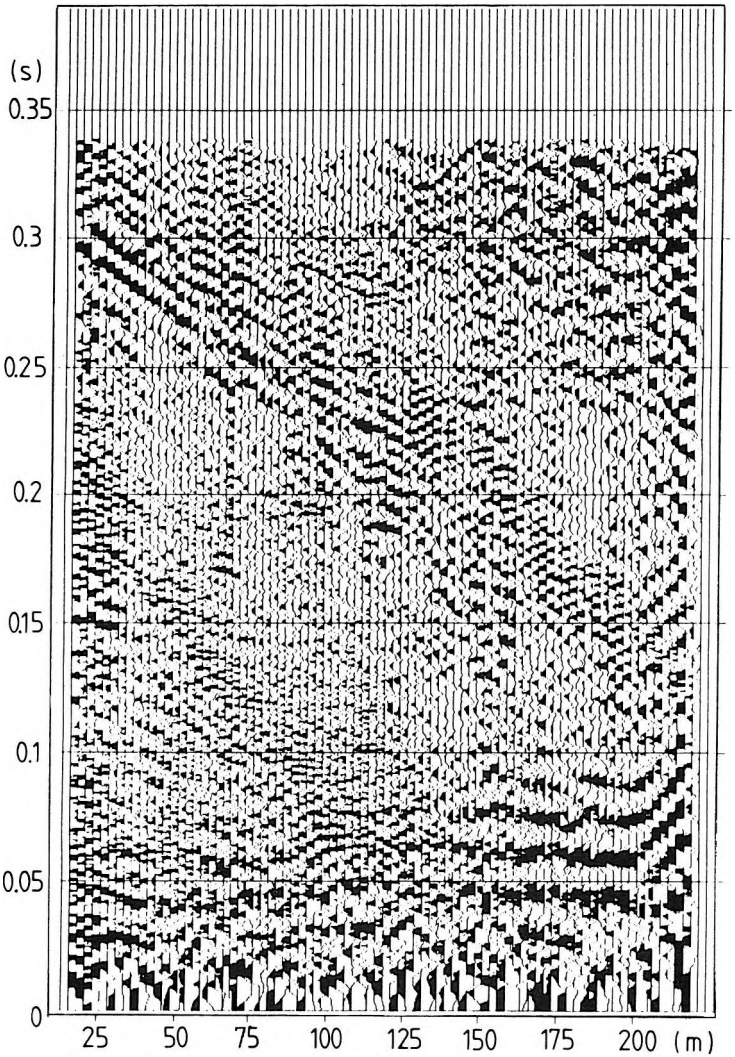

Fig. 12. Processed time section of in-mine seismic reflection survey

12. ábra. A reflexiós mérés feldolgozott időszelvénye

Рис. 12. Временной профиль, полученный в результате обработки.

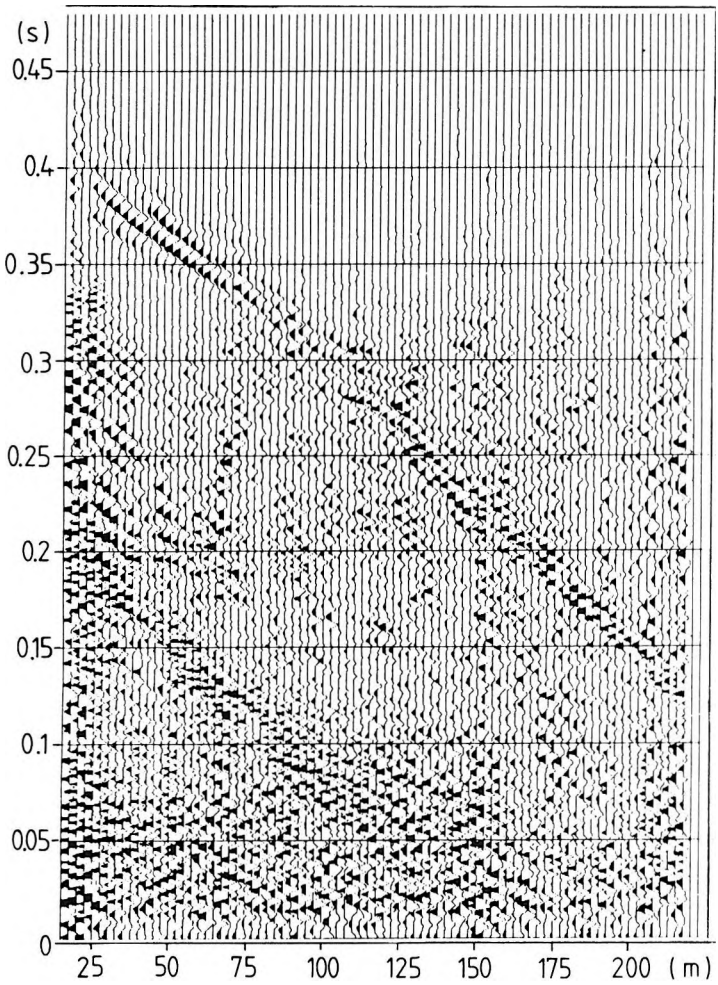

Fig. 13. Time section composed from recompressed single records

13. ábra. A nyers szeizmogramok rekompressziós szűrése után kapott időszelvény

Рис. 13. Временной профиль, полученный в результате обработки сейсмограмм с «рекомпрессивной» фильтрацией.

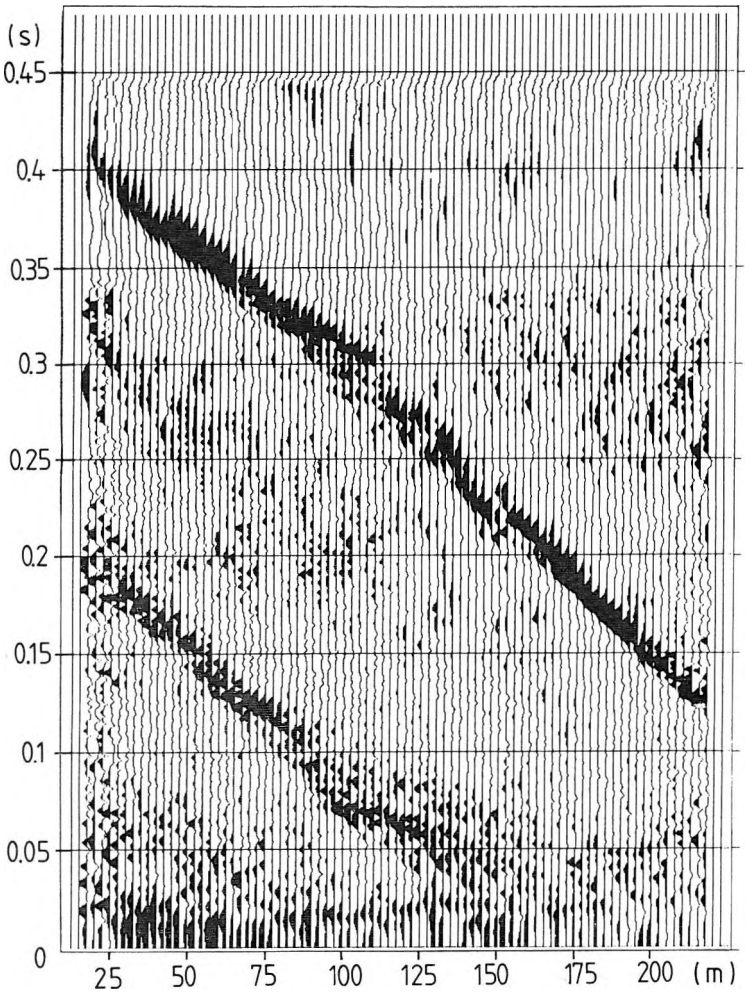

Fig. 14. Enveloped version of the time section of Fig. 13

14. ábra. A 13. ábra időszelvénye burkoló képzés után

Рис. 14. Временной профиль рис. 13 после создания объемлющей

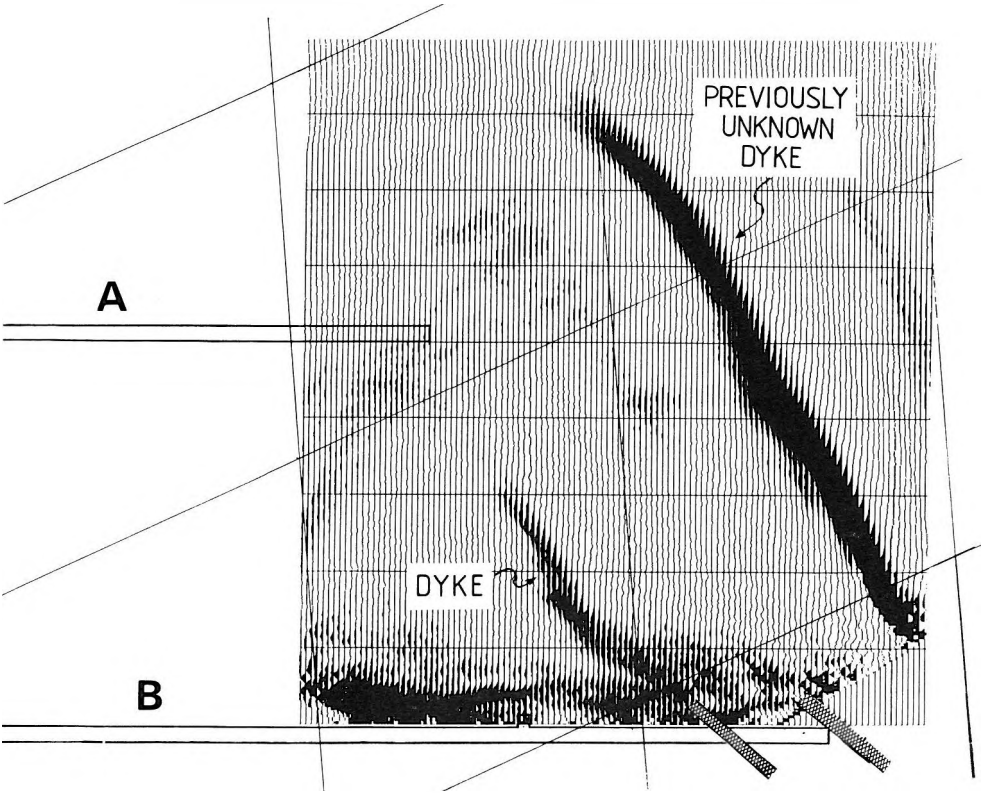

Fig. 15. Interpretation of the migrated time section (this location map is distorted by the different scales in x and y direction)

15. ábra. A mérés eredményeinek értelmezése a migrált szelvény segítségével (a szelvény x és y irányú léptékének különbsége miatt torzul a helyszínrajz)

Рис. 15. Интерпретация результатов измерений с помощью мигрированного профиля (план искажен в связи с различиями в x и y масштабах мигрированного профиля).

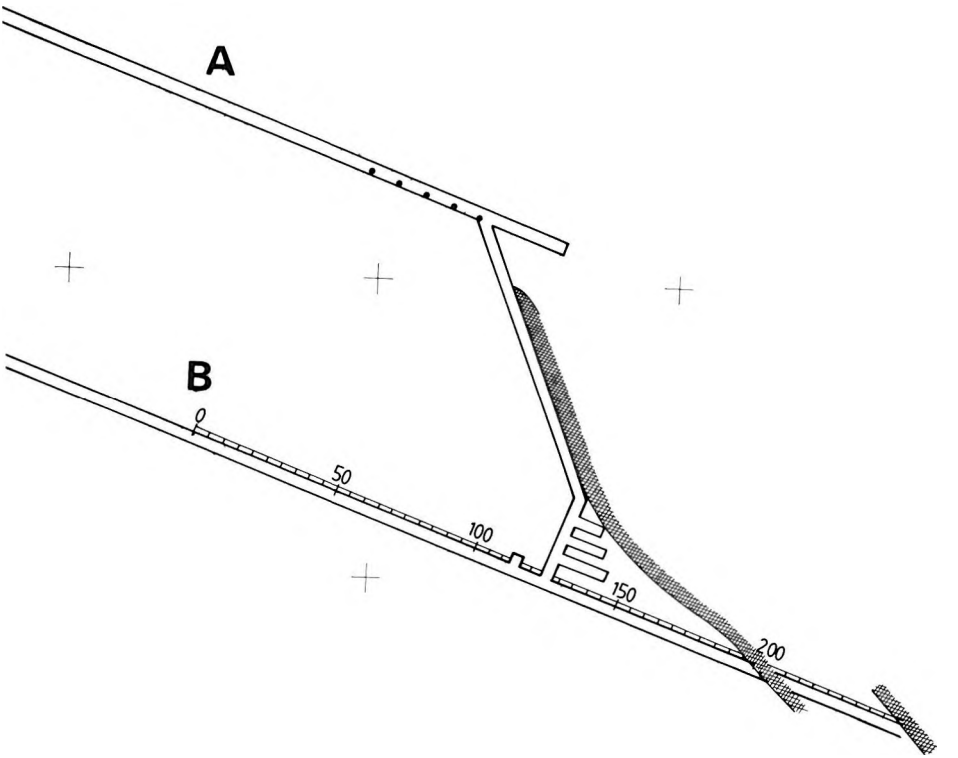

Fig. 16. Checking of results of reflection survey by roadway driving. For legend see Fig. 8

16. ábra. A mérési eredmények bányászati ellenőrzése. Jelmagyarázatot lásd a 8. ábrán

Рис. 16. Контроль за результатами измерений горными выработками. Обозначения см. на рис. 8.

5. Conclusions

On the basis of this recompressive filtering study it can be stated that

— in the case of erroneous parameters the efficiency of filtering decreases rapidly due to its deterministic character. The method is particularly sensitive to the errors of velocity and seam-thickness data, however, these data can be determined accurately enough.

— Efficiency of filtering is not sensitive at all to noise or to the distortions of the spectrum caused by absorption. The method resolves the overlapping dispersed signals well and effectively eliminates noise.

— A spectacular improvement in the quality of recorded data can be achieved by the application of recompressive filtering.

REFERENCES

BODOKY T., CZILLER E., TÁBORSZKI Gy. and TŐRÖS E. 1986: The use of seismic channel waves in coal mines. Part II. In-seam reflection measurements (in Hungarian). Magyar Geofizika, **27**, 6, pp. 197–215

BOOER A. K., CHAMBERS J. and MASON I. M. 1977: Fast numerical algorithm for the recompression of dispersed time signals. Electronic Letters, **13**, pp. 453–455

BUCHANAN D. J. 1979: The location of faults by underground seismology. Colliery Guardians, **227**, pp. 419–427

GRUSZCZYK E. and SZABELSKI S. 1981: Automatic compression program of a dispersion signal. Paper read at the 26th Geophysical Symposium, Leipzig, Proceedings of the 26th International Geophysical Symposium, pp. 223–232

KLINGE U. J., KREY Th., ORDOWSKY N. and REIMERS L. 1979: Digital in-seam reflection surveys and their interpretation by classical data processes only. Paper read at the EAEG Meeting, Hamburg

MARSCHALL L. and SCHOTT W. 1981: Treatment of dispersive wavetrains. Paper read at the EAEG Meeting, Venice, Technical Programme and Abstracts of Papers, p. 27

A REKOMPRESSZIÓS SZŰRÉS LEHETŐSÉGEI ÉS KORLÁTAI A TELEPHULLÁM SZEIZMIKUS MÉRÉSEK FELDOLGOZÁSÁBAN

BAKI György, BODOKY Tamás, CZILLER Eszter, SCHOLTZ Péter

A dolgozatban a szerzők megvizsgálják Booernek és társainak a diszperz jelek összehúzására, azaz a diszperzitás megszüntetésére javasolt eljárását. A vizsgálat kiterjed arra, hogy milyen mértékben érzékeny az eljárás hatékonysága a bemenő paraméterek hibáira, a zajokra és az abszorpció okozta spektrum torzulásokra, illetve arra, hogy milyen mértékben képes az eljárás a szuperponálódó diszperz jeleket szétbontani. A dolgozat egy bányabeli telephullám reflexiós mérés feldolgozásán keresztül bemutatja a vizsgált eljárás gyakorlati alkalmazását.

ВОЗМОЖНОСТИ И ПРЕДЕЛЫ ПРИМЕНИМОСТИ РЕКОМПРЕССИВНОЙ ФИЛЬТРАЦИИ В ОБРАБОТКЕ ДАННЫХ СЕЙСМОРАЗВЕДКИ ПО ПЛАСТОВЫМ ВОЛНАМ

Дёрдь БАКИ, Тамаш БОДОКИ, Эстер ЦИЛЛЕР и Петер ШОЛЬЦ

В статье рассматривается способ сокращения рассеянных сигналов, то-есть устранения рассеяния, предложенный Боэром с соавторами. Рассмотрены чувствительность эффективности способа к ошибкам вводимых параметров и к искажениям спектра из-за шумов и абсорпции, а также его способность к выделению рассеянных сигналов, наклодываемых друг на друга.

Практическое применение рассматриваемого способа иллюстрируется примером обработки данных измерений по отражениям пластовых волн, выполненных в горных выработках.

GEOPHYSICAL TRANSACTIONS 1988
Vol. 33. No. 3–4. pp. 237–246

IN-MINE VERTICAL SEISMIC PROFILING

Tamás ORMOS*

A 2 × 3-component geophone sonde developed for measuring interval velocity in in-mine vertical seismic profiling and a seismic source that generates enhanced *S*-waves are introduced in the paper. High-frequency (200–800 Hz) *P*- and *S*-waves can be generated and detected with the help of these tools. The errors in measuring the interval time are analysed from the viewpoint of the waveguide model — which model plays an important role in seam-wave seismics. The errors are illustrated by record sections. To eliminate the errors of time- and amplitude measurement directions for future research are suggested.

Keywords: vertical seismic profiles, *P*-waves, *S*-waves, high resolution methods, phase velocity, coal seams, seismic sources, errors

1. Introduction

Methods utilized for the data processing of in-mine seismic surveys (recompression, tomography) require a knowledge of the absorption and dispersion relations of channel waves propagating in undisturbed coal bearing complexes [DOBRÓKA 1987a,b,c, BODOKY et al. 1986, BAKI et al. this issue]. These relations can be calculated from seam-wave records [DZIEWONSKI et al. 1969, MILLAHN and ARNETZL 1980, MCMEHAN and YEDLIN 1981]. However, experience has shown that in a great number of cases dispersion of the recorded channel waves fall within a frequency band which is so narrow — because of the physical parameters of rocks — that it is not suitable for the reliable determination of the absorption–dispersion relations [ELSEN et al. 1985, MASON et al. 1985, BODOKY et al. 1986, GREENHALGH et al. 1986, BREITZKE et al. 1987]. These relations can also be calculated from the model of the waveguide if the physical parameters of the layers constituting the coal-bearing complex are known (velocity of *P*- and *S*-waves, density). [KREY 1963, DOBRÓKA and ORMOS 1983, ORMOS 1985, RÄDER et al. 1985, DOBRÓKA 1987b,d, BUCHANAN 1987].

This paper describes a VSP method modified for in-mine purposes (MVSP), which enables the velocity of *P*- and *S*-waves to be determined more accurately than is done by the traditional VSP surveys as well as providing a more detailed stratigraphic column. MVSP differs from traditional VSP [TOKSÖZ and STEWART 1984, HARDAGE 1985, RÁDLER 1985, GÖNCZ et al. 1985a,b, MÓD et al. 1985] methods by inducing *P*- and *S*-waves of one order higher

* Department of Geophysics, Technical University for Heavy Industry, Miskolc, Egyetemváros H-3515, Hungary
Manuscript received: 11 December, 1987

frequency (200–1000 Hz) and by their high-fidelity recording simultaneously at two points in the borehole in order to resolve layers having a thickness of a few metres like the coal seams.

A suitable measuring technique for realizing the above purposes has been developed at the Department of Geophysics of the Technical University for Heavy Industry over the last few years [ORMOS 1986, TAKÁCS 1986, BREITZKE et al. 1987]. An *S*-wave source and a double three-component geophone sonde were built. Interval velocities can be calculated from the differences of arrival times of *P*- and *S*-waves, respectively, at two points of the sonde (distance *L*), while the wave source is fixed. Thus, rough errors caused by the source (e.g. start time), are "automatically" eliminated. Problems of the special processing of the profiles will be treated elsewhere.

2. The sonde

Figure 1 shows the schematic structure of the sonde. It operates in a vertical position in boreholes of 60 mm nominal diameter drilled either upward or downward. The 120 mm long sensors are at the ends of the sonde (*U* and *L* in Fig. 1), and each contains three electrodynamic geophones positioned perpendicularly to each other. These PPG, GF-9-B type geophones were selected by virtue of their similar amplitude vs. frequency characteristics. (Measurements

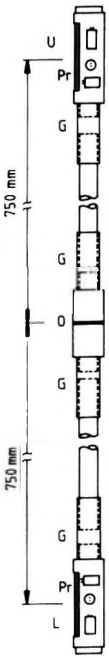

Fig. 1. Structural drawing of two-times 3-component sonde
U — upper sensor with three geophones; *L* — lower sensor with three geophones; *G* — damping rubber; *O* — orientating unit; *Pr* — pneumatic rubber pipe

1. ábra. A 2 × 3-komponenses szonda szerkezeti rajza
U — felső geofonhármas; *L* — alsó geofonhármas; *G* — gumi csillapító közdarab; *O* — orientáló egység; *Pr* — felfújható gumitömlő

Рис. 1. Блок-схема зонда, измеряющего три поинтервальные скорости по двум компонентам каждая:
U — верхняя тройка сеймоприемников; *L* — нижняя тройка сейсмоприемников; *G* — промежуточный узел из резины для усиления затухания волн; *O* — узел ориентации; *Pr* — надувная резина.

were carried out by the Research Centre of the Mecsek Coal Mines.) The velocity-amplitude vs. frequency dependence of the seismometers is constant between 20 and 1500 Hz. The cylindrical sensors are pressed against the wall of the hole pneumatically [ORMOS 1982]. The coupling between the cylindrical sonde and the approximately cylindrical borehole is rather uncertain. With a small contacting surface, resonances may be created in the frequency domain of the signals to be recorded [BEYDOUN 1984]: an effect that was especially significant in the case of the horizontal components. We followed the "three-point support" principle as a means of overcoming the resonance phenomena. Therefore three sledges (*Ss*) protruding 6 mm were attached to each sensor. Thus, both ends of the sonde (*U* and *L* in Fig. 1) were steadily pressed against the wall of the hole at three points. Pressing is achieved by inflating a pneumatic rubber pipe (*Pr*) — which is able to bulge out of the sonde — to a pressure of 0.2 MPa. The contact between the sonde and the wall of the hole is shown in *Fig. 2*. In order to enhance the *SH*-waves the sonde may be rotated to the appropriate direction, in this way realizing polarized recording according to the polarized excitation. This is done with the help of the orientating unit which is built into the middle of the sonde (*O* in Fig. 1); this unit contains a miniature compass and an optoelectric sensor. Any of the horizontal components of the sonde may be rotated in the direction that suits the excitation, before the measurement. The estimated azimuth error of rotation is 10 degrees. It can be achieved by rotation that *S*-waves appear in one component only. The advantages of such recording are that errors of the measuring technique are easy to recognize and correct and, moreover, the operation of component rotation can be omitted from data processing. Based on experience the rotation of the sonde does not increase significantly the recording time in boreholes drilled upwards.

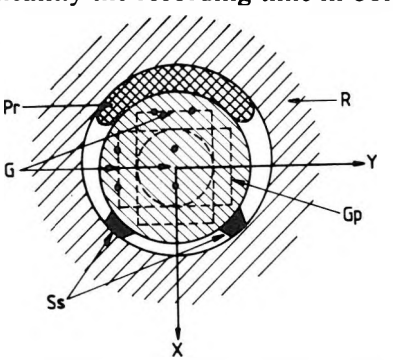

Fig. 2. Arrangement of sonde in borehole
R — rock; *Gp* — geophone probe; *Pr* — pneumatic rubber pipe; *G* — electrodynamic geophones; *Ss* — stabilizing sledges

2. ábra. A szonda elhelyezkedése a lyukban
R — kőzet; *Gp* — geofonszonda; *Pr* — felfújható gumitömlő; *G* — elektrodinamikus szeizmométerek; *Ss* — stabilizáló szánkók

Рис. 2. Расположение зонда в скважине:
R — порода; *Gp* — сейсмоприемный зонд; *Pr* — надувная резина; *G* — электродинамические сейсмометры; *Ss* — стабилизирующие «санки».

The sensors and the orientation unit are connected by metal tubes with rubber hose joints (*G* in Fig. 1) in order to damp the waves propagating in the sonde. Taking into consideration the desired resolution power, the accuracy of interval-time measurements, the portability of the tool and the distorting effect of the permanent magnetic field of the geophones on orientation, the length of the sonde was chosen to be 1.5 m. The total mass of the sonde is 3 kg.

3. Seismic sources

Seismic sources that are employed in the MVSP method must be able to generate high-frequency signals, especially high-energy *S*-waves, and they must have good reproducibility. Some rock-bolts which are widely used in Hungarian mines are suitable for that purpose if hit by a hammer, but the steady contact surface between the bolt and the hole drilled for it must be large (not point-like) [HANSÁGI 1985]. Favourable experiences have been gained with resin bonded and Split-Set rock-bolts. *Fig. 3* shows a resin bonded bolt positioned for wave generation. The highly inhomogeneous, fractured zone around the roadway and the shear stress in the bonded section of the bolt together induce the high-energy *S*-wave [ÁDÁM 1987].

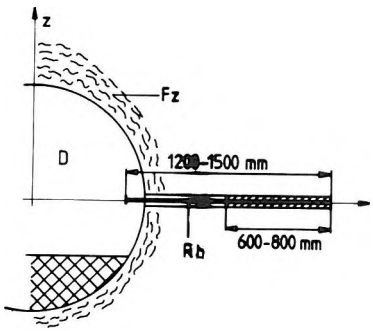

Fig. 3. Location of cemented rock-bolt for generating *S*-waves
D — roadway; *Fz* — fissured zone around the roadway; *Rb* — rock-bolt

3. ábra. A ragasztott kőzethorgony elhelyezése transzverzális hullámkeltés céljából
D — vágat; *Fz* — vágat körüli repedezett zóna; *Rb* — kőzethorgony

Рис. 3. Размещение склеенного породного якоря с целью возбуждения поперечных волн:
D — выработка; *Fz* — зона повышенной трещиноватости вокруг выработки;
Rb — породный якорь.

In order to obtain a source generating reproducible waveforms, weight dropping along forced trajectory was tested but such structures are difficult to transport and to operate in mines. In our experience manual hammer blows offer adequate reproducibility: *P*- and *S*-waves were successfully induced in the 200–800 Hz range depending on the extent of the fractured zone, on the length of the bolt, and on the quality of the bond. A typical measurement array of in-mine vertical seismic profiling is shown in *Fig. 4*.

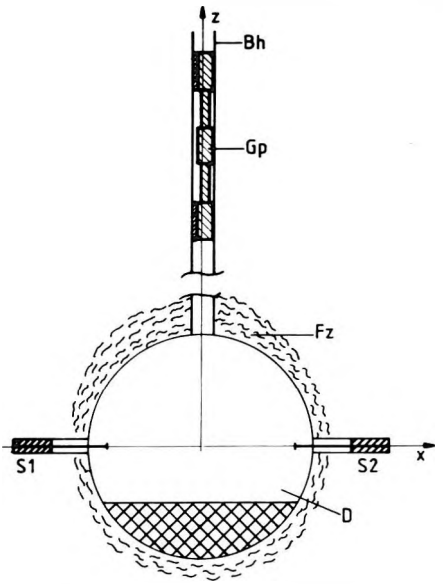

Fig. 4. Operational scheme of MVSP
Bh — borehole; *Fz* — fissured zone; *Gp* — geophone probe; *S1*, *S2* — seismic sources; *D* — roadway

4. ábra. MVSP észlelési vázlata
Bh — fúrólyuk; *Fz* — fellazult zóna; *Gp* — Geofonszonda; *S1*, *S2* — hullámforrások; *D* — vágat

Рис. 4. Схема производства наблюдений ПВСП:
Bh — скважина; *Fz* — ослабленная зона; *Gp* — сейсмоприемный зонд; *S1*, *S2* — источники волн; *D* — выработка.

4. Errors in determing interval velocities, possibilities of eliminating them

The interval velocities of *P*- and *S*-waves can be calculated from the time difference along the length of the sonde if the rock is supposed to be homogeneous in that domain [AKI and RICHARDS 1980]. The same result can be obtained by crosscorrelating the two corresponding traces. Accuracy of phase velocities is determined by the length of the sonde, amplitude- and phase conditions of wave generation and recording, amplitude- and phase characteristics of the recording instrument, sampling interval, and by the signal-to-noise ratio.

Velocities in Hungarian coal seams were found to be in the following ranges: for *P*-waves 1500–3000 m/s, for *S*-waves 700–1700 m/s. For the *P*-waves these velocities result in a 1–0.5 ms propagation time along the length of the sonde and 2–0.9 ms in the case of the *S*-waves. The rather short interval times raise the question: What is the maximum accuracy of measuring these times and how great an error of the interval velocity is caused by this inaccuracy? VERMES [1984] gave an approximate relation for estimating the lower limit of the

standard deviation of interval velocities caused by the erroneous measurement of distance and time. Because—due to the fixed distance between the two sensors of the sonde—the error of the distance measurement is negligible compared with the error of time determination, this relation may be modified as follows:

$$\sigma_v = \sqrt{2}\,\frac{v\sigma_t}{\Delta t}$$

where σ_v, and σ_t denote the standard deviation of the interval velocity and time measurement, respectively, and Δt the propagation time along the length L of the sonde. The demands of in-mine seismic methods limit the maximum standard deviation of velocities [DOBRÓKA 1987d, BAKI et al. this issue]. If we allow a maximum standard deviation for body-wave velocities of 15% then, assuming the above-mentioned velocities, the relative error of time measurement has to be reduced to below 0.1–0.05 ms in the case of the *P*-waves, and below 0.2–0.1 ms for the *S*-waves. Bearing in mind the interval times of the *P*-waves these conditions are very tight. However, it must be noted that in-mine seismics uses Love-type seam waves that contain *SH*-waves. Thus, generally we have to deal with the waveguide model of *S*-waves, for which the high frequencies generated by the above-described ways seem to provide the prescribed standard deviation.

Accuracy of phase velocity determination is influenced by the signal-to-noise ratio particularly in the case of *S*-waves. Supposing random noise AKI and RICHARDS [1980] gave a relation for estimating the error of phase velocity, viz.

$$\frac{\Delta c}{c} = \frac{1}{2\pi}\,\frac{|N(\omega)|}{|S(\omega)|}\,\frac{\lambda}{L}$$

where c, Δc, λ, $N(\omega)$ and $S(\omega)$ denote phase velocity, its relative error, wavelength and the amplitude spectra of noise and signal, respectively. Assuming, for example, a dominant frequency of 500 Hz the wavelengths will be 3–6 m and 1.5–3.5 m for the *P*- and *S*-waves, respectively. Accepting a maximum 15% error in velocity measurement the necessary smallest signal-to-noise ratio is about 5–6 dB for a wavelength of 3 m.

It is relatively simple to eliminate the errors of time measurement created by the electronic units (geophone, seismic instrument) by determining the transfer functions and selecting a suitable instrument (with the appropriate sampling rate). Some of the errors caused by the wave generation (e.g. error of start-time) "automatically" disappear during the computation of phase velocity. On the receiver side, interval velocities computed from the recorded seismograms show high standard deviation especially in sheared, disturbed complexes due to local inhomogeneities. These effects may also be eliminated by selecting the most suitable field geometry allowed by the conditions in the mine and by stacking of repeated shots.

Data processing steps and methods of in-mine vertical seismic profiling (e.g. inversion) are identical with or similar to the steps of either acoustic well logging or VSP. Taking advantage of the two sensors of the sonde there is a possibility to produce VSP profiles which are time-corrected on each trace for the *P*- and the *S*-waves. Information on the rheological features of rocks (e.g. Q_P, Q_S) can be obtained from the amplitude conditions of the records if several shots are used [DOBRÓKA 1986, BURKHARDT 1986].

5. Measurement example

A detail of an in-mine, experimental vertical seismic profile is presented in *Figs. 5* and *6*. The measurement took place in the Kányás Colliery of the Nógrád Coal Mines. The hole had been drilled vertically upward and had the nominal diameter of 60 mm. The sonde was moved with the help of the light metal bars of the MIRAKAR in-mine logging instrument which can be found at every Hungarian mining plant. After fixing the sonde pneumatically the bars were drawn back about 2 m. It must be mentioned here that it is much more advantageous to measure in an upward direction than in holes drilled downwards because in the first case the hole is always dry (there is no tube wave), pneumatic fixing requires less pressure (a hand-pump can be used), there is no danger of getting the sonde stuck or lost due to loose pieces of rock, and the sonde can be rotated easily.

The 1.5 m long sonde was moved in steps of 0.25 m and the corresponding signals (*P*- and *S*-waves) of both sensors were recorded. Thus, traces which are 1.5 m apart belong to the same shot. No processing was performed on the records except the Gaussian tapering to suppress the electronic noise of starting. The time window was shifted linearly between the first and last trace of the profile. The similar character of the adjacent signals proves that the hammer blows exhibit satisfactory reproducibility. The resonance-like phenomena caused by the inadequate fixing of the sensor and the local inhomogeneities of rocks are also well noticeable. (Survey parameters—instrument: BISON 1580 (modified); channels: 6; amplitude resolution: 8 bit; sampling rate: 0.2 ms; analog band-pass filter: 125–1000 Hz; fold: 1; recording: SHARP PC 1500; source: manual (hammer blow) on horizontal, bonded bolt; time break: galvanic contact.)

Productivity of the survey: a crew of 3–4 people is able to make 25 6-channel records per hour with the equipment of the Geophysical Department. Presently it takes about 2.2 min. to record one shot on tape which time is usually longer than the time necessary to change the location of the sonde.

Processing and plotting were performed by an HP 9000/217 computer. Interval velocities showed large standard deviation; this fact indicates the high stress in the surrounding rocks. These effects can be eliminated by further, properly located seismic sources.

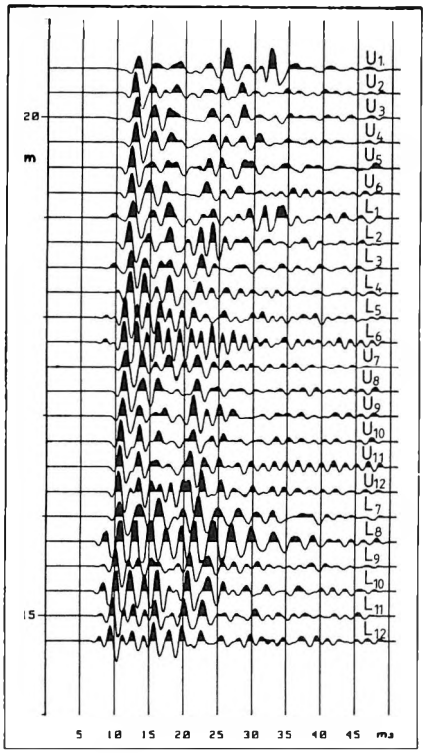

Fig. 5. MVSP profile, vertical component
Taper: 5.12–48.51 ms at 20.5 m
3.9 –48.51 ms at 14.75 m

5. ábra. MVSP szelvény, vertikális komponens
Taper: 5,12–48,51 ms 20,5 m-nél
3,9 –48,51 ms 14,75 m-nél

Рис. 5. Профиль ПВСП, вертикальная компонента. Окно со сглаженными краями:
5,12–48,51 мс при 20,5 м,
3,9 –48,51 мс при 14,75 м.

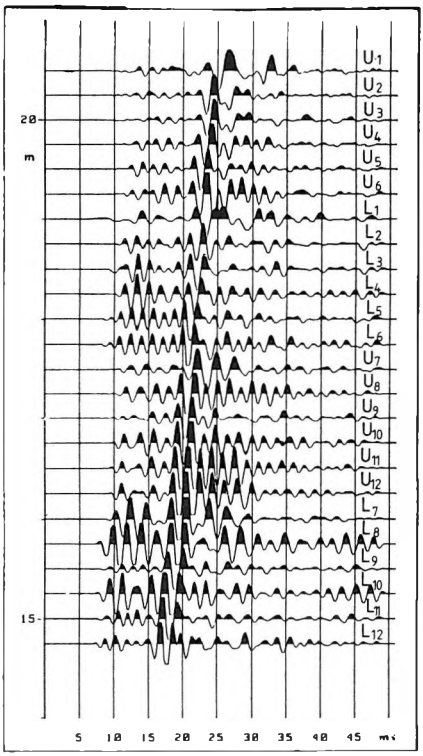

Fig. 6. MVSP profile, horizontal component
Taper: 5.12–48.51 ms at 20.5 m
3.9 –48.51 ms at 14.75 m

6. ábra. MVSP szelvény, horizontális komponens
Taper: 5,12–48,51 ms 20,5 m-nél
3,9 –48,51 ms 14,75 m-nél

Рис. 6. Профиль ПВСП, горизонтальная компонента. Окно со сглаженными краями:
5,12–48,51 мс при 20,5 м,
3,9 –48,51 мс при 14,75 м.

Acknowledgement

I express my thanks to the researchers of the Geophysical Department of the University for Heavy Industry for their very effective cooperation in establishing the equipment, and to Nógrád Coal Mines for creating the possibility for test measurements.

REFERENCES

ÁDÁM O. 1987: Seismic exploration. University text-book (in Hungarian) 264 p. Tankönyvkiadó, Budapest

AKI K., RICHARDS P. G. 1980: Quantitative Seismology. Theory and Methods. W. H. Freeman and Company. USA

BAKI Gy., BODOKY T., CZILLER E., SCHOLTZ P. 1988: Possibilities and limitations of recompressive filtering in the processing of seam-wave seismic surveys. Geophysical Transactions **33,** 3–4, pp. 221–236

BEYDOUN W. B. 1984: Seismic tool–formation coupling in boreholes. In Vertical Seismic Profiling. Part B.: Advanced concepts (Editors: Toksöz M. N. and Stewart R. R.) In Series: Helbig K., Treitel S. (Editors): Handbook of Geophysical Exploration. Section I.: Seismic Exploration, Vol. 14. B. Geophysical Press, London–Amsterdam. pp. 80–86

BODOKY T., CZILLER E., TÁBORSZKI Gy., TÖRÖS E. 1986: The use of seismic channel waves in coal mines. Part II.: in-seam reflection measurements (in Hungarian). Magyar Geofizika **27,** 6, pp. 197–215

BREITZKE M., DRESEN L., CSÓKÁS J., GYULAI Á., ORMOS T. 1987: Parameter estimation and fault detection by three-component seismic and geoelectrical surveys in a coal mine. Geophysical Prospecting, **35,** 7, pp. 832–863

BUCHANAN D. J. 1987: Dispersion calculations for *SH* and *P-SV* waves in multilayered coal seams. Geophysical Prospecting, **35,** 1, pp. 62–70

BURKHARDT H. 1986: Absorption seismischer Wellen: Bestimmungsmethoden und mögliche Nutzung. 6. Mintrop-Seminar, Kassel 13—16. Mai. 1986.

DOBRÓKA M., ORMOS T. 1983: Absorption–dispersion relations for Love channel waves. Geophysical Transactions, **29,** 2, pp. 117–127

DOBRÓKA M. 1985: The study of inhomogeneity and tectonic disturbances of coal measures by means of the absorption of seam waves. Dissertation (in Hungarian). Hungarian Academy of Sciences

DOBRÓKA M. 1987a,b: Displacement functions and absorption–dispersion relations of Love seam-waves (in Hungarian)
Part I: Magyar Geofizika **28,** 1, pp. 20–33
Part II: Magyar Geofizika **28,** 4–5, pp. 121–139

DOBRÓKA M. 1987c: The displacement functions and the absorption-dispersion properties of seam waves of the Love type (in Hungarian)
Part III: Magyar Geofizika, in press

DOBRÓKA M. 1987d: Love seam waves in a horizontally inhomogeneous three-layered medium. Geophysical Prospecting, **35,** 5, pp. 502–516

DZIEWONSKI A., BLOCH L., LANDISMAN M. 1969: A technique for the analysis of transient seismic signals. Bull. of the Seismological Soc. of America, **59,** pp. 427–444

ELSEN R., RÜTER H., SCHOTT W. 1985: Seam waves along multilayered coal seams: Some case histories. Paper presented at the 47th EAEG Meeting, 4–7 June 1985, Budapest

GÖNCZ G., RÁDLER B. 1985a: Principles of the vertical seismic profiling (in Hungarian). Magyar Geofizika, **26,** 2, pp. 43–53

GÖNCZ G., KÉSMÁRKY I., VÉGES I. 1985b: Processing of short offset VSP data (in Hungarian). Magyar Geofizika, **26,** 2, pp. 66–88

GREENHALGH S. A., BURNS D., MASON I. 1986: A cross-hole and face-to-borehole in-seam seismic experiment at Invincible Colliery, Australia. Geophysical Prospecting, **34,** 1, pp. 30–55

HANSÁGI I. 1985: Practical rock mechanics in ore mining (in Hungarian). Müszaki Kiadó, Budapest. 172 p.

HARDAGE B. (Editor) 1985: Vertical Seismic Profiling. Part A.: Principles. In Series: Helbig K., Treitel S. (Editors): Handbook of Geophysical Exploration. Section I.: Seismic Exploration, Vol. 14.A. Geophysical Press, London–Amsterdam

KREY Th. 1963: Channel waves as a tool of applied geophysics in coal mining. Geophysics, **28,** 5, pp. 701–714

Mason I., Greenhalgh S., Hatherly P. 1985: A channel wave transmission study in the Newcastle coal measures, Australia, Geoexploration, **23,** 3, pp. 395–413

Millahn K. O. and Arnetzl H. H. 1980: Some aspects of two-component in-seam seismology. Theodor Krey Fortschrift. Prakla Seismos GmBH

McMechan G. A. and Yedlin M. J. 1981: Analysis of dispersive waves by wave field transformation. Geophysics, **46,** 6, pp. 896–874

Mód G., Rádler B., Tóth J. 1985: VSP-field procedures (in Hungarian). Magyar Geofizika, **26,** 2, pp. 54–65

Ormos T. 1982: Development of a three-component seismic sonde (in Hungarian). Exploration Report for Mecsek Coal Mines

Ormos T. 1985: The formation of Love seam waves in the Borsod coal basin. Thesis (in Hungarian). Technical University for Heavy Industry, Miskolc

Ormos T. 1986: Determination of tectonic disturbances from galleries by the transmission and reflection method of seismic seam waves (in Hungarian). Exploration Report for Borsod Coal Mines

Rádler B. 1985: Vertical seismic profiling (in Hungarian). Magyar Geofizika, **26,** 2, pp. 41–42

Räder D., Schott W., Dresen L., Rüter H. 1985: Calculation of dispersion curves and amplitude-depth distribution of Love channel waves in horizontally-layered media. Geophysical Prospecting. **33,** 6, pp. 800–816

Takács E. 1986: Development of an in-mine geophysical method to clarify the depth conditions of footwall dolomite in the surroundings of a starting gallery (in Hungarian). Exploration Report for the Bauxite Mines of Fejér County

Toksöz M. N. and Stewart R. R. (Editors) 1984: Vertical Seismic Profiling. Part B: Advanced Concepts. In Series: Helbig K., Treitel S. (Editors): Handbook of Geophysical Exploration. Section I.: Seismic Exploration, Vol. 14. B. Geophysical Press, London–Amsterdam

BÁNYABELI VERTIKÁLIS SZEIZMIKUS SZELVÉNYEZÉS

ORMOS Tamás

A dolgozat bányabeli vertikális szeizmikus szelvényezés céljaira alkalmas 2 × 3 komponenses intervallumsebességet mérő szeizmométerszonda, valamint transzverzális hullámokat kiemelten gerjesztő hullámforrás fejlesztéséről számol be, amelyekkel nagyfrekvenciás (200—800 Hz) longitudinális és transzverzális hullámok gerjesztése és vétele oldható meg. A telephullámszeizmikában fontos hullámvezető csatornamodell meghatározásának szempontjait szem előtt tartva elemzi az intervallumidő mérésének hibáit, amelyeket mért szeizmogram-szelvénnyel illusztrál. Az idő- és amplitúdómérések hibáinak kiküszöbölésére további fejlesztési irányt javasol.

ПОДЗЕМНОЕ ВЕРТИКАЛЬНОЕ СЕЙСМИЧЕСКОЕ ЗОНДИРОВАНИЕ

Тамаш ОРМОШ

Излагаются результаты разработки сейсмометрического зонда, измеряющего три поинтервальные скорости по двум компонентам каждая, и источника волн, специфически возбуждающего поперечные волны, предназначенные для подземного вертикального сейсмического зондирования, с помощью которого можно решить проблему возбуждения и регистрации высокочастотных (200–800 гц) продольных и поперечных волн. С учетом особенностей опеделения канала-волновода, имеющего большое значение в сейсморазведке по пластовым волнам, дается анализ ошибок в измерении поинтервальных времен с иллюстрацией в виде профиля по измеренным сейсмограммам. Предлагаются дальнейшие работы по устранению ошибок в измерениях времен и амплитуд.

GEOPHYSICAL TRANSACTIONS 1988
Vol. 33. No. 3–4. pp. 247–266

ON THE ASSESSMENT OF PERMEABILITY AND THERMAL CONDUCTIVITY IN DEEP-SEA CLAYS BY ELECTRICAL AND ACOUSTIC MEASUREMENTS

M. A. LOVELL*

A laboratory examination of a suite of nine surficial samples from the North East Atlantic has been carried out using a modified oedometer cell which enables the simultaneous measurement of electrical formation factor, thermal conductivity, compressional wave velocity, and shear wave velocity, during a conventional uniaxial consolidation test. Permeability and porosity values are derived from uniaxial consolidation theory. Electrical formation factor and compressional wave velocity exhibit close interrelationships with permeability and the capability of predicting the measured permeability both empirically and theoretically to within an order of magnitude is shown. The empirical prediction may be improved by additional input aimed at defining the structure of the sample (e.g. initial void ratio or shear wave velocity). Thermal conductivity and electrical formation factor each exhibit a dependence on porosity for saturated sediments. Using this common parameter, porosity, it is possible to successfully relate the electrical formation factor of a saturated sediment to its thermal conductivity. Compressional wave velocity anisotropy exists and may be expected for other energy transfer processes. This directional dependence, whilst not critical in thermal observations in surficial sediments, may become important at depth and particularly for fluid flow predictions throughout the sediment column.

Keywords: thermal conductivity, marine sediments, P-waves, S-waves, velocity, electrical formation factor, oedometer

1. Introduction

The current search for a suitable repository in which high-level radioactive waste can be safely confined over long periods of time has led to renewed interest in the geotechnical properties of the deep ocean floor. Previously the majority of research into the role of the sea floor in a geotechnical framework has been as a foundation materical in the exploration for, and exploitation of, hydrocarbons on the continental shelf. In this field the notable success in identifying individual geotechnical parameters by geophysical means is well documented [TAYLOR SMITH 1971, 1983, JACKSON et al. 1981]. In attempting to identify a suitable location for such a storage requirement, two geotechnical parameters are of special concern, the permeability and thermal conductivity of the medium. Both of these quantities have been studied extensively in soils [LOUDON

* Marine Science Laboratories, University College of North Wales, Menai Bridge, Anglesey, LL59 5EY, U.K. Now at Department of Geology, University of Nottingham, University Park, Nottingham, NG7 2RD, U. K.
Manuscript received: 14 July, 1987

1952, De Vries and Afgan 1975], although their determination for large volumes of material by direct testing is both problematical and expensive [Pane et al. 1983, Nickerson 1978, Lovell and Ogden 1983]. Apart from their direct bearing on the radioactive waste programme, both parameters are of particular interest in the study and modelling of hydrocarbon formation, and also with the proposed laying of sensitive fibre-optic communication cables on the sea floor.

2. Background

Marine sediments may be considered as assemblages of grains, the pore spaces between which are filled with a pore fluid. Generally this pore fluid consists largely of seawater, although, under certain circumstances, quantities of gas may also be present. The proportion of space taken up by the pores is referred to as the porosity, being the ratio of the volume of voids to the total volume. The major drawback with porosity, if any, is its static, scalar nature. The porosity of two sediments, one isotropic, one anisotropic, may be equal although many geotechnical and geophysical parameters will exhibit variations according to the direction or orientation of the measurements within that framework. A parameter which extends the concept of the pore space in terms of its distribution and interconnections is the permeability of the medium.

Electrical flow in marine sediments has been considered both theoretically and experimentally, and relationships between porosity and electrical formation factor shown to exist [Schopper 1966, Boyce 1968, Jackson, Taylor Smith and Stanford 1978, Mendelson and Cohen 1982]. Generally electrical flow is considered to take place through the saline pore fluid, the grains themselves acting relatively as insulators; this holds for clays, where the particle structure may exhibit certain conducting properties, in the presence of a saline pore fluid [Brace et al. 1965]. The extension of electrical flow as being analogous to fluid flow permeability has been noted frequently and various attempts at relating the two exist [Archie 1942, Schopper 1966, Brace 1977]. However, questions as to the role of the pore space in defining the two individual flows have been raised [Dullien 1979], for while a dependency is ubiquitously proposed, the precise scale and nature is ill-defined.

Compressional wave measurements in porous media, both in-situ and in the laboratory, have shown the dependence of the speed of propagation on the nature and distribution of the pore fluid. At a given porosity the speed of propagation falls considerably if a small quantity of the pore fluid is replaced by gas, whilst for a saturated sediment an inverse relationship between the speed of propagation and porosity is well documented [Nafe and Drake 1957, Boyce 1976]. Electrical flow, which is also dependent on the pore fluid phase of a sediment, has been noted as exhibiting some form of analogy with fluid flow, while sound speed is known to exhibit anisotropy in foliated clays, though whether this is due to a difference in the fluid flow arrangement of the sediment

structure or its elasticity is difficult to determine [HAMDI and TAYLOR SMITH 1982]. Shear wave velocity in comparison exhibits little dependence on the pore fluid, but is very dependent on the nature of the particle framework of the sediment, and indeed to particle orientations (i.e. it is sensitive to anisotropic grain fabrics).

In attempting to show the effect of permeability on the propagation of seismo-acoustic waves, HAMDI and TAYLOR SMITH [1982] effected a theoretical model along the lines proposed by BIOT [1956, 1962a, 1962b], and input data obtained for a variety of marine sediments (*Fig. 1*)*. This theoretical connection between fluid flow and compressional wave velocity is particularly interesting in the light of earlier discussions. In defining the model, a mass coupling factor, b, is introduced. For $b = 1$ there is no fluid — solid coupling; a mass coupling factor of 1 thus forms a limiting boundary condition in the absence of an accurate value, and indeed the broken lines of Fig. 1 are computed on this basis. BROWN [1980] has suggested that through an analogy with electrical and fluid flow it may be possible to derive a value for b, pertinent to each sample, where

$$b = FFn,$$

where FF = electrical formation factor,
n = fractional porosity.

The value so derived would form a lower limit to the value of b and whilst the magnitude does not vary greatly the model is reasonably sensitive to it. To evaluate the effect of changing the value of b by this technique, formation factor values have been computed for the data presented in Fig. 1 by substituting the porosity values into Archie's law

$$FF = n^{-m}$$

where the exponent value m is in general agreement with the work on formation factor — porosity relationships [TAYLOR SMITH 1971, JACKSON et al. 1978]; these are listed in *Table I*. The modified results are plotted in Fig. 1 as solid lines and show an improved fit, although neither of the sets of predictions is far from the measured values.

3. Experimental procedure

Whilst much of the interest focusses on non-cohesive sediments and porous media generally, this paper is concerned with cohesive sediments from the deep sea environment which may be adequately sampled, relatively speaking, but which suffer non-reversable deformation during laboratory testing such as described here. The samples must therefore be tested on a basis of one measure-

* The author uses different expressions in the following figures (e.g. coefficient of permeability, oedometer permeability, etc.) but the dimension (m/s) proves that the variable on the horizontal axes is the filtration coefficient. *Editor*

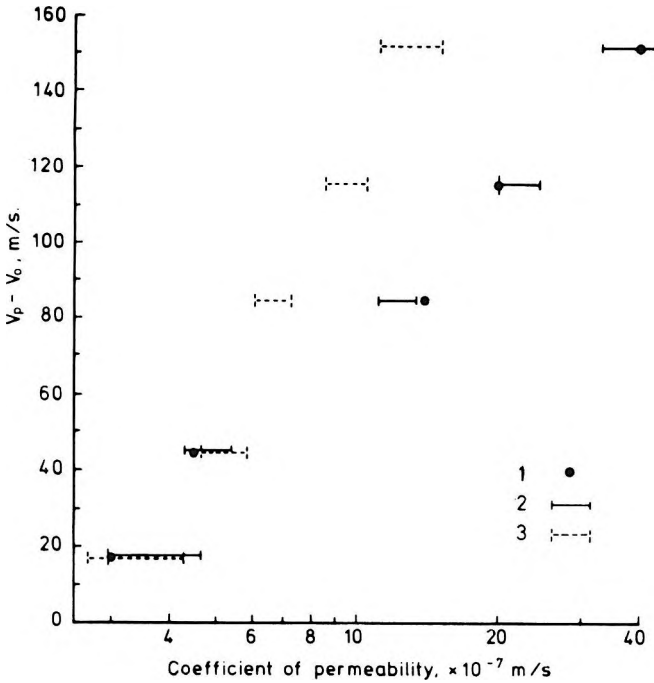

Fig. 1. Permeability values computed from Biot's model for mass coupling factor $b = 1$ and $b = FFn$ plotted, together with measured permeabilities, against velocity discrepancy (measured–calculated for zero frequency), after HAMDI and TAYLOR SMITH [1982]
1 – measured values: 2 – predicted values with $b = FFn$; 3 – predicted values with $b = 1$

1. ábra. Mért és számított permeabilitás értékek. A számítás a Biot-féle modell alapján, a tömegcsatolási tényező két különböző értékével ($b = 1$ és $b = FFn$) történt. Ábrázolás a sebesség eltérés (mért–0 frekvenciára számított) függvényében [HAMDI és TAYLOR SMITH 1982 nyomán]
1 – mért érték; 2 – $b = FFn$-nel számítva; 3 – HAMDI és TAYLOR SMITH képletével számítva

Рис. 1. Значения проницаемости, рассчитанные на основе модели Био при двух различных значениях фактора соединения масс $b = 1$ и $b = FFn$, нанесенные, совместно с измеренными значениями проницаемости как функция расхождений в скоростях, измеренных и рассчитанных для нулевых частот [по HAMDI и TAYLOR SMITH 1982]:
1 – измеренные значения; 2 – значения, рассчитанные по формуле $b = FFn$; 3 – то же, по формуле HAMDI и TAYLOR SMITH.

Table I. Data used in constructing Figure 1

I. táblázat. Az 1. ábra szerkesztéséhez használt adatok

Таблица I. Данные по составлению рис. 1.

Sample No.	Permeability			Porosity n %	Formation factor	Archie slope
	Measured 10^{-7} m/s	Computed ($b = 1$) 10^{-7} m/s	Computed ($b = FFn$) 10^{-7} m/s			
1	3.0	4.5	3.7	0.600	2.50	−1.8
2	4.6	5.4	4.8	0.549	2.94	−1.8
3	14.0	6.7	12.0	0.445	4.00	−1.7
4	20.0	8.9	22.0	0.430	3.34	−1.4
5	40.0	12.0	42.5	0.393	3.12	−1.3

ment routine per undisturbed specimen. To maximise the data so obtained the measurements are based on the use of a standard soils engineering oedometer or consolidometer, whereby one sample is mechanically loaded to provide a series of consecutive physical states. In this way permeability values are derived from consideration of uniaxial consolidation theory, while thermal conductivity is measured using the transient needle probe technique [VON HERZEN and MAXWELL 1959, BLOOMER and WARD 1979].

3.1 The modified oedometer

During the test, a specimen is confined laterally in a ring, some 75 mm in diameter and 20 mm tall, and is subjected to uniaxial loading, applied in static increments over time intervals of 24 hours or more; during this period the sample is compressed and the pore fluid expelled to the adjacent porous stones, above and below the sample. When the excess pore fluid pressure is reduced to zero the sample is said to have completed its primary consolidation; it is at this point that the geophysical measurements are made. The oedometer thus reproduces, at least to a first approximation, the mechanical loading of a sediment which may occur on the sea floor. The applied vertical pressure in the test may be equated to a depth in the sediment column; the depths so reproduced depend on the nature of the sample, but for pressures up to 800 kPa are in the region down to 150 m.

The modified oedometer cell *(Fig. 2)* is based on the design of a fixed ring cell. The modifications allow for the inclusion of the geophysical measuring elements, and in particular the cell is constructed out of electrically non-conducting polyvinyl chloride (PVC) to allow meaningful electrical resistivity measurements to be made on the sample. The sample is contained in a ring,

which is seated on a basal porous stone. A top cap, which is free to move inside the ring, transfers the axial load to the sample via another porous stone. Beyond each of the two porous stones is located a perspex housing, containing the piezoelectric transducers and electrical connections.

Compressional wave velocity measurements are made using two 1 MHz piezoelectric transducers and these provide for a vertical propagation path through the saturated porous stones and sample. An additional pair located in the side walls of the base allow for measurements in the horizontal direction. Shear wave velocity measurements are made using two piezoelectric bimorph crystals; these each protrude some 3 mm into the sample in order to obtain adequate shear wave transmission. The techniques for the measurement of the compressional and shear wave velocities are fully described by HAMDI and TAYLOR SMITH [1982].

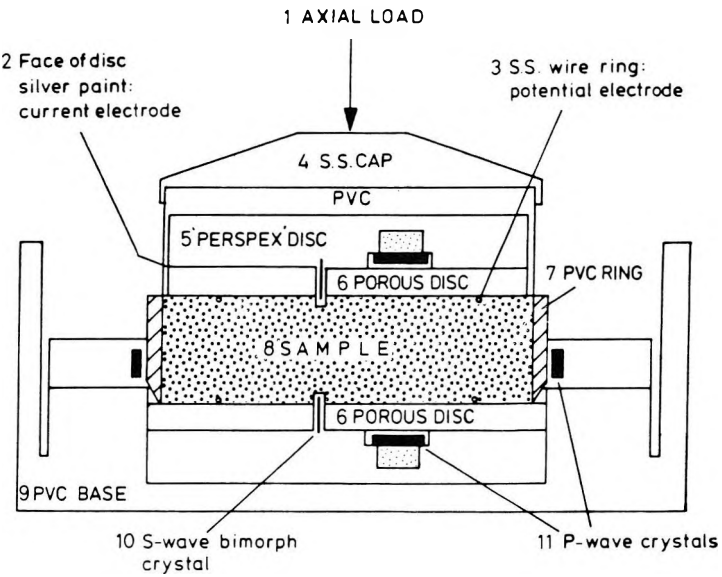

Fig. 2. The modified oedometer cell

2. ábra. Módosított ödométer cella
1 – tengelyirányú terhelés; 2 – a korongot borító ezüst festék az áram elektróda; 3 – rozsdamentes acél huzal: potenciál elektróda; 4 – rozsdamentes acél sapka; 5 – „PERSPEX" korong; 6 – porózus korong; 7 – PVC gyűrű; 8 – minta; 9 – PVC foglalat; 10 – *S*-hullám gerjesztő és érzékelő kristály; 11 – *P*-hullám gerjesztő és érzékelő kristály

Рис. 2. Модифицированная ячейка эдометра:
1 – осевая нагрузка; 2 – токовый электрод – серебряная краска, покрывающая диск; 3 – электрод потенциалов — провод из нержавеющей стали; 4 – колпак из нержавеющей стали; 5 – диск «PERSPEX»; 6 – пористый диск; 7 – кольцо из полихлорвинила; 8 – образец; 9 – патрон из полихлорвинила; 10 – кристалл, возбуждающий и воспринимающий поперечные волны; 11 – кристалл, возбуждающий и воспринимающий продольные волны.

Electrical resistivity is monitored during the test using a vertically orientated 4-electrode array. The outermost two current electrodes are the inner surface of each of the perspex housings, which are coated with electrically conducting silver paint. The two inner potential electrodes are located at the interfaces between the porous stones and the sample, each in the form of a single circular stainless steel wire. An alternating current (0.4 Hz) is passed between the two outer electrodes and the electrical resistance of the sample monitored at the inner electrodes. This resistance may in turn be converted to a resistivity, or an electrical formation factor (electrical resistivity of the sample normalised with respect to the resistivity of the pore fluid).

Additionally, it is possible to introduce a thermal conductivity needle probe horizontally into the cell. The needle (70 mm in length, 0.8 mm diameter) allows the thermal conductivity to be determined within 100 seconds.

A total of nine samples have been tested in this study; each originated from the N. E. Atlantic, off Madeira, sampled by Kastenlot gravity corer in water depths of approximately 5000 m.

3.2 Results

Previous attempts at defining the permeability and thermal conductivity of a sedimentary material have related each of the parameters to the porosity or void ratio of the sample. In extending this concept to geophysical measurements a relationship is known to exist between porosity and electrical formation factor for sedimentary rocks [ARCHIE 1942] and saturated clean marine sands [JACKSON et al. 1978], and also for individual measurements on large numbers of marine samples [BOYCE 1968]. The oedometer, however, enables a series of measurements to be made on a single sample for a range of porosities as the sample is mechanically consolidated under increasing increments of axial load. The porosity-electrical formation factor results are documented in detail elsewhere [LOVELL and OGDEN 1983, LOVELL 1985]. *Figure 3* is a typical linear plot on a log-log scale for any one sample; this follows the Winsauer equation [WINSAUER et al. 1952.]

$$FF = Cn^{-m}$$

rather than the Archie equation [ARCHIE 1942]

$$FF = n^{-m}$$

(note that the well-known Humble formula $FF = 0.62\, n^{-2.15}$ is but a particular form ot the Winsauer equation). Plotting all of the data together, however, gives a broad zone which may be roughly approximated by a 3rd degree polynomial [see LOVELL 1983].

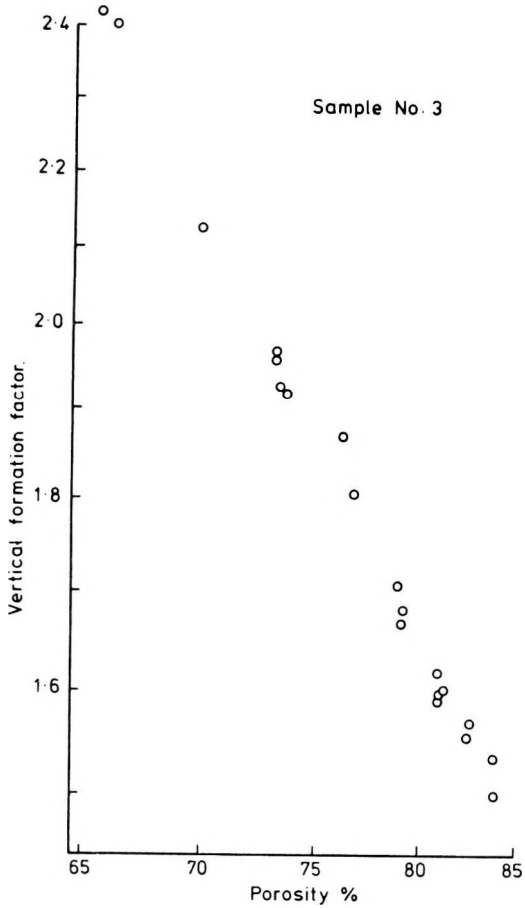

Fig. 3. Apparent formation factor plotted against porosity for one deep-sea sediment sample

3. ábra. Látszólagos formáció faktor a porozitás függvényében, egyetlen mélytengeri üledékmintára

Рис. 3. Кажущийся формационный фактор как функция пористости для отдельно взятой пробы глубоководных осадков.

4. Permeability

Permeability may be determined either directly, in which the rate of fluid flow is measured under a known induced pressure gradient, or indirectly whereby a value is derived from theoretical consideration of the consolidation behaviour of a sample. The latter are normally between one and two orders of magnitude less than those measured directly [BRYANT et al. 1981, HAMDI 1981]. Whilst there is no definitive explanation of this phenomenon, various experimenters have pointed to the difference in the state of the samples being

tested, particularly the strain imposed in the oedometer. This strain, while creating a large hydraulic gradient which would tend to produce a high value of permeability, is countered by the particle rearrangement which may tend to reduce the flow channels resulting in a decrease in permeability. The permeability values produced here are derived from consolidation theory; however, since both these and direct measurements are fluid flow dependent, it would seem likely that some relationship between one permeability data set and a geophysical parameter should be tenable for the alternative data set using some, as yet, undefined transfer process.

4.1 Empirical relationships

LOVELL [1985] has shown that permeability exhibits a unique relationship with void ratio for each sample during consolidation. Since the void ratio, in terms of the porosity, has been shown to exhibit a relationship with electrical formation factor, this relationship may be exhibited in terms of a permeability — formation factor plot *(Fig. 4)*. Similar work on sands [LOVELL 1985] shows the slope of each plot to be a function of the pore shape, while the relative position of each is a function of the particle size distribution. For each of the clays considered the permeability can be predicted to within an order of magnitude, simply from the formation factor measurement. However, consideration of the shear wave velocity characteristics of the samples shows the initial shear wave velocity to decrease in an inverse trend with initial void ratio, or proportionally with initial formation factor. Hence utilisation of this measurement may help to further define the precise magnitude of the permeability. The shear wave velocity — depth profiles may be separated into three groups on the basis of initial void ratio *(Fig. 5)*. Similarly, the formation factor — permeability plots may be separated on the same basis *(Fig. 6)*. This connection between the permeability and the shear wave velocity is reasonable within one grade of sediment since the shear wave velocity may be expected to reflect the sediment structure, and for samples within one sediment grade may expose relative features.

4.2 Theoretical relationship

It is possible to predict the permeability of a marine sediment on the basis of Biot's equations [HAMDI and TAYLOR SMITH 1982]. *Figure 7* shows a clear relationship between the oedometer-derived permeability and that predicted using the simple model based on Biot's equations by HAMDI and TAYLOR SMITH with the mass coupling factor b defined as BROWN [1980] suggested; $b = FFn$. The slope of the line is 1. Unfortunately, the experimental arrangement here does not allow a thorough evaluation of the model for the materials under study, although its success in identifying the permeability to within an order of magnitude is obvious. It is interesting, also, to note that the predicted value

bears a similar relation to the oedometer-derived value as would be expected for a directly measured value (i.e a discrepancy of some two orders of magnitude).

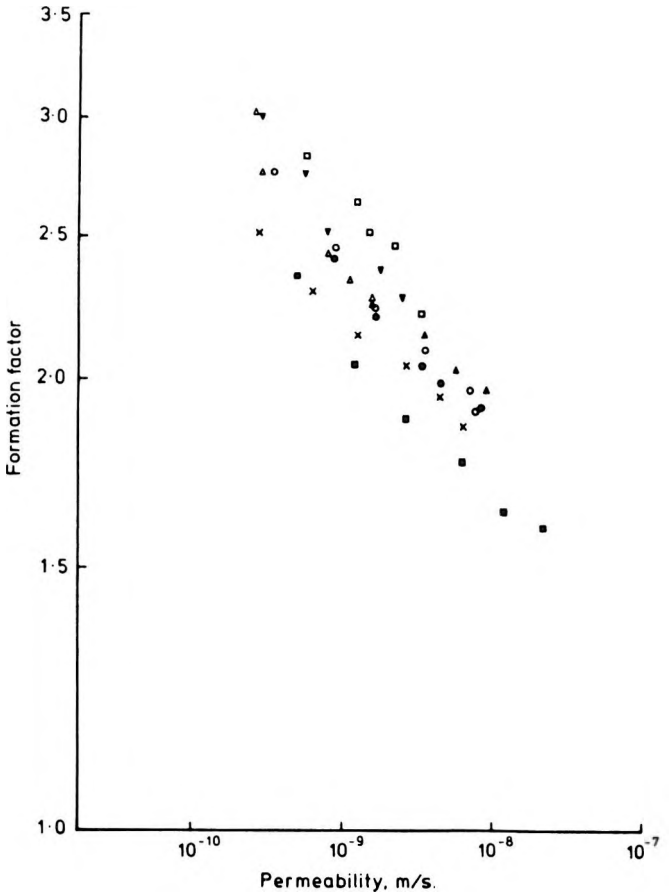

Fig. 4. Apparent formation factor plotted against permeability for 8 deep-sea clays

4. ábra. Látszólagos formáció faktor a permeabilitás függvényében, 8 mélytengeri agyagra

Рис. 4. Фактор кажущейся формации как функция проницаемости для восьми проб глубоководных глин.

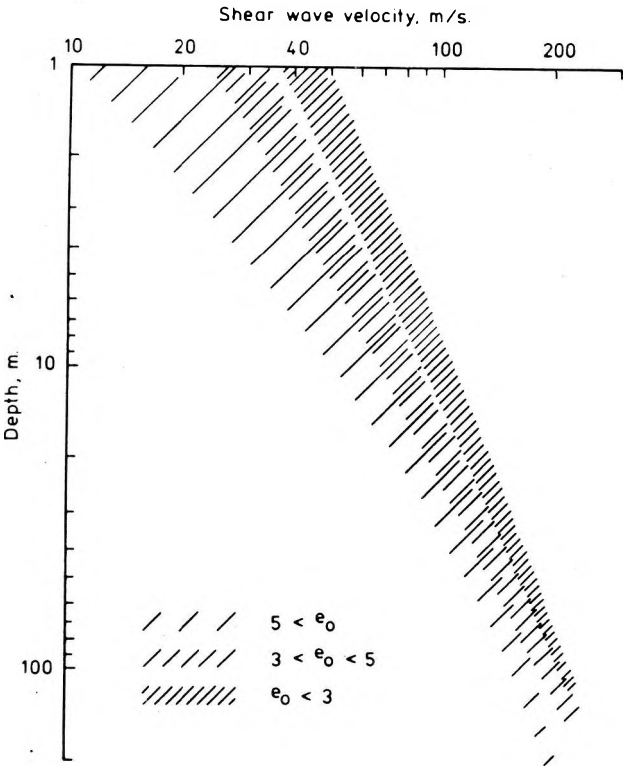

Fig. 5. Shear-wave velocity variation with oedometer-simulated depth; zonations are based on initial void ratio e_0

5. ábra. A nyíróhullám sebességének változása az ödométerrel szimulált mélységgel. A zónák az e_0 kezdeti porozitással kapcsolatosak

Рис. 5. Колебания скорости скалывающих волн с глубиной, симулированной эдометром; зоны выделены на основе начальной пористости e_0.

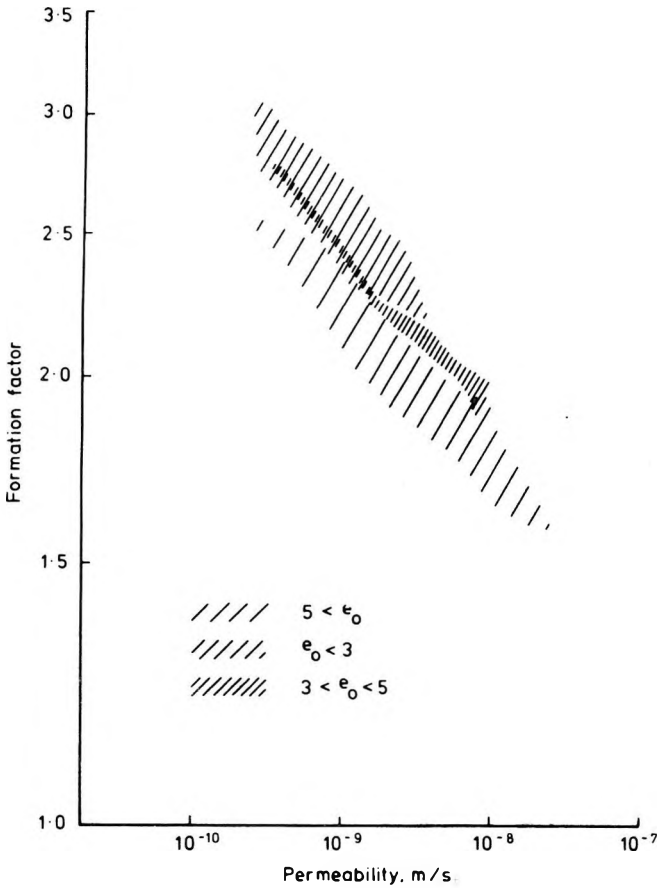

Fig. 6. Data of Fig. 4 zoned on initial void ratio (e_0) as in Fig. 5

6. ábra. A 4. ábra adathalmaza, az e_0 kezdeti porozitásnak megfelelő zónákra osztva, mint az 5. ábrán

Рис. 6. Данные рис. 4, распределенные по зонам в соответствии с начальной пористостью, как и на рис. 5.

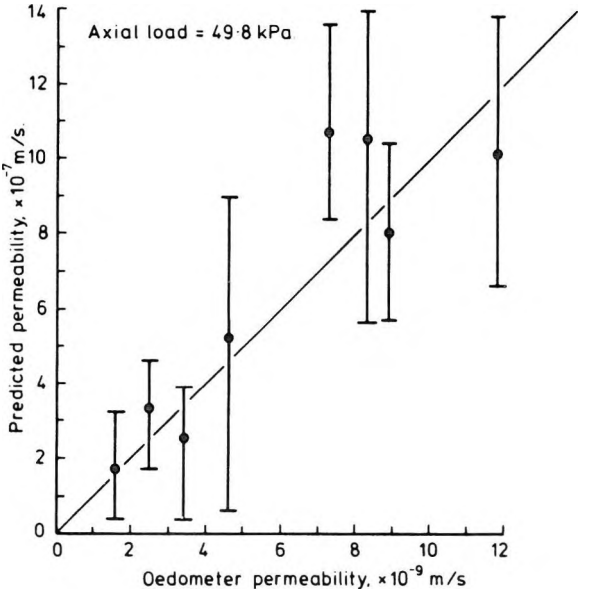

Fig. 7. Permeability values calculated from HAMDI and TAYLOR SMITH's model (intervals) plotted against oedometer-derived permeability values (dots) for eight samples at similar axial loading

7. ábra. HAMDI és TAYLOR SMITH modellje szerint számított permeabilitás értékek intervallumai, ödométerből levezetett permeabilitás értékek (pontok) függvényében, nyolc mintára, hasonló tengelyirányú terhelés mellett

Рис. 7. Значения проницаемости, рассчитанные по модели HAMDI и TAYLOR SMITH (отрезки), нанесенные как функция значений проницаемости, полученных эдометром (точки), для восьми проб при сходных осевых нагрузках.

5. Thermal conductivity

Previous thermal conductivity measurements on deep sea clays have exhibited a clear dependence on the water content of the sample [BULLARD et al. 1956]; for a saturated sediment this may be expressed in terms of the porosity. Emphasis has also been given to the use of the geometric equation [LICHTENECKER 1926, SASS et al. 1971] for expressing the thermal conductivity of a porous system:

$$k_b = k_s^{(1-n)} k_w^n$$

$$\log k_b = n(\log k_w - \log k_s) + \log k_s$$

where k is the thermal conductivity and subscripts b, s and w refer to the bulk, solids, and pore fluid. Measurements on nine samples at various stages, prior to, during, and after, the loading cycle, provide a total of twenty data points

which when plotted on a log — arithmetic scale give a linear trend, [Lovell 1985]; i.e. general adherence to the geometric equation *(Fig. 8)*. The scatter may be real, or may be due to the severe time limits imposed on the measurement by the size of the sample. Interpreting the data by the geometric equation provides a solid conductivity value of 2.01 W/mK and a fluid conductivity value of 0.61 W/mK. Since both the electrical formation factor and the thermal conductivity may be related to the porosity of the sediment, it appears possible to relate the electrical and thermal measurements through this common parameter.

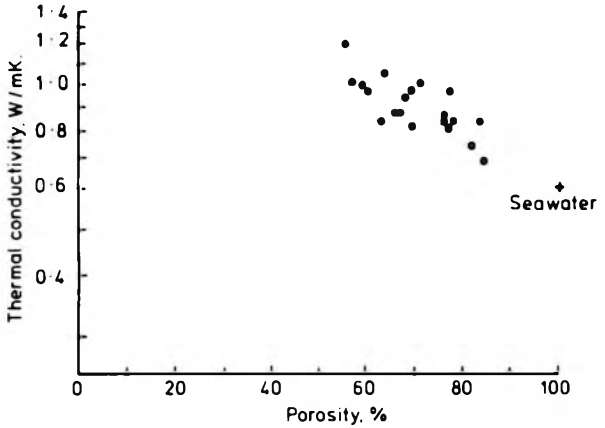

Fig. 8. Thermal conductivity plotted against porosity for all samples [Lovell 1985] in three stages (7 points absent due to measurement problems)

8. ábra. A hővezető képesség a porozitás függvényében, az összes mintára [Lovell 1985], három fokozatban (7 pont hiányzik mérési problémák miatt)

Рис. 8. Теплопроводность как функция пористости для всех проб [Lovell 1985] в три стадии (семь точек пропущены в связи с измерительными проблемами).

6. Discussion and conclusion

The results presented here and elsewhere suggest that routine geophysical measurements can predict both the permeability (to within an order of magnitude) and the thermal conductivity of a deep-sea clay. For permeability the approach may be empirical or theoretical although whichever is chosen the measurement of a number of geophysical parameters in an integrated scheme will provide better limits on the magnitude predicted. Thermal conductivity, meanwhile, for a saturated sediment is capable of prediction simply through the geophysical determination of the porosity; this is most accurately achieved in high porosity clays by the electrical formation factor.

In considering the success evident in these results, together with the suggestions for improving the predictions, it is interesting to consider the experimental

arrangement in relation to the state of the samples. All of the results are presented as though any one sample is homogeneous and isotropic, and remains so during the test. However, it has been possible with the experimental arrangement shown in Fig. 2 to measure both the horizontal and vertical compressional wave velocities. These show a consistent, though slight, anisotropy to exist, the horizontal velocity being slightly greater than the vertical *(Fig. 9)*. For the thermal conductivity measurements using the needle probe, the measurement relates to the planes perpendicular to the axis of the needle *(Fig. 10)*. Thus for

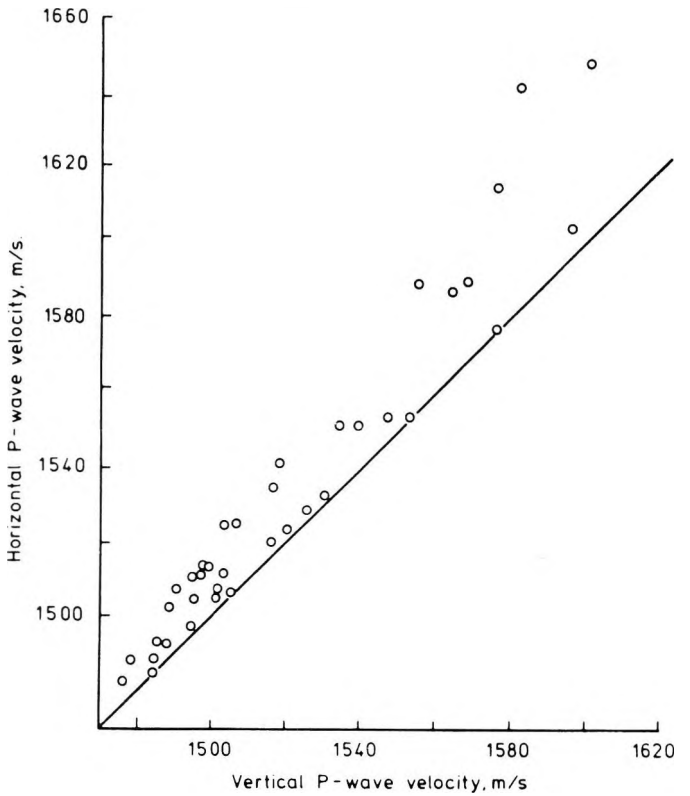

Fig. 9. Anisotropy of *P*-wave velocity for all samples in several stages

9. ábra. A *P*-hullám sebesség anizotrópiája, az összes mintára, több fokozatban

Рис. 9. Анизотропия скоростей продольных волн для всех проб в несколько стадий.

the needle vertical the measurement would approximate to the horizontal conductivities, k_x, k_y; for the needle horizontal, as in this test, the measurement approximates to a mean value between the vertical conductivity, k_z, and one of the horizontal conductivities k_x or k_y. In vertically anisotropic media k_z may differ from k_x and k_y, which themselves will tend to be the same. Thus measurements with the needle verticle will tend to be greater than those made with the

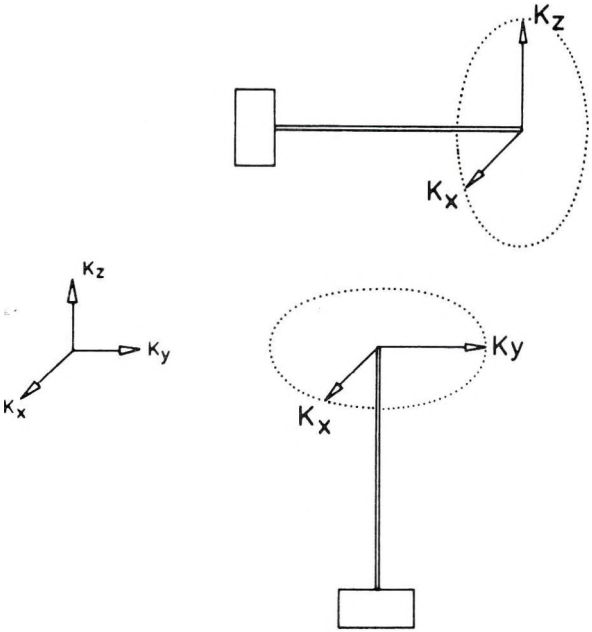

Fig. 10. Thermal conductivity needle and measurement orientation (dotted line represents isothermal locations)

10. ábra. Hővezetőképesség-mérő szonda mutatója és mérési irány (a pontozott vonal izotermát jelöl)

Рис. 10. Стрелка зонда для измерения теплопроводности и ориентировка измерений (пунктирными линиями обозначены изотермы).

needle horizontal. *Figure 11* shows this anisotropic effect for measurements made on vertically compacted sands in the laboratory, with the needle horizontal and vertical [Lovell 1985].

Since anisotropy is evident in vertically compacted sands for thermal measurements, and in deep sea clays for compressional wave velocity measurements, then in the light of the results presented earlier, anisotropy may be considered plausible for fluid flow in such media. Whilst these effects may be slight in near surface materials and in mechanically loaded samples, they may be important at greater depths, particularly where time-related effects such as particle bonding may occur.

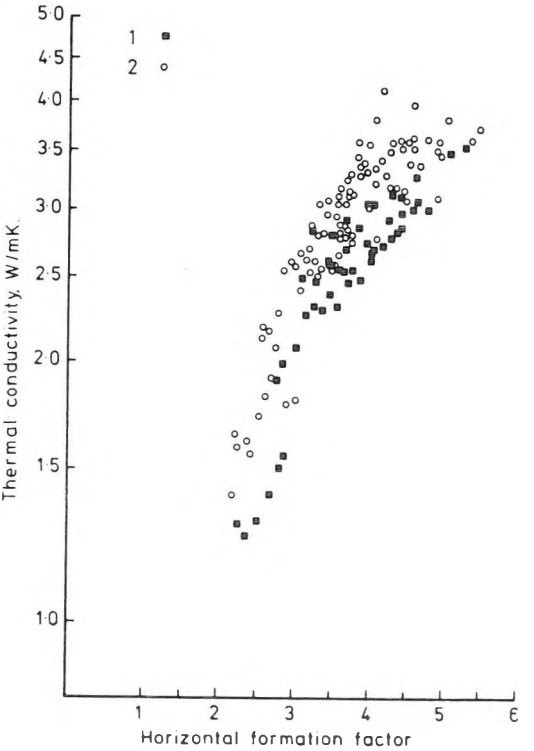

Fig. 11. Thermal conductivity anisotropy for a suite of artificial sands [after LOVELL 1985]
1 – needle horizontal; 2 – needle vertical

11. ábra. Hővezető képesség anizotrópia egy sor mesterséges homokra [LOVELL 1985 nyomán]
1 – a mutató vizszintes; 2 – a mutató függőleges

Рис. 11. Анизотропия теплопроводности в различных искусственных песках [по LOVELL 1985]:
1 – стрелка в горизонтальном положении; 2 – стрелка в вертикальном положении.

Acknowledgements

This work was carried out under contract with the European Atomic Energy Community (Contract No. 263–81–7) WAS UK and the Department of the Environment (Contract No. RKM4100). In addition to this financial support, the author wishes to thank D. Taylor Smith for constructive criticism throughout the programme, and to acknowledge the help of many colleagues in assistance with the laboratory work, the provision of samples, and innumerable helpful discussions.

REFERENCES

ARCHIE G. E. 1942: The electrical resistivity log as an aid in determining some reservoir characteristics. Transactions of the American Institute of Mining, Metallurgical and Petroleum Engineers, **146,** pp. 54–62

BIOT M. A. 1956: Theory of propagation of elastic waves in a fluid saturated porous solid. I: Low frequency range pp. 168–178. II: Higher frequency range. J. Acoust. Soc. Am., **28,** pp. 179–191

BIOT M. A. 1962a: Generalised theory of acoustic propagation in porous dissipative media. Journal of Applied Physics, **33,** pp. 1254–1264

BIOT M. A. 1962b: Mechanics of deformation and acoustic propagation in porous media. Journal of Applied Physics, **33,** pp. 1482–1498

BLOOMER J. R. and WARD J. 1979: A semi-atuomatic field apparatus for the measurement of thermal conductivities of sedimentary rocks. J. Phys. E., **12,** pp. 1033–1035.

BOYCE R. R. 1968: Electrical Resistivity of Modern Marine Sediments from the Bering Sea. Journal of Geophysical Research, **73,** 14, pp. 4759–4766

BOYCE R. E. 1976: Sound velocity — density parameters of sediment and rock from DSDP Drill sites 315–318. In Initial Reports of the Deep Sea Drilling Project, **33,** pp. 695–728.

BRACE W. F. 1977: Permeability from Resistivity and Pore Shape. J. Geophys. Res., **82,** 23, pp. 3343–3349

BRACE W. F., ORANGE A. S. and MADDEN T. R. 1965: The effect of pressure on the electrical resistivity of water saturated crystalline rocks. Journal of Geophysical Research, **70,** 22, pp. 5669–5678

BROWN R. J. S. 1980: Connection between formation factor for electrical resistivity and fluid — solid coupling factor in Biot's equations for acoustic waves in fluid-filled porous media. Geophysics, **45,** 8, pp. 1269–1275

BRYANT W. R., BENNET R. H. and KATHERMAN C. E. 1981: Shear Strength, Consolidation, Porosity, and Permeability of Oceanic Sediments. pp. 1555–1616. Offprint from: The Sea, **7.** The Ocean Lithosphere. John Willey & Sons

BULLARD E. C., MAXWELL A. E. and REVELLE R. 1956: Heat flow through the deep sea floor. Advances in Geophysics **3,** pp. 153–181

DE VRIES D. A. and AFGAN N. H. 1975: Heat and Mass Transfer in the Biosphere Part 1. Transfer Processes in the plant environment. John Wiley & Sons.

DULLIEN F. A. L. 1979: Porous media: fluid transport and pore structure. Academic Press, 396 p.

HAMDI F. A. I. 1981: Variations of seismic velocity with depth in nearsurface marine sediments and their engineering significance. Ph. D. thesis, University of Wales (unpubl.)

HAMDI F. A. I. and TAYLOR SMITH D. 1982: The influence of permeability on compressional wave velocity in marine sediments. Geophysical Prospecting, **30,** 5, pp. 622–640

JACKSON P. D., TAYLOR SMITH D. and STANFORD P. N. 1978: Resistivity–porosity–particle shape relationships for marine sands. Geophysics, **43,** 6, pp. 1250–1268

JACKSON P. D., BARIA R. and MCCANN D. M. 1981: Geotechnical Assessment of Superficial Marine Sediments Using In-situ Geophysical Probes. Ocean Management, **7,** 1–4, pp. 189–209

LICHTENECKER K. 1926. Die Dielektrizitätskonstante natürlicher und künstlicher Mischkörper. Physik Z. **27,** pp. 115–158

LOUDON A. G. 1952: The computation of permeability from simple soil tests. Geotechnique, **3,** pp. 165–183

LOVELL M. A. 1983: Resistivity–porosity–thermal conductivity relationships for marine sediments. Ph. D. Thesis, Univ. of Wales (unpubl.)

LOVELL M. A. 1985: Thermal Conductivity and Permeability Assessment by Electrical Resistivity Measurements in Marine Sediments. Marine Geotechnology, **6,** 2, pp. 205–240

LOVELL M. A. and OGDEN P. 1983: Remote Assessment of Permeability/Thermal Diffusivity of Consolidated Clay Sediments. Report to the European Atomic Energy Community, published in the EUR-series, Brussels [1984]. EUR 9206 EN.

MENDELSON K. S. and COHEN M. H. 1982: The effect of grain anisotropy on the electrical properties of sedimentary rocks. Geophysics **47,** 2, pp. 257–263

NAFE J. E. and DRAKE C. L. 1957: Variation with depth in shallow and deep water marine sediments of porosity, density and the velocities of compressional and shear waves. Geophysics **22,** 3, pp. 523–552

NICKERSON C. R. 1978: Consolidation and Permeability Characteristics of Deep Sea Sediments: North Central Pacific Ocean. M. Sc. thesis (unpubl.) Worcester Polytechnic Institute, Worcester, Massachusetts, U.S.A.

PANE V., CROCE P., ZNIDARCIC D., KO H-Y, OLSEN H. W. and SCHIFFMAN R. L. 1983: Effects of consolidation on permeability measurements for soft clay. Geotechnique **33,** pp. 67–72

SASS J. H., LACHENBRUCH A. H. and MUNROE R. J. 1971: Thermal conductivity of rocks from measurements on fragments and its application to heat-flow determinations. J. Geophys. Res., **76,** 14, pp. 3391–3401

SCHOPPER J. R. 1966: A theoretical investigation on the formation factor — permeability — porosity relationship using a network model. Geophysical Prospecting **14,** 3, pp. 301–341

TAYLOR SMITH D. 1971: Acoustic and electric techniques for seafloor sediment identification. Proceedings of International Symposium on Engineering Properties of sea floor soils and their geophysical identification. Seattle, Washington, pp. 235–267

TAYLOR SMITH D. 1983: Seismo-acoustic wave velocities and sediment engineering properties. In "Acoustics and the Sea Bed" (Conference). (ed. N. Pace) University of Bath Press.

VON HERZEN R. P. and MAXWELL A. E. 1959: The measurement of thermal conductivity of deep-sea sediments by a needle probe method: Journal of Geophysical Research, **64,** 10, pp. 1557–1563

WINSAUER W. O., SHEARIN A. M., MASSON P. H. and WILLIAMS M. 1952: Resistivities of brine saturated sands in relation to pore geometry. Bulletin of the American Association of Petroleum Geologists, **36,** pp. 253

MÉLYTENGERI AGYAGOK PERMEABILITÁSÁNAK ÉS HŐVEZETŐKÉPESSÉGÉNEK BECSLÉSE ELEKTROMOS ÉS AKUSZTIKUS MÉRÉSEK ALAPJÁN

M. A. LOVELL

Módosított ödométer cella segítségével végezték el az Atlanti-óceán északkeleti részén a tengerfenékről vett, kilenc mintából álló sorozat laboratóriumi vizsgálatát. Ez a berendezés lehetővé teszi az elektromos formáció faktor, a hővezetőképesség, a nyomáshullám és a nyíróhullám sebesség egyidejű meghatározását, hagyományos egytengelyű konszolidáció-vizsgálat során. A permeabilitás és porozitás értékek az egytengelyű konszolidáció elmélete alapján vezethetők le. Az elektromos formáció tényező és a nyomáshullám sebessége szoros kapcsolatot mutat a permeabilitással, így a mért permeabilitást mind gyakorlatilag, mind elméletileg egy nagyságrenden belül meg lehet becsülni. A becslés pontosabbá tehető, ha a minta szerkezetére vonatkozó további ismereteket is felhasználunk (például kezdeti pórustérfogat, vagy nyíróhullám sebesség). Vízzel telített minták esetén mind a hővezetőképesség, mind az elektromos formáció tényező függ a porozitástól, és az elektromos formáció tényezőt a hővezetőképességgel is kapcsolatba lehet hozni. A nyomáshullám sebesség anizotróp, és ez feltételezhető más energia átadási folyamatokról is. Az irányfüggés, bár nem kritikus a tengerfenéken végzett termikus megfigyeléseknél, a mélyben fontossá válhat, különösen az üledékoszlopon át történő folyadék áramlás becslésénél.

ОЦЕНКА ПРОНИЦАЕМОСТИ И ТЕПЛОПРОВОДИМОСТИ МОРСКИХ ГЛУБОКОВОДНЫХ ГЛИН ПО ЭЛЕКТРИЧЕСКИМ И АКУСТИЧЕСКИМ ПАРАМЕТРАМ

М. А. ЛОВЕЛЛ

С помощью переоборудованной камеры компрессиометра (эдометра) проведены лабораторные исследования по серии из девяти образцов, отобранных со дна северо-восточной части Атлантического океана. Это устройство даёт возможность одновременно определить фактор электрической формации, теплопроводимость, скорость продольных и поперечных волн в ходе традиционных исследовании одноосной консолидации. Величны проницаемости и пористости можно вывести по теории одноосной консолидации. Фактор электрической формации и скорость продольных волн показывают тесную связь с проницаемостью так, что величину измеренной проницаемости можно предсказать и практически, и теорически, с точностью до одного порядка. Эмпирическое предсказание можно улучшить, если принять во внимание и допольнительные данные по структуре образцов (например, начальный объём пор образца или скорость поперечных волн). В насыщенных водой образцах как теплопроводимость, так и фактор электрической формации зависят от пористости. Используя пористость, можно связать электрическую формацию с теплопроводимостью в насыщенный водой образцах. Скорость продольных волн анизотропна, то же можно предполагать и в отношении других процессов с передачей энергии. Зависимость от направления, хотя она и не критична при тепловых исследованиях на дне моря на больших глубинах может стать важной, особенно при предсказании просасывания жидкостей через осадочные толщи.

GEOPHYSICAL TRANSACTIONS 1988
Vol. 33. No. 3–4. pp. 267–293

COMPUTER SIMULATION OF ^{252}Cf NEUTRON FIELDS IN BAUXITE WELL LOGGING

Iván BALOGH*

The distribution of neutron fields is examined by the computer modelling of neutron transport in bauxitic rocks of high hydrogen content. The modelling program, based on the Monte Carlo method is introduced and tested by known measurement data. Results of computations for typical bauxitic rocks are presented according to which epithermal and thermal neutrons have exponential distributions. With a knowledge of the epithermal and thermal neutron distributions the $\xi\Sigma_i$, Σ_s and Σ_a neutron physical parameters may be calculated. These parameters are in direct linear relation with the chemical composition of a given medium. The distorting effects on the neutron field of the probe and the borehole (wet or dry) is demonstrated qualitatively.

Keywords: bauxite prospecting, well logging, neutron logging, simulation, computer programs, macroscopic cross section

1. Introduction

Bauxites in Hungary are deposited on a karstic basement. During drilling, the drilling mud is often completely lost whereupon the hole is saved from collapse by casing. Thus, drilling for bauxite means more difficult conditions for well logging than for other materials because three-quarters of the measurements fall on cased or dry intervals. Due to these circumstances well logging in bauxite prospecting in Hungary has been based on nuclear logging since the beginning. Recently, nuclear well-logging methods have started to develop rapidly. In our case even the in situ determination of the chemical composition of bauxites in the borehole may be set as a long-term objective. The solution of the so-called direct problem must be the first step towards our objective, in other words the study of the behaviour of nuclear radiation fields in bauxite. Here, we deal with neutron fields induced in bauxitic rocks.

2. Possibilities of analytical and numerical computation of neutron fields in bauxite well logging

The so-called transport-equation, an integro-differential equation of seven variables, describes the distribution of neutrons according to space, energy and angle [SZATMÁRY 1971]. This equation may analytically be solved only in special cases: the most important of these are the solution according to Fermi's age

* Hungalu Prospecting Company, POB 31, Balatonalmádi, H–8221, Hungary
Manuscript received: 13 July, 1987

theory and the diffusion one. Low hydrogen content is among the initial conditions of both solutions; however, Hungarian bauxites have a high hydrogen content. The main minerals that constitute bauxites contain much hydrogen themselves (see *Table I* after BÁRDOSSY 1977, BETECHTIN 1964). Furthermore, these bauxites are strongly hygroscopic, their percentage of water is between 16 and 20% of the weight in the in-mine state [BARNABÁS 1966]. Thus, the hydrogen porosity of a high quality gibbsitic bauxite may reach 80% and that of the good boehmitic bauxites is around 60% *(Table II)*. This means that neither the diffusion approach nor Fermi's age theory can give a satisfactory solution. More accurate results may be obtained by the so-called multigroup diffusion method [SZATMÁRY 1971]. If one divides the energy scale into intervals the diffusion approach may be assumed valid even for a medium rich in hydrogen if the intervals are short enough. In this case a system of diffusion differential equations is to be solved where the number of equations corresponds to the number of intervals, i.e. to the number of groups. The source side of the equations of the lower groups will depend on all the groups having higher energy due to the presence of hydrogen [FEHÉR 1984]. The system of equations has an analytical solution in one dimension but with more complicated geometry only numerical methods work. At this stage, however, the necessary amount of computing time and memory capacity is comparable to those needed for the exact computer modelling of neutron transport. In view of this and because the modelling programs are simple and highly flexible, and because the borehole and the construction of the probe can easily be taken into account a Monte Carlo simulation program utilizing a Commodore 64 was written for the task.

Mineral	Chemical formula	Density (g/cm^3)	Hydrogen porosity (%)
Boehmite	AlOOH	3.035	45.6
Gibbsite	$Al(OH)_3$	2.35	81.4
Kaolinite	$Al_4(OH)_8Si_4O_{10}$	2.59	36.2
Calcite	$CaCO_3$	2.71	–
Siderite	$FeCO_3$	3.8	–
Pyrite	FeS_2	5.05	–
Goethite	FeOOH	4.2	42.6
Haematite	Fe_2O_3	5.1	–
Rutile	TiO_2	4.25	–
Anatase	TiO_2	3.9	–
Water	H_2O	1	100

Table I. The rock-forming minerals of Hungarian bauxites, their density and hydrogen prorosity

I. táblázat. A hazai bauxitok fő kőzetalkotó ásványai, sűrűségük és hidrogén porozitásuk

Таблица I. Главные породообразующие минералы, плотность и водородная пористость отечественных бокситов.

Mineral \ Rock code		0	1	2	3	4	5	6	7
Boehmite	[vol. %]	0	0	0	40	15	15	0	20
Gibbsite	[vol. %]	0	50	20	0	0	15	0	0
Kaolinite	[vol. %]	0	2	30	5	35	15	40	2.5
Calcite	[vol. %]	0	0.5	1	1	1	0.5	0	50
Pyrite	[vol. %]	0	0	0	0	0	13	0	0
Goethite	[vol. %]	0	2	3	4	3	5	15	2
Haematite	[vol. %]	0	4	7	8	7	0	5	4
Rutile/Anatase	[vol. %]	0	0.5	1	1	1	1	0	0.5
Water	[vol. %]	100	41	38	41	38	35.5	40	21
Density	[g/cm^3]	1	1.96	2.18	2.4	2.29	2.47	2.32	2.55
Hydrogen porosity	[%]	100	83.3	66.42	62.8	58.8	62.1	60.9	31.9

Table II. Mineral composition of rocks involved in the simulation of neutron fields
Code numbers: 0 — water; 1 — gibbsitic bauxite; 2 — clayey, gibbsitic bauxite; 3 — boehmitic bauxite; 4 — clayey, boehmitic bauxite; 5 — pyritic bauxite; 6 — clay; 7 — bauxite mixed with detrital limestone

II. táblázat. A neutronterek szimulációja során modellezett kőzetek ásványi összetétele
Kódszámok: 0 — víz; 1 — gibbszites bauxit; 2 — agyagos gibbszites bauxit; 3 — böhmites bauxit; 4 — agyagos böhmites bauxit; 5 — pirites bauxit; 6 — agyag; 7 — mészkőtörmelékes bauxit

Таблица II. Минеральный состав пород, моделированных при симуляции нейтронных полей.
Кодовые номера: 0 — вода, 1 — гиббситовый боксит, 2 — глинистый гиббситовый боксит, 3 — бёмитовый боксит, 4 — глинистый бёмитовый боксит, 5 — пиритизированный боксит, 6 — глина, 7 — боксит с обломками известняков.

3. Main features of the simulation program

The essence of the modelling of neutron fields is the computer simulation of the transport of single neutrons based on the simple laws of neutron physics and on probability considerations, and the statistical testing of the behaviour of an adequate number of simulated neutrons. Many publications are available on Monte Carlo methods and their applications in nuclear well logging [YERMAKOV 1975, SZOBOL 1981, DENISHIK et al. 1962, PSHENICHNYY 1982, FEHÉR 1984, KHISAMUTDINOV et al. 1985] so only the main features of the program are enumerated here.

The initial energy of the neutrons is determined by the energy spectrum of the modelled source. The energy spectrum of two sources having the same neutron yield is shown in *Fig. 1.* One is a Ra–Be source of 1 GBq activity (dotted line), the other is a ^{252}Cf source of 3 MBq activity (continuous line). The ^{252}Cf source has a smoother spectrum than that of the Ra–Be source. Bearing in mind the relatively low energies and the medium atomic weights only scattering was

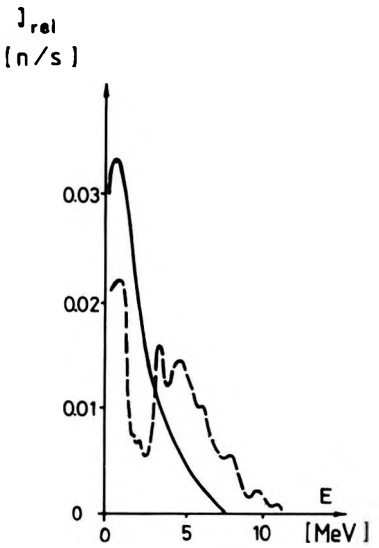

Fig. 1. Energy spectra of ^{252}Cf (continuous line) and Ra–Be (dotted line) neutron sources [after Radiation Sources 1974, SZABÓ—SIMONITS 1973, and KARDON et al. 1971]

1. ábra. Neutronforrások energia spektrumai: ^{252}Cf — folytonos vonal, Ra–Be — szaggatott vonal

Рис. 1. Энергетический спектр источников нейтронов ^{252}Cf—прерывситая линия; Ra–Be—сплошная линия.

taken into account from the possible interactions in the fast range. Angular distribution of scattering was assumed to be isotropic in the mass-centrical coordinate system. Values of the microscopic fast cross-sections were taken from the literature [NIKOLAYEV and BAZAZYANTS 1972, ALLEN 1960]. In the actual calculations the average values of the fast cross-sections weighted by 1/E (E: energy) were used except for hydrogen. The boundary of the fast range was defined as being at the beginning of the thermal Maxwell spectrum, i.e. at 0.1 eV *(Fig. 2)*.

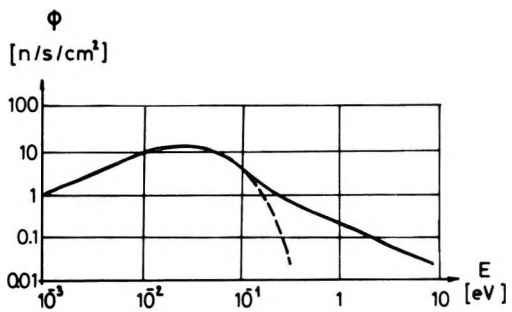

Fig. 2. Function of the fast and the thermal range of neutron flux. The part of the Maxwell spectrum which joins the fast range is indicated by dotted line [from SZATMÁRY 1971]

2. ábra. Neutronfluxus gyors és termikus tartományának csatlakozása. A termikus Maxwell-spektrum gyors tartományhoz csatlakozó szakaszát szaggatott vonal jelzi

Рис. 2. Стыковка быстрого и термического диапазонов нейтронного потока. Интервал стыковки термического спектра Максвелла к быстрому диапазону обозначен прерывистой линией.

In the modelling project resonance neutrons captured by indium and cadmium foils, and epithermal neutrons measured by a shielded He^3 proportional counter had to be modelled as well. Resonance neutrons were recorded by the program when crossing the 1.44 and 0.1 eV energy levels, thus, in fact the slowing down densities belonging to the corresponding energies were obtained. The flux of epithermal neutrons that could be measured by the proportional counter were recorded in the 1.0–0.1 eV energy interval during simulation.

In the thermal range scattering and absorbing interactions were taken into account. Scattering was regarded as being isotropic in the so-called laboratory system of coordinates, too, because the velocities of thermal neutrons and colliding nuclei are commensurable. The corresponding values of the microscopic cross-sections were taken from the literature [NAGY 1971]. There are considerable differences in the literature data regarding the thermal cross-section for scattering of hydrogen (38 barn in NAGY 1971, 20.3 barn in PSHENICHNYY 1982). On the other hand, the literature values of the thermal diffusion-length are very similar, viz. $L_d \approx 2.7$ cm. Calculating with that value and checking it by modelling the result gave 28 barn for the effective thermal cross-section for the scattering of hydrogen.

To trace the trajectories of neutrons the method given by DENISHIK et al. [1962] was used. The change in direction caused by scattering may be described by two rotation which have axes perpendicular to each other. Let us denote the product matrix of the multiplication of the two rotations by T_i at the i-th collision. Then vector $\vec{r}_i$ determining the direction of the next free path of the neutron may be obtained from the initial direction-vector $\vec{r}_0$ as follows:

$$\vec{r}_i = T_0 T_1 \ldots T_{i-1} T_i \vec{r}_0$$

that is

$$\vec{r}_i = P_{i-1} T_i \vec{r}_0$$

where

$$P_{i-1} = \prod_{k=0}^{i-1} T_k$$

Once the direction changes and the covered free paths are known, the position of the neutrons can be determined. Inhomogeneous material of complicated geometry may cause difficulties while modelling the free path because the total macroscopic cross-section (Σ_t), which determines the free path, becomes a function of place. In this case it is expedient to define a fictive cross-section of maximum value Σ_t^0 for the whole space under investigation [SZGŁOŁ 1981]. Thus, the free path is computed by the same algorithm in the whole space. In the j-th part of the space, however, the collision will be fictive with a probability of

$$K^j = \frac{\Sigma_t^0 - \Sigma_t^j}{\Sigma_t^0}$$

i.e. the energy and direction of movement of the neutron remain unchanged. The position and behaviour of the neutrons are easily traceable by this method in any medium having complicated geometry and chemical composition.

The Monte Carlo program was written in the above described way, see *Figs. 3* and *4*. Firstly the boundary and initial conditions — i.e. the geometrical structure, the chemical composition of the medium and the energy spectrum of the radiation source — are defined. The neutron is "born" in a radioactive source placed at the origin and it has an initial energy which is generated according to the spectrum of the source. The initial value of its direction-vector and P_{i-1} transformation matrix is unity. The initial direction of its trace gets a random value because the value of the first T transformation matrix is generated randomly. The fictive free path is independent of energy and space domain. The real free path is depending on energy and space domain and on whether the collision was real or fictive. In the case of a real collision the energy and direction of the neutron will change depending on the target nucleus. If the energy of the neutron decreases below 0.1 eV it will move over to the thermal range. In the thermal range the fictive free path is also independent of the space domain and the real free path will again be determined by the fictive and real collisions. The energy of the neutron is not changed by scattering and the distribution of scattering direction is independent of the target nucleus and isotropic. Absorption ends the "life" of neutrons. If insufficient neutrons are modelled the program steps to point A to generate a new neutron.

4. Testing of the simulation program by published data

Many publications discuss the space distribution of neutrons and experimental data are also found in a number of them. Most experiments deal with water but data concerning, for example, sandstone, are also available. Thus we could test our program by published data.

At first the field of a Na–γ–Be source placed in water — a homogeneous, isotropic medium — was simulated. The measured data corresponding to that model were published by DENISHIK et al. [1962]. The measurements were performed with the help of indium foil, thus, epithermal neutrons of 1.44 eV energy were involved. The initial energy was taken to be 0.966 MeV and the first, fast part of the program was run with 1.44 eV threshold-energy. The results of the computation involving 3900 neutrons can be seen in *Fig. 5*. The distance from the source is on the horizontal axis, the number of neutrons on concentrical, spherical surfaces at a distance r from the source is shown on the vertical axis. The scale is logarithmic. Measured data are marked by continuous line and dots represent the computed averages for 2 cm thick spherical shells.

Fig. 3. Block diagram of the Monte Carlo simulation program in the fast range

3. ábra. A szimulációs (Monte Carlo) program blokkvázlata a gyors tartományban

Рис. 3. Блок-схема симуляционной программы Монте Карло в быстром диапазоне.

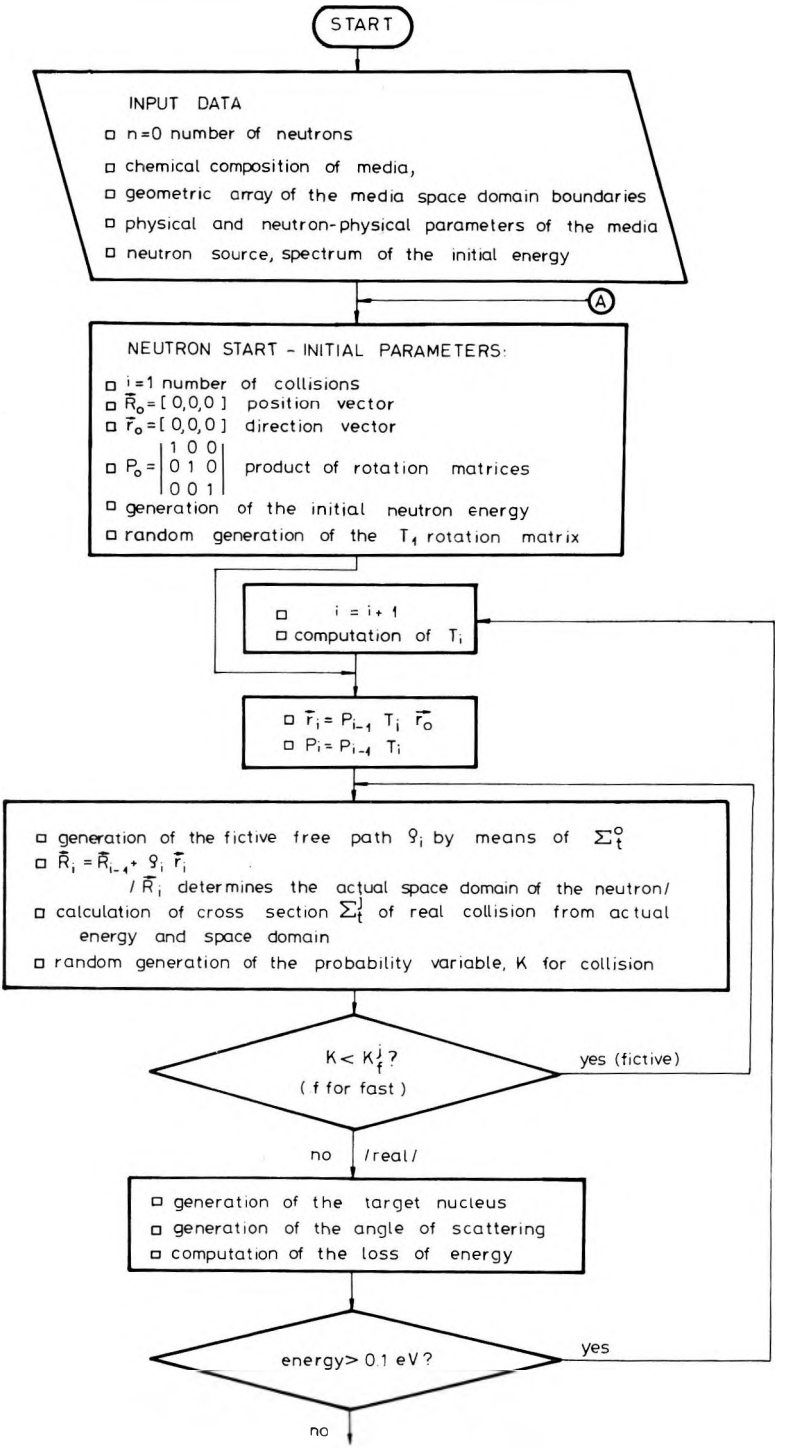
START
INPUT DATA
□ n=0 number of neutrons
□ chemical composition of media,
□ geometric array of the media space domain boundaries
□ physical and neutron-physical parameters of the media
□ neutron source, spectrum of the initial energy
A
NEUTRON START - INITIAL PARAMETERS:
□ i=1 number of collisions
□ $\vec{R}_o$=[0,0,0] position vector
□ $\vec{r}_o$=[0,0,0] direction vector
□ P_o = | 1 0 0 | / | 0 1 0 | / | 0 0 1 | product of rotation matrices
□ generation of the initial neutron energy
□ random generation of the T_1 rotation matrix
□ i = i+1
□ computation of T_i
□ $\vec{r}_i = P_{i-1}\ T_i\ \vec{r}_o$
□ $P_i = P_{i-1}\ T_i$
□ generation of the fictive free path ϑ_i by means of Σ_t^o
□ $\vec{R}_i = \vec{R}_{i-1} + \vartheta_i\ \vec{r}_i$
/ $\vec{R}_i$ determines the actual space domain of the neutron/
□ calculation of cross section Σ_t^j of real collision from actual energy and space domain
□ random generation of the probability variable, K for collision
$K < K_f^j$?
(f for fast)
yes (fictive)
no /real/
□ generation of the target nucleus
□ generation of the angle of scattering
□ computation of the loss of energy
energy > 0.1 eV ?
yes
no

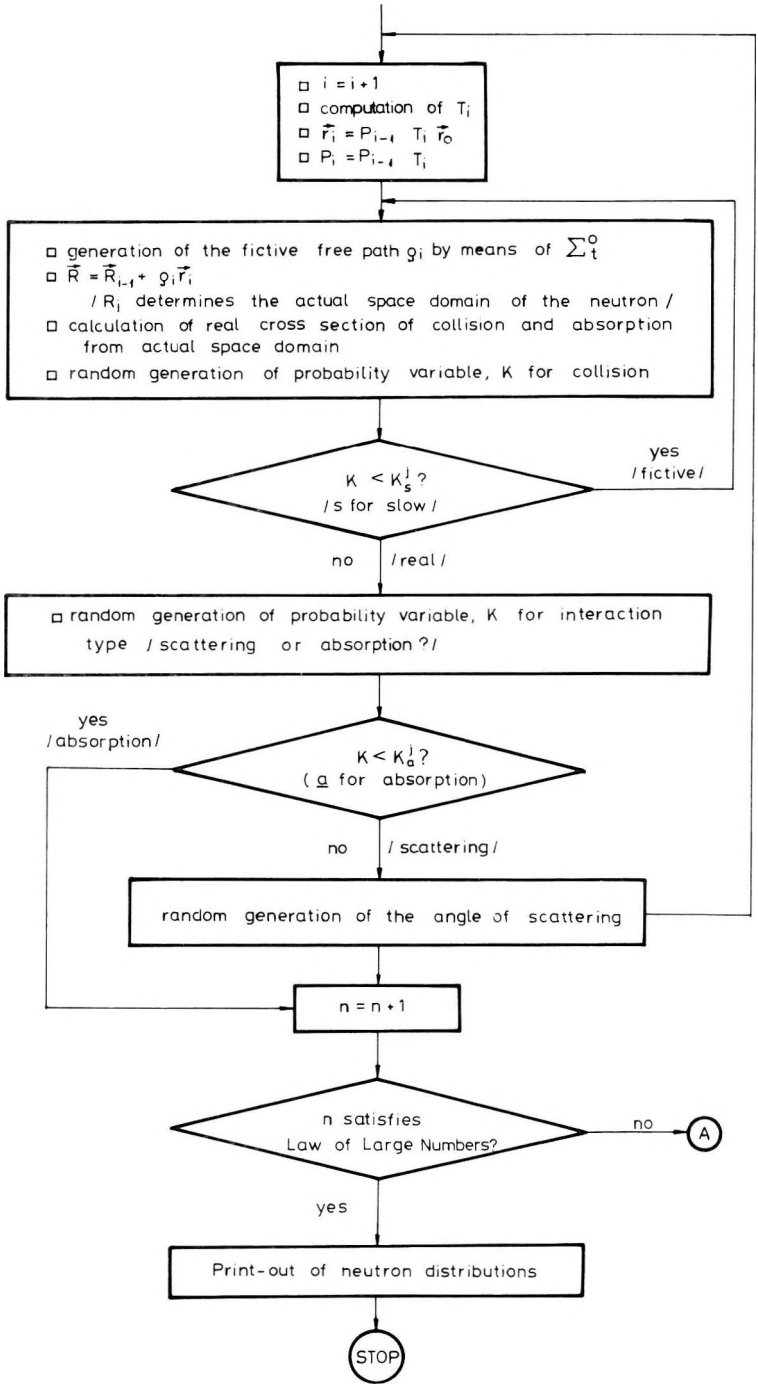

Fig. 4. Continuation of Fig. 3: Block diagram of the Monte Carlo simulation program in the thermal range

4. ábra. A 3. ábra folytatása: a szimulációs program a termikus tartományban

Рис. 4. Продолжение рис. 3. — симуляционная программа в термическом диапазоне.

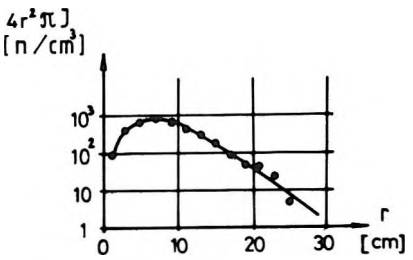

Fig. 5. Epithermal neutron distribution of Na–γ–Be neutron source measured in water by indium foil (continuous line) and computed by the simulation program (dots)

5. ábra. Na–γ–Be neutronforrás körüli epitermikus neutroneloszlás vízben, indium fóliával mérve (folytonos vonal), és a szimulációs programmal számítva (pontok)

Рис. 5. Распределение эпитермических нейтронов от источника Na–γ–Be в воде при измерении индиевой фольгой (сплошная линия) и при расчете симуляционной программой (пунктир).

At second a Ra–Be source — also placed in water — was simulated. The corresponding measured data were published by ALLEN [1960]. The space distribution of both the thermal and epithermal neutrons was studied. Epithermal neutrons were again measured by an indium foil. The relatively broad range, continuous initial energy-spectrum of the neutrons leaving the Ra–Be source had to be taken into account here (Fig. 1). Again, the program "recorded" the epithermal neutrons when they crossed the 1.44 eV energy level, while the threshold-energy of the thermal range was 0.1 eV. The results obtained from studying 9700 neutron-trajectories are presented in *Figs. 6* and *7*. Similarly to Fig. 5 the vertical axes represent the average number of neutrons on the 1 cm thick spherical shells at a distance r from the source but the scale is linear, as in the original publication. (The computed data were normalized in order to be matched to the curves: one unit was 350 neutrons for the epithermal neutrons and 37 500 neutrons for the thermal ones). Measured and computed data are represented by continuous lines and dots, respectively. Finally, similar computations were carried out for dry sandstone and for wet sandstone of 20% porosity. The corresponding data are to be found in [DENISHIK et al. 1962]. The source was also Ra–Be, the energy of the epithermal neutrons was 0.1 eV suited to the cadmium foil. 2400 neutrons were modelled in order to study their distribution in dry sandstone; *Fig. 8* shows the result. Measured and computed data — as averages for 15 cm thick spherical shells — are represented by a continuous line and dots, respectively. In the case of the 20% porosity wet sandstone the trajectories of approximately 1100 neutrons were simulated *(Fig. 9)*. Data concerning the thermal and epithermal distribution were also available so computations were performed for the thermal range, too. Computed data are averaged for 4 cm thick shells.

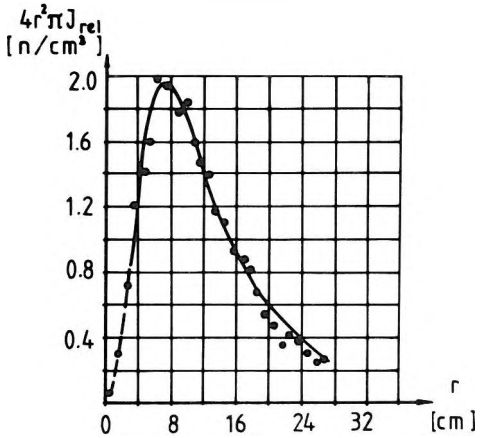

Fig. 6. Epithermal neutron distribution of Ra–Be neutron source measured in water by indium foil (continuous line) and computed by the simulation program (dots)

6. ábra. Ra–Be neutronforrás körüli epitermikus neutroneloszlás vízben, indium fóliával mérve (folytonos vonal), és a szimulációs programmal számítva (pontok)

Рис. 6. Распределение эпитермических нейтронов от источника Ra–Be в воде при измерении индиевой фольгой (сплошная линия) и при расчете симуляционной программой (пунктир).

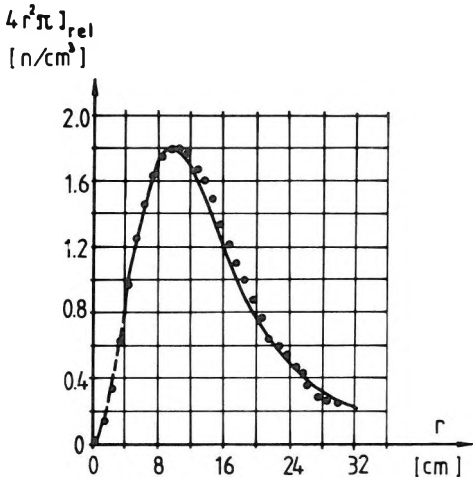

Fig. 7. Thermal neutron distribution of Ra–Be neutron source measured in water (continuous line) and computed by the simulation program (dots)

7. ábra. Ra–Be neutronforrás körüli termikus neutroneloszlás vízben mérve (folytonos vonal), és a szimulációs programmal számítva (pontok)

Рис. 7. Распределение термических нейтронов от источника Ra–Be, измеренное в воде (сплошная линия) и рассчитанное по симуляционной программе (пунктир).

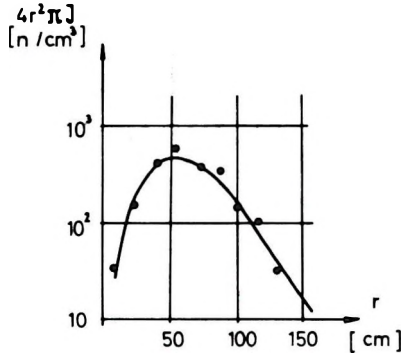

Fig. 8. Epithermal neutron distribution (energy 0.1 eV) around Ra–Be neutron source in dry sandstone (continuous line) and computed by the simulation program (dots)

8. ábra. Epitermikus, 0,1 eV energiájú neutronok eloszlása száraz homokkőben (folytonos vonal), és a szimulációs programmal számítva (pontok). Neutronforrás: Ra–Be

Рис. 8. Распределение эпитермических нейтронов с энергией 0,1 эв в сухом песчанике (сплошная линия) и рассчитанное по симуляционной программе (пунктир). Источник нейтронов — Ra–Be.

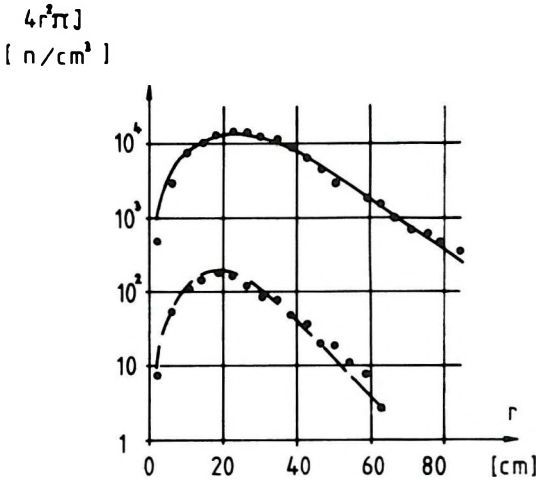

Fig. 9. Epithermal (energy ~0.1 eV, dotted line) and thermal (continuous line) neutron distributions around Ra–Be neutron source in 20% porosity wet sandstone, and computed by the simulation program (dots)

9. ábra. Epitermikus, 0,1 eV energiájú (szaggatott vonal), és termikus (folytonos vonal) neutronok eloszlása 20% porozitású vizes homokkőben, ill. a szimulációs programmal számítva (pontok). Neutronforrás: Ra–Be

Рис. 9. Распределение термических (сплошная линия) и эпитермических (штриховая линия) с энергией 0,1 эв, полученное в обводненных песчаниках с пористостью 20% и рассчитанное по симуляционной программе (пунктир). Источник нейтронов — Ra–Be.

5. Modelling the neutron field of ^{252}Cf in homogeneous isotropic bauxitic media

In bauxite well logging, instead of Ra–Be, ^{252}Cf neutron sources are used better suited to the requirements of neutron-activation measurements. The ^{252}Cf source produces neutrons by spontaneous fission, so the initial energy distribution of the emitted neutrons (N(E)) can be expressed analytically by the Maxwell distribution: $N(E) = \sqrt{E}\,e^{-E/T}$, where T is for ^{252}Cf: 1.43 MeV. [KARDON et al. 1971]. The ^{252}Cf spectrum of Fig. 1 was constructed with the help of this formula. The modelling program was run for pure water with the initial energy distribution of ^{252}Cf in order to compare the results with those of the Ra–Be source. The thermal neutron fields of the two sources in the form of the ratio of the number of neutrons in unit volume and the number of all neutrons modelled versus the distance from the source are presented in *Fig. 10*. This presentation relating to unit volumes meets better the conditions of well logging. As can be seen, both thermal neutron fields in pure water of both sources can be approximated linearly in logarithmic scale which means exponential distributions. It is also apparent that the softer spectrum of ^{252}Cf produces a steeper gradient (the average energy of Ra–Be is 3.6 MeV; that of ^{252}Cf is 2.05 MeV).

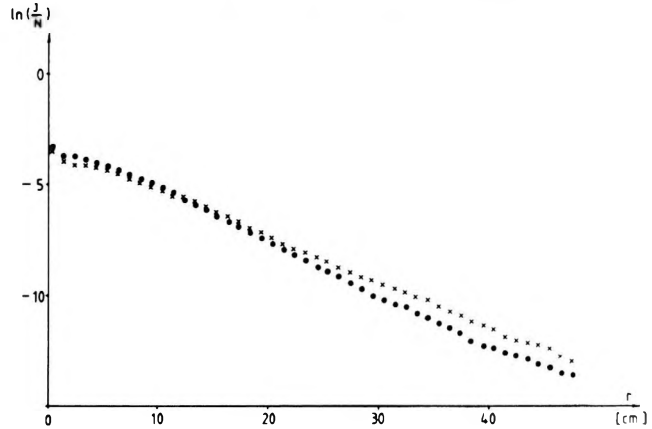

Fig. 10. Thermal neutron distributions around Ra–Be (calculated for 9,700 neutrons, x-es) and ^{252}Cf (calculated for 32,000 neutrons, dots) neutron sources in water, computed by the simulation program. On the vertical axis: logarithm of the ratio of neutrons in unit volume to all simulated neutrons

10. ábra. Termikus neutron eloszlások vízben, a szimulációs programmal számítva. x-ek: neutronforrás Ra–Be, 9700 neutronra számítva, pontok: neutronforrás ^{252}Cf, 32 000 neutronra számítva. A függőleges tengelyen az egységnyi térfogatra eső neutronok és az összes szimulált neutron hányadosának természetes logaritmusa

Рис. 10. Распределения термических нейтронов в воде, рассчитанные по симуляционной программе. Крестики — источник нейтронов Ra–Be, в расчете на 9700 нейтронов, пунктир — источник нейтронов ^{252}Cf в расчете на 32 000 нейтронов. По вертикальной оси отложены натуральные логарифмы отношений количеств нейтронов в единице объема к количеству всех симулированных нейтронов.

In other words it means that neutrons emitted from the ^{252}Cf source cover, on average, a somewhat shorter distance than the neutrons of the Ra–Be source.

In the following, calculations were performed on bauxites of differing composition, on clay, and on a mixture of bauxite and limestone detritus. The respective mineral and chemical compositions, densities and hydrogen-porosity data are to be found in *Tables II and III.* Mineral compositions were selected so that the main types of Hungarian bauxites should be represented [BÁRDOSSY 1977, BARNABÁS 1966]. The number of modelled neutrons was 10–11 thousand in each case. *Table IV.* and *Figures 11, 12* present the results for the epithermal between 0.1–1.0 eV and the thermal neutron flux respectively, normalized to unit source strength. Vertical axes are scaled for water, for the other media the coordinate system must be shifted.

Elements \ Rock code		0	1	2	3	4	5	6	7
Al	[g/cm³]	0	0.417	0.325	0.573	0.394	0.408	0.217	0.287
Si	[g/cm³]	0	0.011	0.169	0.028	0.197	0.085	0.225	0.014
Fe	[g/cm³]	0	0.195	0.329	0.391	0.329	0.438	0.574	0.195
Ti	[g/cm³]	0	0.012	0.024	0.024	0.024	0.024	0	0.012
Ca	[g/cm³]	0	0.005	0.011	0.011	0.011	0.005	0	0.543
S	[g/cm³]	0	0	0	0	0	0.351	0	0
C	[g/cm³]	0	0.002	0.003	0.003	0.003	0.002	0	0.163
O	[g/cm³]	0.888	1.222	1.242	1.296	1.268	1.09	1.237	1.296
H	[g/cm³]	0.112	0.093	0.074	0.07	0.066	0.07	0.068	0.036
Al_2O_3	[Dry weight %]	–	50.9	34.15	54.49	38.95	36.4	21.3	23.19
SiO_2	[Dry weight %]	–	1.56	20.12	3.03	22.06	8.54	25.1	1.29
Fe_2O_3	[Dry weight %]	–	18.05	26.15	28.13	24.59	29.55	42.74	11.97
TiO_2	[Dry weight %]	–	1.32	2.27	2.05	2.13	1.92	0	0.87
CaO	[Dry weight %]	–	0.49	0.84	0.76	0.79	0.36	0	32.51
Ignition loss	[Dry w. %]	–	27.69	16.46	11.54	11.48	23.22	10.85	30.17

Table III. Chemical composition of the modelled bauxitic rocks (elements and oxides referring to dry rock matrix, corresponding to laboratory chemical analysis)
For code numbers, see Table II.

III. táblázat. A modellezett bauxitos kőzetek kémiai összetétele, és száraz kőzetmátrixra vonatkoztatott oxidos összetétele (ez utóbbi megfelel a laboratóriumi vegyelemzésnek).
A kódszámokat lásd a II. táblázatban

Таблица III. Химический состав моделированных бокситов, исходный и пересчитанный на сухую породу в виде окислов; последний соответствует лабораторным определениям.
Кодовые номера см. в табл. II.

Analysis of the distributions of Figs. 11 and 12 enable one to conclude that in a homogeneous medium both the epithermal and thermal distributions may be well approached by exponential functions – or in logarithmic representation by straight lines. The linear relation seems to fit the best in the $r > 4$ cm range, which is the equivalent of the environment of the standard (76 mm) borehole diameter in bauxite prospecting in Hungary. The linear relation was also numerically examined in the 4–30 cm range. The Φ_{ep} epithermal flux is

$$\Phi_{ep} = F_1 \exp(-r/L_1)$$

that is

$$\ln \Phi_{ep} = \ln F_1 - (r/L_1)$$

For the Φ_t thermal flux

$$\Phi_t = F_2 \exp(-r/L_2)$$

that is

$$\ln \Phi_t = \ln F_2 - (r/L_2)$$

L_1 and L_2 can be related to the slowing down length (L_f) and the migration length (L_M), respectively [QUITTNER et al. 1971]. Constants given by regression calculation are in Table IV. Linear regression has proved to be adequately close in each case: the worst correlation factor was 0.99.

Rock code	Epithermal distribution		Thermal distribution	
	F_1 [10^{-4} n/s/cm^2]	L_1 [cm]	F_2 [10^{-2} n/s/cm^2]	L_2 [cm]
0	4.026	3.48	3.031	4.07
1	5.462	3.4	2.608	3.86
2	4.316	3.94	1.505	4.58
3	4.699	3.87	1.488	4.49
4	4.015	4.18	1.229	4.96
5	4.299	4.01	1.261	4.53
6	4.255	4.09	1.232	4.68
7	2.258	6.14	0.472	7.93

Table IV. Parameters of the exponential curves fitted to the epithermal and thermal neutron distributions of the ^{252}Cf neutron source between 4 and 30 cm (Figs. 11–12). For code numbers, see Table II.

IV. táblázat. A ^{252}Cf neutronforrás szimulált epitermikus és termikus neutroneloszlásaihoz (11–12. ábra) 4–30 cm között illesztett exponenciális görbék paraméterei. A kódszámokat lásd a II. táblázatban

Таблица IV. Параметры экспоненциальных кривых, полученных путем аппроксимации в интервале 4–30 см симулированных распределений эпитермических и термических нейтронов (рис. 11 и 12) источника ^{252}Cf. Кодовые номера см. в табл. II.

The L_f slowing down length increases with decreasing hydrogen content, if the rock composition is the same. This fact is taken advantage of by the dual-spaced neutron-porosity logging. *Figure 13* shows the relation between the L_1 data that were computed by regression from epithermal distributions and between the hydrogen content of a unit volume of the modelled media (H[g/cm^3]) and its hydrogen-porosity (P_H[%]). The relation has a hyperbolic tendency.

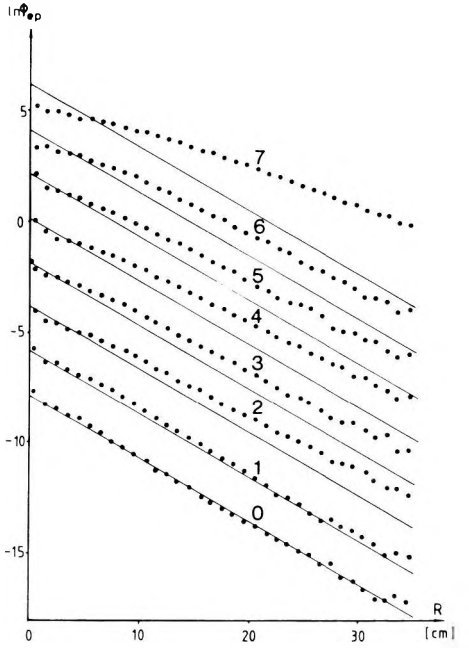

Fig. 11. Epithermal neutron flux around ^{252}Cf neutron source in water and in bauxitic rocks, computed by the simulation program. For code numbers, see Table II. The curves coded by 1–7 are in each case shifted by two units along vertical axis. The adjusted straight line of water (code number 0: see Table II) is also shifted for reference

11. ábra. Epitermikus neutronfluxus vízben és bauxitos kőzetekben, a szimulációs programmal számítva. Neutronforrás: ^{252}Cf, kódszámokat lásd a II. táblázatban. Az 1–7 kódszámú görbék a függőleges tengely mentén 2–2 egységgel el vannak tolva. Az eltolt görbék mellett referenciaként fel van tüntetve a 0 kódjelű víz kiegyenlítő egyenesének eltolt változata is

Рис. 11. Потоки эпитермических нейтронов в воде и в бокситах, рассчитанные по симуляционной программе. Источник нейтронов — ^{252}Cf, коды приводятся в табл. II. Кривые №№ 1–7 смещены вдоль вертикальной оси на 2 единицы каждая. Для сравнения рядом с ними нанесены смещенные прямые, соответствующие воде, обозначенной кодом 0.

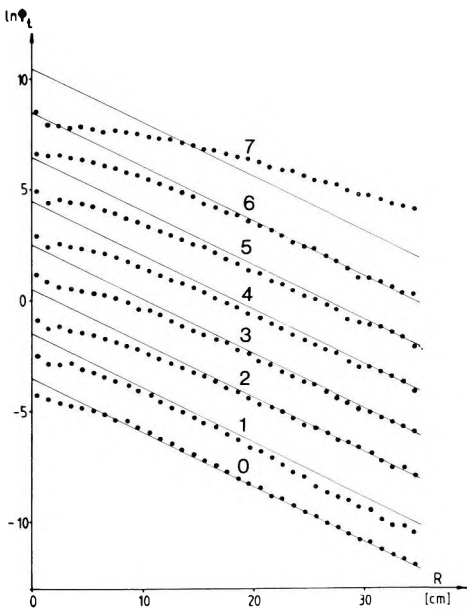

Fig. 12. Thermal neutron flux around ^{252}Cf neutron source in water and in bauxitic rocks, computed by the simulation program. Legend as in Fig. 11

12. ábra. Termikus neutronfluxus vízben és bauxitos kőzetekben, a szimulációs programmal számítva. Neutronforrás: ^{252}Cf, jelölések azonosak a 11. ábráéval

Рис. 12. Потоки термических нейтронов в воде и в бокситах, рассчитанные по симуляционной программе. Источник нейтронов — ^{252}Cf, обозначения см. на рис. 11.

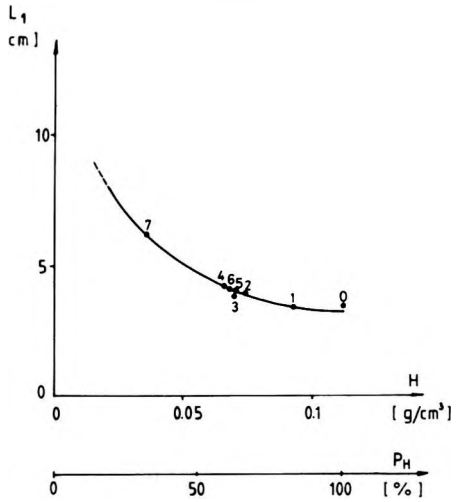

Fig. 13. Relation between the L_1 parameter of the exponential adjustment of the epithermal distributions (the reciprocals of gradients in Fig. 11) and hydrogen content (H) and hydrogen porosity (P_H) of the modelled medium. For code numbers, see Table II

13. ábra. Az epitermikus eloszlások exponenciális kiegyenlítő görbéinek L_1 paramétere (a 11. ábra görbemeredekségeinek reciproka) és a modellezett közeg hidrogéntartalma (H) ill. hidrogénporozitása (P_H) közötti kapcsolat. Kódszámokat lásd a II. táblázatban

Рис. 13. Взаимосвязь между параметром L_1 (величиной, обратной крутизнам кривых рис. 11) выравнивающих экспоненциальных кривых эпитермических распределений и содержанием водорода (H) в моделируемых породах и их водородной пористостью (P_H). Коды см. в табл. II.

6. Analysis of neutron fields simulated in homogeneous, isotropic bauxitic media

Let us examine the above discussed distributions more thoroughly. The following boundary condition is valid for epithermal flux due to the stationary neutron field (see Appendix):

$$\int_V q_{ep}\,\mathrm{d}V = \int_V \xi\Sigma_t\Phi_{ep}\,\mathrm{d}V = Q$$

that is

$$\int_V \xi\Sigma_t F_1 \exp(-r/L_1)\,\mathrm{d}V = Q$$

and so

$$8\pi\xi\Sigma_t F_1 L_1^3 = Q \qquad (1)$$

where Q = intensity of the neutron field [n/s] (it was unity for the simulated fields)

q_{ep} = epithermal slowing down density [n/s/cm^3]

ξ = average logarithmic energy-decrease

Σ_t = macroscopic total (epithermal) cross-section [cm^{-1}]

$\xi\Sigma_t$ = slowing down power [cm^{-1}]

$\mathrm{d}V$ = volume element [cm^3]

A similar boundary condition is valid in the thermal range:

$$\int_V \Sigma_a \Phi_t \, dV = Q$$

that is

$$\int_V \Sigma_a F_2 \exp(-r/L_2) \, dV = Q$$

and so

$$8\pi \Sigma_a F_2 L_2^3 = Q, \tag{2}$$

where Σ_a is the macroscopic absorption (thermal) cross-section [cm^{-1}].

The dimension of flux and thus of F is [$n/s/cm^{-2}$]. Let us now consider the L_1 and L_2 quantities. The following relation exists between the slowing down length, L_f, and the migration length, L_M, [QUITTNER et al. 1971]:

$$L_M^2 = L_f^2 + L_d^2,$$

where L_d is the thermal diffusion length [cm].

The following relation is also known [SZATMÁRY 1971]:

$$L_d^2 = 1/(3\Sigma_s \Sigma_a),$$

where Σ_s is the macroscopic scattering (thermal) cross-section [cm^{-1}].

Bearing in mind the above-mentioned relations:

$$L_M^2 - L_f^2 = 1/(3\Sigma_s \Sigma_a).$$

Since the slowing down and migration lengths, L_f and L_M, may correspond to L_1 and L_2, we obtain:

$$L_2^2 - L_1^2 = 1/(3\Sigma_s \Sigma_a). \tag{3}$$

Note that on the basis of the numbered equations—or in other words analysing the epithermal and thermal neutron distributions—the macroscopic cross-sections $\xi\Sigma_t$, Σ_s and Σ_a can be determined if Q, L_1, F_1, L_2 and F_2 are known. Thus, these might be considered as quasi-measurement data, obtained by measuring the neutron distribution. Data computed this way will be marked with an asterisk.

The above macroscopic cross-sections may also be directly calculated from the microscopic cross-sections [NAGY 1971, NIKOLAYEV and BAZAZYANTS 1972, and ALLEN 1960] if the chemical composition of the medium is known (Table III). Therefore the macroscopic cross-sections are linear combinations of the concentrations of elements. *Table V* contains the macroscopic cross-sections determined in two different ways — from quasi-measurement and from the chemical composition. The average of the total cross-section of hydrogen in the fast range was needed to calculate the slowing down power (see Appendix). This value was calculated by means of simulation for water. Consequently, the slowing down power of water computed from the chemical composition is based on quasi-measurement only, therefore this value was also marked with an

Rock code	Epithermal distribution		Thermal distribution			
	macroscopic cross-section		scattering		absorption	
	$\xi\Sigma_t$ [cm^{-1}]	$\xi\Sigma_t^*$ [cm^{-1}]	Σ_s [cm^{-1}]	Σ_s^* [cm^{-1}]	Σ_a [cm^{-1}]	Σ_a^* [cm^{-1}]
0	2.355*	2.355	2.012	3.81	0.0221	0.0194
1	1.971	1.855	1.79	3.749	0.0269	0.0265
2	1.577	1.510	1.497	2.209	0.0278	0.0275
3	1.493	1.461	1.447	2.168	0.0295	0.0295
4	1.398	1.356	1.361	1.77	0.0265	0.0266
5	1.475	1.433	1.411	2.235	0.0334	0.034
6	1.446	1.366	1.417	2.037	0.0309	0.0314
7	0.772	0.76	0.898	0.786	0.0184	0.0169

Table V. Neutron-physical parameters, calculated from the chemical composition of modelled bauxitic rocks (Table III) and from neutron distributions (marked with asterisk). For code numbers, see Table II.

V. táblázat. Neutronfizikai paraméterek a modellezett bauxitos kőzetek kémiai összetételéből (III. táblázat), illetve a szimulált neutroneloszlásokból (csillaggal jelölve) számítva. A kódszámokat lásd a II. táblázatban

Таблица V. Нейтронно-физические параметры, рассчитанные по химическому составу бокситов (табл. III) и по симулированным распределениям нейтронов, обозначенным звездочкой. Кодовые номера см. в табл. II.

asterisk in the Table. Naturally the slowing down powers computed from the chemical compositions of the other media are independent of the quasi-measured data concerning the given media.

The data of Table V are graphically illustrated by *Figs. 14, 15* and *16*. The code number of the given medium (see Table II) is indicated at each point. It can be seen that data calculated from the quasi-measurements and from the

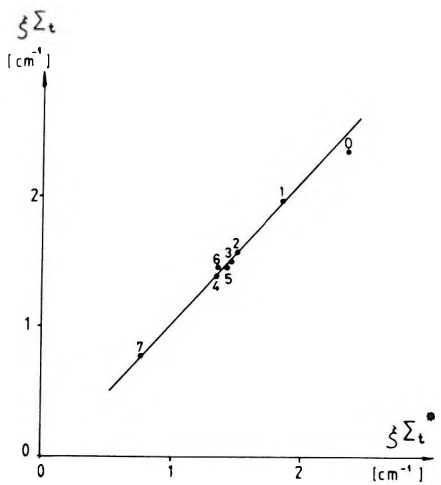

Fig. 14. Relation between *slowing down powers* $\xi\Sigma_t^*$ calculated from Formula (1) and $\xi\Sigma_t$ calculated from the chemical composition. For code numbers, see Table II

14. ábra. Az elemi összetételből számított $\xi\Sigma_t$, és a (1) összefüggés alapján számított $\xi\Sigma_t^*$ *fékezési erély* kapcsolata. A kódszámokat lásd a II. táblázatban

Рис. 14. Взаимосвязь между $\xi\Sigma_t$, рассчитанным по элементному составу, и *тормозящим моментом* $\xi\Sigma_t^*$, рассчитанным по выражению (1). Коды см. в табл. II.

chemical composition agree well; data of the macroscopic scattering even show a close correlation. Only the data of water denoted by code-number 0 and, in case of the scattering cross-section, the bauxite mixed with detrital limestone denoted by 7 fall slightly off the averaging straight line.

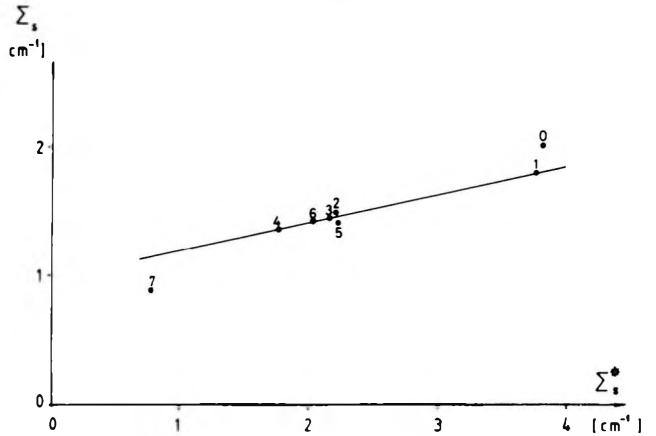

Fig. 15. Relation between *scattering cross section* Σ_s^* computed from Formula (2) and Σ_s calculated from the chemical composition. For code numbers, see Table II

15. ábra. Az elemi összetételből számított Σ_s, és a (2) összefüggés alapján számított Σ_s^* *szórási hatáskeresztmetszetek* kapcsolata. A kódszámokat lásd a II. táblázatban

Рис. 15. Взаимосвязь между Σ_s, рассчитанным по элементному составу, и *диффузионным эффективным сечением* Σ_s^*, рассчитанным по выражению (2). Коды см. в табл. II.

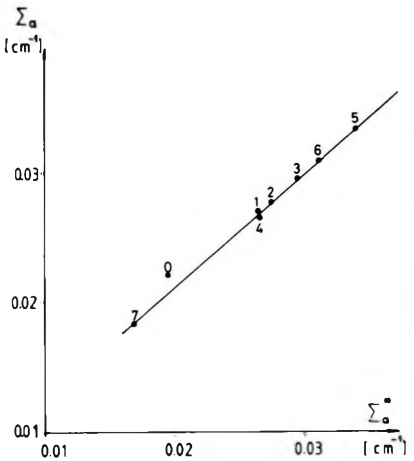

Fig. 16. Relation between *absorption cross-section* Σ_a^* calculated from Formula (3) and Σ_a calculated from the chemical composition. For code numbers, see Table II

16. ábra. A (3) összefüggés alapján számított Σ_a^* *abszorpciós hatáskeresztmetszetek* és az elemi összetételből számított Σ_a kapcsolata. A kódszámokat lásd a II. táblázatban

Рис. 16. Взаимосвязь между *абсорбционным эффективным сечением* Σ_a^*, рассчитанным по выражению (3), и Σ_a, рассчитанным по элементному составу. Коды см. в табл. II.

7. Simulation of neutron fields in bauxitic media taking into account the probe and the borehole

The main advantage of the Monte Carlo method in simulating neutron fields is that any arbitrary geometry may be assumed in the given medium — as was mentioned in the introduction. Using this possibility, let us see how the presence of the probe and the borehole influences the homogeneous, isotropic fields. An R–Z coordinate system was set up for the new calculations in which the probe and the borehole are positioned concentrically around the Z-axis; the diameter of the probe and the borehole are 40 and 80 mm, respectively. The studied volume of space extends 100 cm in the Z direction and 40 cm in the R direction. It was sufficient to record the neutron-physical events in $40 \times 100 = 4000$ elementary cells due to cylindrical symmetry. The ^{252}Cf radioactive source was at the origin of the coordinate system. The body of the probe was assumed to be iron but only half of its density was used in the calculations thus modelling the approximately 50% material/volume ratio of the probe structure. The probe extends 15 cm below the origin and extends along the whole studied volume of space upwards. In the first version of the calculations the hole is filled with water, in the second one it is dry. The medium is gibbsitic bauxite (code number 1 in Table II). This rock was selected for studying the influence of the probe and borehole because its neutron-physical parameters differ the most from the same of the probe and the dry hole and so the distorting effect is expected to be the strongest in this case. Naturally, the hole filled with water will not have a very strong distorting effect.

The arrangement and the results for water-filled boreholes are shown by *Figs. 17* and *18*. Cells having neutrons are inside the contour. Those cells in which the logarithm of the neutron density corresponding to unit neutron yield is greater than -12.5, are shaded horizontally, while vertical shading means those cells in which this logarithm is greater than -10. The distribution of epithermal neutrons of 0.1 eV energy is presented in Fig. 17, and the same for absorbed thermal neutrons in Fig. 18. The number of neutrons in the study was approximately 38 thousand. This number was not enough for an accurate, quantitative analysis of the neutron-distribution—as is suggested by the figures—though the maximum capacity of the Commodore 64 was used. Nevertheless, the figures are still suitable for qualitative analysis. The distortion caused by the sonde-body in the Z direction is apparent — especially in the case of the epithermal neutrons. It is also interesting that the epithermal neutrons hardly penetrate into the sonde-body. *Figure 19* showing the distribution of the thermal neutron flux along the Z axis, allows a comparison with the homogeneous isotropic field. The coordinate-system is identical with that of Fig. 12 and so the corresponding homogeneous isotropic data could be displayed along the data measured in an inhomogeneous field. The position of the ^{252}Cf source and the probe is also shown along the Z axis.

Figures 20–22 are similar to the previous ones with the difference that here the borehole was dry. The distorting effect in the Z direction increased.

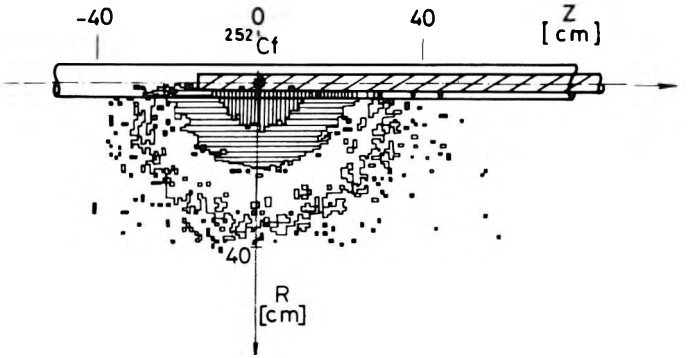

Fig. 17. Distribution of epithermal neutrons (energy ~0.1 eV) around a ^{252}Cf neutron source in *water-filled* borehole drilled in gibbsitic bauxite

17. ábra. Epitermikus, 0.1 eV energiájú neutronok eloszlása gibbszites bauxitot harántoló *vizes* fúrólyukban. Neutronforrás: ^{252}Cf

Рис. 17. Распределение эпитермических нейтронов с энергией 0,1 эв в *обводненной* скважине, вскрывшей гиббситовые бокситы. Источник нейтронов — ^{252}Cf.

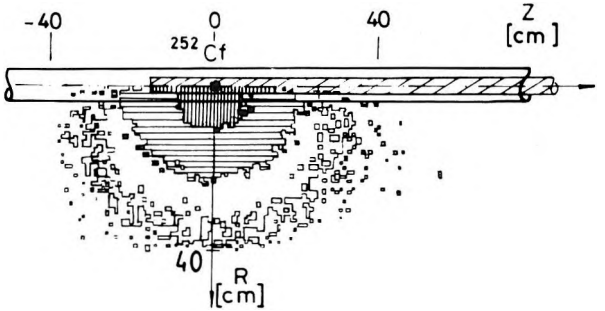

Fig. 18. Distribution of absorbed thermal neutrons around the ^{252}Cf neutron source in *water-filled* borehole drilled in gibbsitic bauxite

18. ábra. Abszorbeálódott termikus neutronok eloszlása gibbszites bauxitot harántoló *vizes* fúrólyukban. Neutronforrás: ^{252}Cf

Рис. 18. Распределение абсорбированных термических нейтронов в *обводненной* скважине, вскрывшей гиббситовые бокситы. Источник нейтронов — ^{252}Cf.

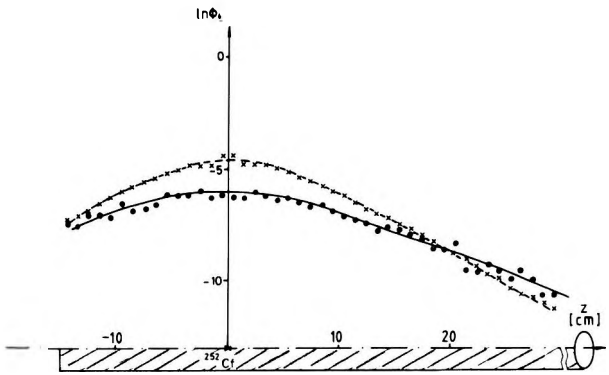

Fig. 19. Thermal neutron flux of a ^{252}Cf neutron source along the axis of the probe, in *water-filled* borehole drilled in gibbsitic bauxite (x-es mark the distribution computed for to the homogeneous isotropic medium)

19. ábra. Termikus neutronfluxus gibbszites bauxitot harántoló *vizes* fúrólyukban, a szonda tengelye mentén. Neutronforrás: ^{252}Cf (x-ek a homogén izotróp közegre számított eloszlást jelölik)

Рис. 19. Потоки термических нейтронов в *обводненной* скважине, вскрывшей гиббситовые бокситы, вдоль оси зонда. Источник нейтронов — ^{252}Cf (крестиками обозначено распределение, рассчитанное для однородной изотропной среды).

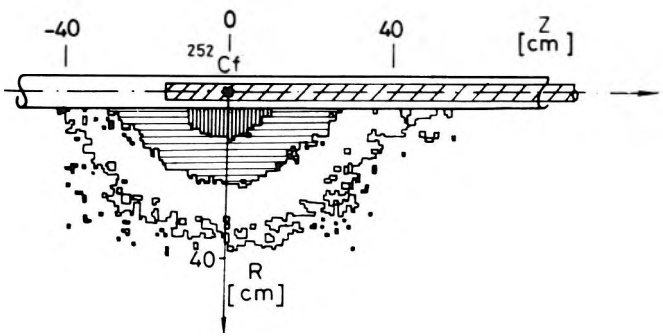

Fig. 20. Distribution of epithermal neutrons of 0.1 eV energy around the ^{252}Cf neutron source in *dry* borehole drilled in gibbsitic bauxite

20. ábra. Epitermikus, 0,1 eV energiájú neutronok eloszlása gibbszites bauxitot harántoló *száraz* fúrólyukban. Neutronforrás: ^{252}Cf

Рис. 20. Распределение эпитермических нейтронов с энергией 0,1 эв в *сухой* скважине, вскрывшей гиббситовые бокситы. Источник нейтронов — ^{252}Cf.

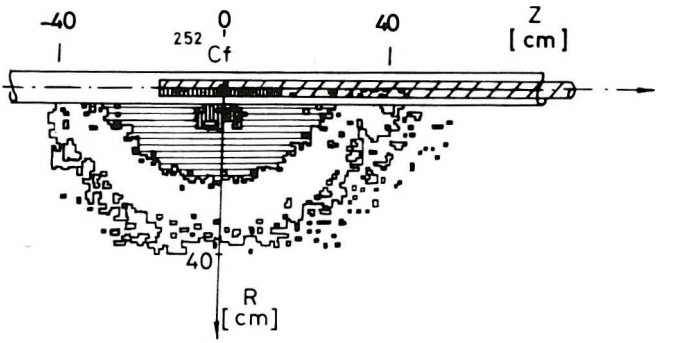

Fig. 21. Distribution of absorbed thermal neutrons around the ^{252}Cf neutron source in *dry* borehole drilled in gibbsitic bauxite

21. ábra. Abszorbeálódott termikus neutronok eloszlása gibbszites bauxitot harántoló *száraz* fúrólyukban. Neutronforrás: ^{252}Cf

Рис. 21. Распределение абсорбированных термических нейтронов в *сухой* скважине, вскрывшей гиббситовые бокситы. Источник нейтронов — ^{252}Cf.

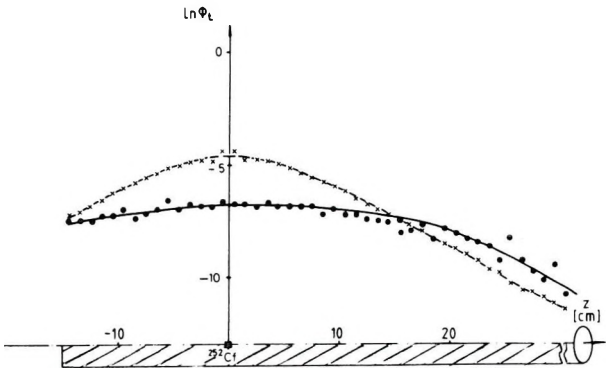

Fig. 22. Thermal neutron flux of a ^{252}Cf neutron source along the axis of the probe in *dry* borehole drilled in gibbsitic bauxite (x-es mark the distribution computed for to the homogeneous isotropic medium)

22. ábra. Termikus neutronfluxus gibbszites bauxitot harántoló *száraz* fúrólyukban, a szonda tengelye mentén. Neutronforrás: ^{252}Cf (x-ek a homogén izotróp közegre számított eloszlást jelölik)

Рис. 22. Потоки термических нейтронов в *сухой* скважине, вскрывшей гиббситовые бокситы, вдоль оси зонда. Источник нейтронов — ^{252}Cf (крестиками обозначено распределение, рассчитанное для однородной изотропной среды).

8. Conclusions

It has been proved that the Monte Carlo modelling program presented here is suitable for studying neutron fields developing in media of many chemical components or of complicated geometry. The program is also able to study the effect of layering. Nevertheless in order to solve such tasks of complicated geometry quantitatively, a faster computer with bigger memory—than the Commodore 64—is needed. Even so, it can be concluded from our computations that the epithermal and thermal neutron fields can be approximated by exponential functions in media of high hydrogen content. These media may be —besides bauxitic rocks—laterites, coals, clays or kaoline.

This exponential approach may be used to correct neutron-activation measurements—as was discussed earlier [Balogh and Horváth 1983]—and on the other hand it may help the interpretation of spectral neutron-gamma measurements [Chrusciel et al. 1985], i.e. it could render a possibility to take into account the influence of neutron distribution on the measurements. The exponential distribution also renders the in situ measurement of the $\xi\Sigma_t$, Σ_s and Σ_a neutron-physical parameters possible in rocks of high hydrogen content by profiling of the epithermal and thermal neutron fields by two times two (two epithermal and two thermal) detectors. It has been proven [Flaum 1983] that it is possible to construct a suitable tool; he reports on the realization of such a tool for hydrogen porosity determination in dry boreholes. To decrease the distorting effects and to be able to detect the epithermal neutrons the body of such a tool should be made of some plastic of high hydrogen content and it should be pressed against the wall of the hole. The parameters measured in this way will be linearly related to the chemical composition of rocks, which is the most important feature to be learnt when prospecting for solid minerals.

APPENDIX

It is known that the slowing down density in media which do not absorb neutrons is as follows [Szatmáry 1971]:

$$q(r, E) = \int_{E'=E}^{E/\alpha} \Sigma_t(E') \frac{E - E'\alpha}{E'(1-\alpha)} \Phi(r, E')\, \mathrm{d}E'$$

where $\alpha = (A-1)/(A+1)$

A = atomic weight

since Σ_t is the sum of the cross-sections of the i components, the integral can be divided

$$q(r, E) = \int_{E'=E}^{E_0} \Sigma_t^{\text{hydrogen}}(E') E \Phi(r, E') \frac{\mathrm{d}E'}{E'} + \sum_i \int_{E'=E}^{E/\alpha_i} \Sigma_t^i(E') \frac{E - E'\alpha_i}{E'(1-\alpha_i)} \Phi(r, E')\, \mathrm{d}E'$$

Here it was taken into account that $\alpha = 0$ for hydrogen. For the other rock-forming elements $\alpha_i \approx 1$, thus the integral can be simplified [SZATMÁRY 1971]:

$$q(r, E) = \int_{E'=E}^{E_0} \Sigma_t^{\text{hydrogen}}(E') E\Phi(r, E') \frac{dE'}{E'} + \sum_i \Sigma_t^i(E) \xi_i E\Phi(r, E)$$

It is usually accepted to decompose the flux to two factors, one depending on the position and the other on the energy [SZATMÁRY 1971]:

$$\Phi(r, E) = R(r)F(E).$$

If it is assumed that the function of energy $F(E)$ is nearly constant in bauxitic rocks, this expression can be written in the following form

$$q(r, E) = \bar{\Sigma}_t^{\text{hydrogen}} E\Phi(r, E) + \sum_i \Sigma_t^i(E) \xi_i E\Phi(r, E)$$

where

$$\bar{\Sigma}_t^{\text{hydrogen}} = \frac{R(r) \int_{E'=E}^{E_0} \Sigma_t^{\text{hydrogen}}(E') F(E') \, dE'/E'}{R(r)F(E)}$$

This quantity will be constant because $F(E)$ was assumed to be constant. If the overstroke is omitted and instead of $E\Phi(r, E)$ $\Phi_{ep}(u, r)$ is written, and if it is considered that $\xi(\text{hydrogen}) = 1$ then:

$$q_{ep} = \sum_i \Sigma_t^i \xi_i \Phi_{ep}(u, r) = \xi \Sigma_t \Phi_{ep}$$

where $u = \ln (E_0/E)$.

Note: if $F(E)$ changes then this equation will only approximately be valid because $\Sigma_t^{\text{hydrogen}}$ was assumed constant. The accuracy of the approximation depends on $F(E)$. However, our modelling results support the assumption of $F(E) \approx$ const. in the studied rocks.

REFERENCES

ALLEN W. D. 1960: Neutron detection. Newnes LTD., London, 260 p.

BALOGH I., HORVÁTH J. 1983: Quantitative determination of Al_2O_3 content in bauxite-prospecting boreholes by means of neutron-activation logging. Geophysical Transactions, **29**, 2, pp. 173–185

BARNABÁS K. 1966: Bauxite. In: The geology of our mineral deposits (in Hungarian). Ed.: B. Jantsky, Műszaki Kiadó, Budapest, pp. 143–178

BÁRDOSSY GY. 1977: Karst bauxites (in Hungarian). Akadémiai Kiadó, Budapest 413 p.

BETECHTIN A. G. 1964: Lehrbuch der Speziellen Mineralogie. VEB Deutscher Verlag für Grundstoffindustrie, Leipzig, 679 p.

CHRUSCIEL E., PALKA K., KACZMARSKI S., WOJDA F. 1985: Determination of coal properties in boreholes by neutron capture and backscattered gamma radiation spectrometry (in Russian). Proceedings of the 30th International Geophysical Symposium, Moscow, Vol B, 3, pp. 51–63

DENISHIK S. A., REZVANOV R. A., LUKHMINSZKIJ B. E. 1962: The method of statistic tests applied to the computation of the distribution of neutrons in problems of the neutron logging. In: Portable neutron generators in nuclear geophysics (in Russian). Editor: Savochin S. I., Publ. H. "Gosatomizdat", Moscow, pp. 172–202

FEHÉR S. 1984: Methods for computing neutron radiation fields. In: Electron shell and nuclear physics in the exploration of fluids and minerals in deep boreholes (in Hungarian). Ed.: Ferenczy L., Association of Hungarian Geophysicists, Csopak, pp. 109–160

FLAUM C. 1983: Dual detector neutron logging in air filled boreholes. SPWLA Twenty-fourth annual logging symposium transactions, Vol. II., BB, 21 p.

KARDON B., KOLTAY E., MAKRA Zs. 1971: Neutronsources (in Hungarian). In: Neutronphysics. Ed.: D. Kiss, P. Quittner. Akadémiai Kiadó, Budapest pp. 49–130

KHISAMUTDINOV A. I., STARIKOV V. N., MOROZOV A. A. 1985: The Monte Carlo algorithm in nuclear geophysics (in Russian). Publ. H. "Nauka", Novosibirsk, 157 p.

NAGY S. 1971: Neutron source- and absorption-application in chemical analysis (in Hungarian). In: Neutronphysics. Ed.: D. Kiss, P. Quittner. Akadémiai Kiadó, Budapest, pp. 941–952

NIKOLAYEV M. N., BAZAZYANTS N. O. 1972: The anisotropy of the elastic scattering of neutrons (in Russian). Publ. H. "Atomizdat", Moscow, 236 p.

PSHENICHNYY G. A. 1982: Interaction between radiation and substance and modelling problems of nuclear geophysics (in Russian). Publ. H. "Energizdat", Moscow, 221 p.

QUITTNER P., BATA L., DEME S., MAKRA Zs., NAGY T., SOMOGYI GY. 1971: Neutron-detection (in Hungarian). In: Neutronphysics. Ed.: D. Kiss, P. Quittner. Akadémiai Kiadó, Budapest, pp. 131–256

Radiation sources for laboratory and industrial use. 1974. (Catalogue 1974/75). Radiochemical Centre, Amersham, 99 p.

SZABÓ E., SIMONITS A. 1973: Activation analysis (in Hungarian). Műszaki Kiadó, Budapest, 362 p.

SZATMÁRY Z. 1971: Neutrongas-physics (in Hungarian). In: Neutronphysics. Ed.: D. Kiss, P. Quittner. Akadémiai Kiadó, Budapest, pp. 809–870

SZOBOL I. M. 1981: The basics of the Monte Carlo methods (in Hungarian). Műszaki Kiadó, Budapest, 318 p.

YERMAKOV S. M. 1975: The Monte Carlo method and adjacent problems (in Russian). Publ. H. "Nauka", Moscow, 472 p.

A ^{252}Cf NEUTRONFORRÁS TERÉNEK SZÁMÍTÓGÉPES SZIMULÁCIÓJA A BAUXITKAROTÁZSBAN

BALOGH Iván

A dolgozat a neutronterek eloszlását vizsgálja a neutrontranszport számítógépes szimulációjára alapozva, nagy hidrogéntartalmú – elsősorban bauxitos – kőzetekben. Röviden ismerteti a kidolgozott szimulációs (Monte Carlo) programot, majd le is teszteli publikációkból ismert mérési adatok segítségével. A dolgozat a továbbiakban tipikus bauxitos kőzetekre végzett számítások eredményeit ismerteti, amelyek szerint az adott kőzetekben az epitermikus és termikus neutronok exponenciális eloszlásúak. Megmutatja, hogy az epitermikus és termikus neutroneloszlások ismeretében kiszámíthatók a $\xi\Sigma_t$, Σ_s, Σ_a neutronfizikai paraméterek, melyek közvetlen lineáris kapcsolatban állnak az adott közeg elemi összetételével. Végül kvalitativ jellegű eredményeket mutat be a szondatest és a vizes, ill. száraz fúrólyuk neutronteret torzító hatásáról.

СИМУЛЯЦИЯ ПОЛЯ НЕЙТРОННОГО ИСТОЧНИКА ^{252}Cf В БОКСИТОВОМ КАРОТАЖЕ С ПОМОЩЬЮ ЭВМ

Иван БАЛОГ

В статье исследуется распределение нейтронных полей на основе симуляции на ЭВМ нейтронного транспорта в породах с большим содержанием водорода, в первую очередь в бокситовых породах. Кратко излагается выработанная программа симуляции Монте Карло, которая тестируется с помощью известных по литературе данных измерений, далее излагаются результаты расчётов по типичным бокситовым породам по которым резонансные и тепловые нейтроны имеют степенное распределение. Показывается, что зная распределение резонансных и тепловых нейтронов, можно рассчитать нейтронно-физические параметры $\xi\Sigma_i$, Σ_s, Σ_a, которые имеют непосредственную линейную связь с элементным составом данной среды. Наконец в статье представляются качественные результаты по искажающему влиянию на нейтронное поле обводенных и сухих скважин и корпуса зонда.